Microphysiological systems for modelling and monitoring biological barriers

Jose Yeste Lozano

Universitat Autònoma
de Barcelona

Tesis doctoral

Microphysiological systems for modelling and monitoring biological barriers

Jose Yeste Lozano

Directores:
Dra. Rosa Villa Sanz
Dr. Xavier Illa Vila

Tutor:
Dr. Jordi Aguiló Llobet

Universitat Autònoma de Barcelona
Departament de Microelectrònica i Sistemes Electrònics
Programa de Doctorat en Enginyeria Electrònica i de Telecomunicació

Bellaterra (Barcelona), mayo 2018

Dra. **Rosa Villa Sanz**, científica titular del Consejo Superior de Investigaciones Científicas, Dr. **Xavier Illa Vila**, investigador del Centro de Investigación Biomédica en Red de Bioingeniería Biomateriales y Nanomedicina, y Dr. **Jordi Aguiló Llobet**, catedrático del Departament de Microelectrònica i Sistemes Electrònics de la Universitat Autònoma de Barcelona,

certifican

que la memoria de tesis, **Microphysiological systems for modelling and monitoring biological barriers**, presentada por **Jose Yeste Lozano** para optar al título de **Doctor en Ingeniería Electrónica y de Telecomunicación** se ha realizado bajo su dirección en el Instituto de Microelectrónica de Barcelona perteneciente al Centro Nacional de Microelectrónica del Consejo Superior de Investigaciones Científicas y ha sido tutelada en el **Departament de Microelectrònica i Sistemes Electrònics** de la Universitat Autònoma de Barcelona.

Dra. Rosa Villa Sanz (codirectora)	Dr. Xavi Illa Vila (codirector)	Dr. Jordi Aguiló Llobet (tutor)

Bellaterra (Barcelona), Mayo 2018

A Sonia

Resumen

Los sistemas microfisiológicos (MPS) son modelos *in vitro* microfabricados que emulan las condiciones *in vivo* fisiológicamente relevantes, como la organización celular y las señales microambientales. Las microtecnologías han permitido el desarrollo de sofisticados MPS capaces de recapitular fielmente la fisiología a nivel de tejido y órgano. Los MPS son particularmente útiles para modelar barreras biológicas, es decir, epitelios y endotelios que separan la circulación sanguínea de los compartimentos tisulares. Su función de barrera es crucial para mantener la homeostasis en los órganos y su desregulación juega un papel importante en la fisiopatología de muchas enfermedades humanas prevalentes. La función principal de un tejido barrera es controlar el transporte transepitelial de solutos. Por lo tanto, la capacidad de cuantificar el transporte en un modelo de barrera es crítico. La espectroscopía de impedancia eléctrica (EIS) permite su cuantificación con las ventajas de ser no destructiva, sin utilizar marcadores y de fácil aplicación en tiempo real. EIS puede determinar 1) la resistencia eléctrica transepitelial (TEER), que evalúa la integridad de la barrera (estrechamente relacionada con la rigidez del espacio intercelular); 2) la capacitancia de la capa celular (C_{cl}), que puede proporcionar información sobre el área superficial de la membrana; y 3) la contribución de la solución del medio a la impedancia.

Mientras que el EIS es fácil de realizar mediante electrodos extracelulares, es difícil lograr la distribución de corriente uniforme requerida para mediciones precisas dentro de los canales de cultivo celular miniaturizados. Entonces, se puede suponer erróneamente que todo el área de cultivo de células contribuye igual a la medición, lo que puede conducir a errores de cálculo del TEER. Esto puede explicar parcialmente la gran disparidad de los valores de TEER reportados para tipos de células idénticas. Aquí, se presenta un estudio numérico para dilucidar este problema en algunos cultivos celulares previamente reportados y para proponer un factor de corrección geométrica (GCF) que corrige este error y que permite aplicarse retrospectivamente. Este estudio también se usó para optimizar una configuración tetrapolar especialmente adecuada para realizar mediciones EIS precisas en canales microfluídicos, y lo que es más importante, los electrodos cubren mínimamente la superficie lo que permite que las células se puedan visualizar junto con el análisis de TEER. Posteriormente, se desarrolló una cámara de perfusión modular con electrodos integrados en base a esta configuración óptima. El dispositivo comprende una membrana porosa desechable en la que se forma el tejido barrera y dos placas reutilizables donde se encuentran los electrodos. Por lo tanto, el tejido en la membrana se puede ensamblar en el sistema para medirlo y exponerlo al flujo, no solo para aplicar un estímulo mecánico fluidico sino también para suministrar continuamente nutrientes y eliminar los desechos. Además, la concentración de NaCl en ambos lados del tejido se puede estimar a partir de la conductancia eléctrica medida con los mismos electrodos integrados en una configuración bipolar. Un modelo *in vitro* del túbulo renal se utilizó para validar el sistema de medición. Como resultado, la concentración de NaCl se estimó a partir de la conductancia que permite la medición en línea del gradiente químico transepitelial de NaCl, que es una función primaria del túbulo renal.

El desarrollo de MPS con múltiples barreras biológicas interconectadas expandirá la tecnología para recapitular funciones más complejas a nivel de órgano. Sin embargo, existen múltiples desafíos técnicos para reproducir varias barreras biológicas en un solo dispositivo mientras se mantiene un microambiente controlado particular para cada tipo de célula. Aquí se presenta un novedoso dispositivo microfluídico donde 1) múltiples tipos de células que están dispuestas en compartimentos uno al lado del otro están interconectadas con microsurcos y donde 2) múltiples tejidos barrera se miden a través de electrodos metálicos que están enterrados debajo de los microsurcos. Como prueba de concepto, el dispositivo se usó para imitar la estructura de la barrera hematorretiniana (BRB), incluidas las barreras interna y externa. Ambas barreras se formaron con éxito en el dispositivo y se monitorearon en tiempo real, lo que demuestra su gran potencial para su aplicación a la tecnología de órgano en un chip.

Abstract

Microphysiological systems (MPS) are biologically inspired microengineered *in vitro* models that emulate physiologically relevant *in vivo* conditions, such as cell organization and microenvironmental cues. Microtechnologies have enabled the development of significant MPS that are able to faithfully recapitulate tissue- and organ-level physiology. MPS are particularly useful for modelling biological barriers, that is, epithelia and endothelia that separate the blood circulation from tissue compartments. Their barrier function is crucial to maintain organ homeostasis and their deregulation play an important role in the pathophysiology of many prevalent human diseases. The primary function of a barrier tissue is to control the transepithelial transport of solutes. Therefore, the ability to quantify transport in a barrier model is critical. Electrical impedance spectroscopy (EIS) permits its quantification with the advantages of being non-destructive, label-free, and easily applicable in real time. EIS can determine 1) the transepithelial electrical resistance (TEER), which evaluates the barrier integrity (closely related with the tightness of the intercellular space); 2) the cell layer capacitance (C_{cl}), which can yield information about the membrane surface area; and 3) the contribution of the medium solution to the impedance.

While EIS is easy to carry out by means of extracellular electrodes, it is challenging to achieve the uniform current distribution required for accurate measurements within miniaturized cell culture channels. Then, it may be erroneously assumed that the entire cell culture area contributes equally to the measurement leading to TEER calculation errors. This can partially explain the large disparity of TEER values reported for identical cell types. Here, a numerical study is presented to elucidate this issue in some cell cultures previously reported and to propose a geometric correction factor (GCF) to correct this error and be applied retrospectively. This study was also used to optimize a tetrapolar configuration especially suitable for performing accurate EIS measurements in microfluidic channels; importantly, it implements minimal electrode coverage so that the cells can be visualised alongside TEER analysis. A modular perfusion chamber with integrated electrodes was developed based on this optimal configuration. The device comprises a disposable porous membrane where the barrier tissue is formed and two reusable plates where the electrodes are located. Therefore, the tissue on the membrane can be assembled into the system to be measured and exposed to flow—not only to apply a fluid mechanical stimuli but also to continuously supply nutrients and remove waste. Additionally, the concentration of NaCl in both sides of the tissue can be estimated from the electrical conductance measured with the same integrated electrodes in a bipolar configuration. An in vitro model of the renal tubule was used to validate the measurement system. As a result, the concentration of NaCl was estimated from the conductance enabling in-line measurement of the transepithelial chemical gradient of NaCl, which is a primary function of the renal tubule.

The development of MPS with multiple interconnected biological barriers will expand the technology to recapitulate more complex organ-level functions. Unfortunately, there are multiple technical challenges to reproduce several biological barriers in a single device while maintaining a particular controlled microenvironment for each cell type. Here, it is presented a novel microfluidic device where 1) multiple cell types that are arranged in side-by-side compartments are interconnected with microgrooves and where 2) multiple barrier tissues are measured through metal electrodes that are buried under the microgrooves. As a proof-of-concept, the device was used to mimic the structure of the blood-retinal barrier (BRB) including the inner and the outer barriers. Both barriers were successfully formed in the device and monitored in real time, demonstrating its great potential for application to organ-on-a-chip technology.

Table of Contents

1

Introduction

1.1 | MOTIVATION AND OBJECTIVES

Recent advances in microtechnologies and biomaterials have provided a new set of tools to construct physiologically relevant microdevices for cell culture, the so-called ‘microphysiological systems’ (MPS) or sometimes referred to as ‘organ-on-a-chip’ when using microelectronic fabrication technologies [1, 2]. These biologically inspired *in vitro* devices intend to faithfully recapitulate tissue- and organ-level physiology by emulating relevant conditions of the *in vivo* microenvironment, which is not possible with conventional cell cultures typically based on culture plates. Since the development of a microfluidic lung alveolus chip in 2010 by Ingber and co-workers [3], many researchers have used the same microfluidic culture concept to create organ-on-chips. The basic principle of these engineered devices is to simplify the organ physiology to its fundamental elements. In that particular case, this simplest element was the physical interface between the alveolar epithelium and the vascular endothelium, which was emulated through a porous membrane in the centre of two microfluidic channels.

My background knowledge about the passive electrical properties of tissues, together with the microelectronic technologies that are available at the Instituto de Microelectrónica de Barcelona of the Centro Nacional de Microelectónica (IMB-CNM, CSIC) prompted me to investigate the integration of impedance-based sensing capabilities in MPS. Therefore, biologists could be provided with information on the cultured tissues in real time. Electrical impedance spectroscopy (EIS) is a primary technique to monitor biological barriers that has been successfully applied in previous works from the Biomedical Applications Group (GAB) of the IMB-CNM. The GAB is a multidisciplinary group mainly focused on providing innovative technological solutions to relevant biomedical problems. In this group, EIS measurements have been widely used to assess *in vivo* and *ex vivo* tissues, for example to quantify hepatic steatosis [4], corneal permeability [5], or ischemic injury [6].

The presented thesis is aimed at developing MPS for modelling and, more relevantly, monitoring biological barriers, primarily separating the blood circulation from tissue compartments. These systems have potential applications in toxicity, disease modelling, and drug development given that barrier tissues are the major hurdles in drug delivery and are closely linked to numerous prevalent human diseases. Because one of the primary functions of barrier tissues is to separate two different environments by controlling the transport of solutes, the ability to quantify transport in a barrier model is critical. Among the quantification techniques, transepithelial electrical measurements enable real-time monitoring and are label-free and non-invasive. While they are easy to carry out only by means of extracellular electrodes, it is challenging to perform transepithelial electrical measurements in miniaturized cell culture channels, hence to be integrated in MPS. Furthermore, they are difficult to interpret because they reflect a combination of many cellular electrical parameters.

This PhD dissertation is focused on the development of two compartmentalization strategies for modelling biological barriers and especially on the integration of sensing capabilities to perform in situ measurements of transepithelial parameters. The main objectives of the thesis are defined as follows:

1. To study and propose an optimal electrode configuration suitable for performing transepithelial electrical measurements in miniaturized cell culture channels.
2. To develop and experimentally validate a MPS with the proposed electrode configuration.
3. To develop a microfluidic cell culture device that addresses the incorporation of multiple barrier tissues and its real-time monitoring in a single device for application to organ-on-a-chip technology.

1.2 | DISSERTATION OUTLIN

This PhD thesis is divided into six chapters (including this one) which are summarized below.

The <u>second chapter</u> describes general knowledge about biological barriers and different methods to quantify their barrier function by means of transepithelial electrical resistance (TEER) measurements. A review of the state of the art on engineered barrier models has been also included in this chapter.

Motivated by the discrepancies between TEER values reported in the literature [7], the <u>third chapter</u> presents a numerical study to assess the accuracy of TEER measurements in Transwell and microfluidic cell cultures. This study is carried out taking into account common electrode configurations found in the literature and an interdigitated electrode (IDE) configuration proposed in this dissertation. Importantly, it is highlighted a possible error in TEER measurements that can be solved by the application of a correction factor.

The fourth chapter describes the development and experimental validation of a modular perfusion chamber with integrated electrodes as defined in the previous chapter. A dynamic in vitro model of the renal tubule is created for that purpose. As a novelty, the same electrodes are used for the continuous and simultaneous monitoring of transepithelial electrical parameters and transepithelial NaCl transport—which is a primary function of the renal tubule.

To address the challenge of interconnecting several barrier tissues in a single microfluidic cell culture, the fifth chapter explores a novel compartmentalization strategy consisted of a crisscross pattern of microgrooves on a glass substrate. In addition, electrodes are integrated in the substrate for the electrophysiological monitoring of the barrier tissues. As a proof-of-concept, it is used to recapitulate the cell structure of the retina mimicking the two biological barriers that separate the retina from the systemic blood circulation.

Finally, the sixth chapter gives a brief overview of the topic and summarizes the conclusions of the presented PhD dissertation. It is also discussed the future work to apply the developed systems in disease modelling, primarily as advanced tools to accelerate translational medicine. Finally, future perspectives of MPS are outlined.

1.3 | THESIS FRAMEWORK

The work presented in this PhD dissertation has been developed in the framework of the following projects:

1. SEPCELLS: Registro de células epiteliales con sensores desarrollados con microtecnologias (DPI2011-28262-C04-04, Proyectos de Investigación Fundamental No Orientada 2011)
2. Micro-BRB: Ruptura de la barrera hematorretiniana: causa o consecuencia de la retinopatia diabetica? (SAF2014-62114-EXP, Explora Tecnologia 2014)
3. Organ on a chip (Proyecto Intramural Especial (CSIC) 201450E116)

1.4 | REFERENCES

[1] Ahadian S, Civitarese R, Bannerman D, et al. Organ-On-A-Chip Platforms: A Convergence of Advanced Materials, Cells, and Microscale Technologies. *Adv Healthc Mater* 2018; 7: 1700506.

[2] Bhatia SN, Ingber DE. Microfluidic organs-on-chips. *Nat Biotechnol* 2014; 32: 760–772.

[3] Huh D, Matthews BD, Mammoto A, et al. Reconstituting Organ-Level Lung Functions on a Chip. *Science* 2010; 328: 1662–1668.

[4] Hessheimer AJ, Parramón D, Guimerà A, et al. A Rapid and Reliable Means of Assessing Hepatic Steatosis In Vivo Via Electrical Bioimpedance. *Transplantation* 2009; 88: 716–722.

[5] Guimera A, Gabriel G, Plata-Cordero M, et al. A non-invasive method for an in vivo assessment of corneal epithelium permeability through tetrapolar impedance measurements. *Biosens Bioelectron* 2012; 31: 55–61.

[6] Genescà M, Ivorra A, Sola A, et al. Electrical bioimpedance measurement during hypothermic rat kidney preservation for assessing ischemic injury. *Biosens Bioelectron* 2005; 20: 1866–1871.

[7] Odijk M, Meer AD van der, Levner D, et al. Measuring direct current trans-epithelial electrical resistance in organ-on-a-chip microsystems. *Lab Chip* 2015; 15: 745–752.

2

Engineering and monitoring epithelial and endothelial barrier models

Epithelia and endothelia delineate tissue compartments and control their environments by regulating the passage of ions and solutes. This barrier function is essential for the development and maintenance of multicellular organisms, and its dysfunction is associated with numerous human diseases. Recent advances in biomaterials and microfabrication technologies have evolved *in vitro* approaches for modelling biological barriers. Current MPS have become more efficient and reliable in mimicking the cell microenvironment. Additionally, electrophysiological approaches for the quantification of barrier functions have long provided significant insight into their underlying mechanisms. In this chapter, after introducing how epithelial and endothelial cells form functional barriers and describing some primary biological barriers of the human body, it is outlined the current techniques to electrophysiologically quantify the barrier function of engineered tissues, focusing on transepithelial measurements and their impedance analysis. Then, common microfabrication techniques that are used to construct MPS are described. Finally, it is given an overview of recent MPS for modelling biological barriers that emulate the cell microenvironment and microarchitecture of native tissues.

Most of the contents of this chapter have been published in:

[1] Ortega-Ribera M, **Yeste J**, Villa R, Gracia-Sancho J. Chapter 18 - Biomaterials for the treatment of liver diseases. In: Mozafari M, Rajadas J, Kaplan D (eds) *Nanoengineered Biomaterials for Regenerative Medicine*. Elsevier, 2018, p. 464.

[2] **Yeste J**, Illa X, Álvarez M and Villa R. Engineering and monitoring epithelial and endothelial barrier models. *J Biol Eng*. **Submitted**.

2.1 | INTRODUCTION

Physical barriers to separate different compartments are essential for the development and maintenance of multicellular organisms and are integral to numerous organs. Epithelia and endothelia form these vital barriers. They delineate tissue compartments and control their environments by regulating the passage of ions and solutes [1]. Some examples are renal tubule epithelium and blood capillaries. The physiological function of these biological barriers is diverse among tissues and responds to the particular needs of each organ, including the supply of nutrients, the absorption of ions, the secretion of waste, the protection against toxins, and the filtration of fluids. The deregulation of their essential function can lead to serious health complications. Numerous endothelia and epithelia dysfunctions are associated with prevalent human diseases such as hereditary diseases (e.g., hypomagnesemia), gastrointestinal tract diseases (e.g., Crohn's disease), or viral infections (e.g., hepatitis C) [2–4].

To date, diverse engineered systems have been developed for modelling human diseases [5] and also for mimicking biological barriers of the lung [6], kidney [7], and brain [8], among others. Since the major function of a cell barrier is to regulate and to separate two distinct physiological compartments, the strategy to build more relevant *in vitro* models usually lies in compartmentalization of different environments [9]. Most engineered cell barrier approaches utilize physical interfaces for such propose and to support cells (e.g., permeable membranes or gel-liquid interfaces).

Besides compartmentalization, quantifying the permeability of barrier tissues is necessary to assess the state of the barriers. For example, in toxicology, the barrier integrity is usually monitored to evaluate the effects of toxic compounds or, in disease modelling, to examine a barrier breakdown during a disease progression. In addition to tracer assays and immunocytochemistry, transepithelial electrical measurements—performed with extracellular electrodes in apical and basal sides—have been an essential methodology to quantify ion permeability and to elucidate important epithelial properties. These electrical measurements are non-invasive and yield information about the voltage, resistance, and current across the epithelium. Measuring these parameters under special conditions, it is possible to determine ion transepithelial transports and the electromotive forces generated by active transporters. Transepithelial electrical properties have been also used to determine ion selectivity, ion permeability, and electrophysiological characterization of epithelial tissues [10–12]; these measurements are widely used.

2.2 | EPITHELIAL AND ENDOTHELIAL TISSUES

Epithelial and endothelial sheets are formed by cells that are attached together sealing the intercellular space. This leads to two possible routes for solutes to cross the barrier: 1) the transcellular pathway in which ions and molecules pass through the cell membrane and 2) the paracellular pathway where solutes cross between cells (Figure 2-1a). Ion and molecules movement along the paracellular route requires a driving force such as a concentration gradient, an electrical potential difference, a hydrostatic pressure, or an osmotic gradient. In a chemical gradient, particles diffuse from an area of high concentration to an area of low concentration. Otherwise, a potential difference solely exerts force on charged particles; cations are moved towards the lower potential, while anions are flowed in opposite direction. The combination of both energies leads to an electrochemical gradient which is usually the main responsible for ion passive transport. In order to move substances against their electrochemical gradient, cells have active transcellular mechanisms of transport involving transmembrane proteins. This active transport co-exists with the passive one in the transcellular route.

The permeability of cellular barriers is very dynamic and responds to extracellular stimuli and mediators by a cascade of signalling mechanisms [13] involving a cross-talk between paracellular and transcellular pathways [14]. For example, the kidney finely controls the whole body balance of calcium, phosphate, and magnesium by regulating the reabsorption of these ions in the renal tubule [15]. Another signalling cascade is initiated in blood vessels resulting in increased permeability when they are subjected to inflammatory stimuli, such as thrombin or tumour necrosis factor alpha (TNF-α) [16]

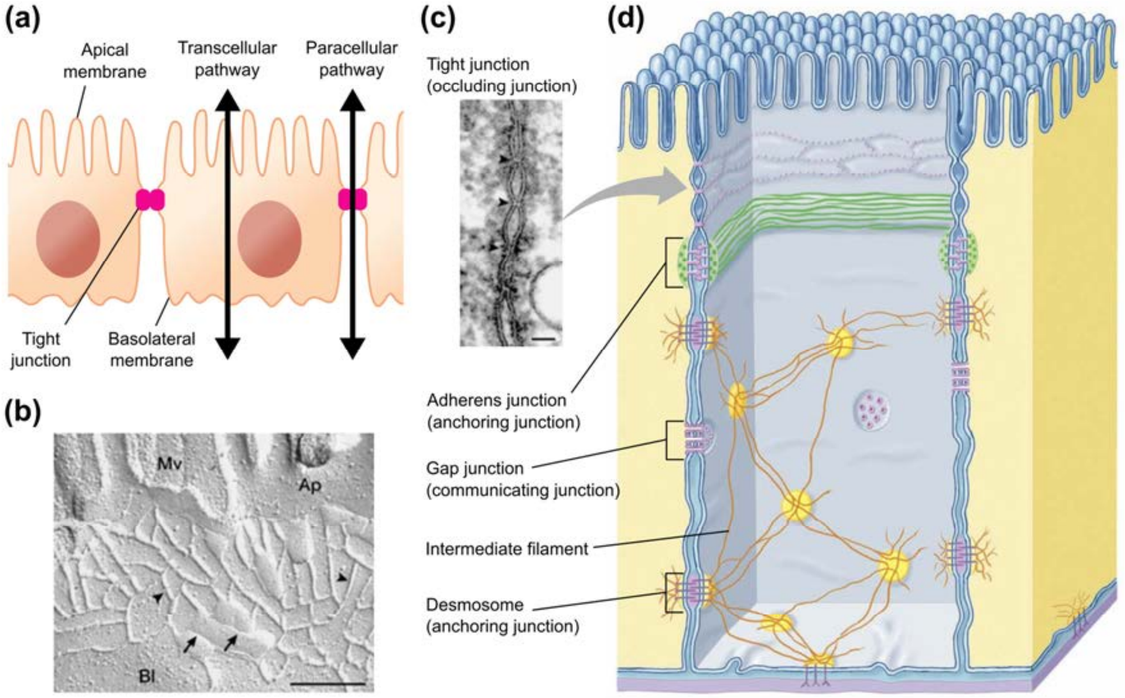

Figure 2-1 Transepithelial transport routes and intercellular junctions. (a) Paracellular and transcellular pathways across an epithelial layer. (b–c) Structure and localization of TJ strands including (b) freeze-fracture replica electron microscopic image (scale bar, 200 nm) and (c) ultrathin sectional view (scale bar, 50 nm). Mv, microvilli; Ap, apical membrane; Bl, basolateral membrane. Adapted by permission from Macmillan Publishers Ltd: Nature Reviews Molecular Cell Biology [1], copyright 2001. (d) Schematic representation of the intercellular space and the junctional protein complex - Adapted from Mescher A L 2013 *Junqueira's Basic Histology: Text and Atlas* (New York, NY: McGraw-Hill Education / Medical).

The proper functioning of an epithelial tissue depends on the polarization of cells by different membrane lipids and protein on their apical and basolateral sides [17]. The close contact between cells makes possible this apicobasal membrane polarity preventing the intermixing of specialized apical and basal membrane components. Each cell type has its particular junctional complex with a mixture of different types of cell-cell junctions (Figure 2-1b and Figure 2-1d). There are basically four types of well-differentiated intercellular junctions between adjacent cells: 1) gap junction channels link the cytoplasm of two cells and serve to exchange ions and small molecules, 2) desmosomes and 3) adherens junctions contribute to physically anchor the cells together, and 4) tight junctions (TJ) bring closer apposed membranes, being the main responsible for controlling the passive transport of solutes through the paracellular pathway [18, 19].

2.2.1 | Tight junctions

TJ are composed of integral membrane proteins involving transmembrane proteins and cytoplasmic plaque proteins for anchoring and communicating the former to the cytoskeleton. All these proteins interact with each other to form a complex protein network [20]. Transmembrane proteins are found within plasma membrane as a branching network of strands. Each strand in turn is associated with another strand from the apposed membrane creating close contact points, the so-called ’kissing points‘. Thus, the intercellular space is obliterated along strands (Figure 2-1c). The number of strands is variable and differs among cell types. Claude *et al*. observed that the junctional tightness was logarithmically related to the number of strands instead of proportionally related, which led him to propose the existence of permeable pores that dynamically and randomly open and close for short periods of time [21].

The understanding of TJ has vastly increased in the recent years and particular junctional proteins have been linked to specific barrier functions. However, the underlying mechanisms regulating such functions remain to be determined [3]. In addition to the barrier function, TJ also act as a fence that restricts the diffusion of protein complexes and lipids within the plasma membrane. Thus, the TJ that are connected to the actin cytoskeleton define the interface between apical and basal domains. In polarized epithelial cells, the TJ that delineate both domains are apically localized, while in endothelial cells, they are laterally intermixed with other junction proteins.

The two major families of transmembrane proteins are occludins and claudins. The latter family has 26 members identified in humans and are expressed differently for each particular tissue. For instance, claudin-16 is expressed specifically in epithelial renal cells from a particular section of the renal tubule, whereas claudin-10 is localized in the entire renal tubule [22, 23]. New high-resolution approaches to detect flux across individual claudin-2 channel suggest the possible existence of the dynamic behaviour, proposed many years ago by Claude *et al*., in the sub-millisecond timescale [24, 25].

Thus, TJ could finely regulate the barrier permeability by this dynamically gating in addition to the more well-known modulation by protein remodelling; further studies are needed to elucidate the crystal structure of claudins and to understand their molecular basis.

It is now clear that TJ not only physically seal the intercellular space but also form permeable channels that have charge and size selectivity [26, 27]. There are evidences that strands contain ion-selective channels that account for particular ion permeation. This is possible by the formation of small pores (around 0.4–0.8 nm) for ion permeability concurrently with large pores (up to ~3–6 nm) for macromolecules. Claudins are thought to be the mediators in ion-selectivity and are grouped on those that are cation-selective, anion-selective, or simply sealing. On the other hand, macromolecules diffusion is less understood but it is thought that implies a dynamic remodelling of the strands in addition to the large pores.

2.2.2 | Barrier function

Thanks to the permeability regulation in the paracellular pathway by intercellular junctions, especially TJ, epithelial and endothelial tissues manage the transport of substances to maintain and regulate the fluid composition between distinct compartments within organs. In the following, it is briefly introduced the barrier function of some primary biological barriers found in kidney, intestine, lung, liver, and brain.

2.2.2.1 | Kidney

The kidney is responsible for the filtration of blood, the balance of body fluid, and the excretion of waste from the blood (Figure 2-2a). This is accomplished by around one million of tiny functional units called nephrons containing several endothelial and epithelial barriers. Inside each nephron, blood first arrives at the renal corpuscle where a network of endothelium capillaries (glomerulus) filters the blood permitting only the passage of water, ions, and small molecules; the rest is returned to the bloodstream. The filtrate then enters the renal tubule, which is lined by epithelial cells that selectively reabsorb diverse compounds (e.g., H_2O, NaCl, glucose, Ca^{2+}, and Mg^{2+}) and secrete other ones (e.g., urea, NH_4^+, and some drugs). Finally, the filtrate is delivered to a system of collecting ducts where it is excreted from the body in the form of urine.

2.2.2.2 | Intestinal barrier

The small intestine is part of the gastrointestinal tract; its primary function is to digest food and subsequently to absorb its nutrients in nearby capillaries. For that purpose, the intestinal tube is lined by a single-layer epithelium that acts as a selective barrier to absorb nutrients and water while preventing the passage of harmful substance (e.g., toxins and pathogenic microorganisms). In order to increase the absorptive surface area, enterocytes—the specialized absorptive cells of the intestinal epithelium—form finger-like processes that project into the lumen (villi) and contain membrane extensions in the apical surface called microvilli (Figure 2-2b). In addition, goblet cells, which are interspersed with enterocytes, are responsible for the secretion and regulation of the composition of a mucus layer that protects from pathogen invasion and regulates antigen traffic. The integrity of this intestinal barrier (i.e., epithelium and mucosa) is vital in the maintenance of gut homeostasis; their dysfunction may lead to a persistent inflammatory state contributing to pathogenesis of inflammatory bowel diseases such as Crohn's disease and ulcerative colitis [28].

2.2.2.3 | Alveolar-capillary barrier

Gas (i.e., O_2 and CO_2) exchange between air and blood occurs at saclike features called alveoli in the lung (Figure 2-2c). These structures are located at the distal ends of the respiratory bronchioles and represent the functional unit of the respiratory system. In the exchange process, the O_2 from the alveolar air diffuses into the blood in surrounding capillaries while the CO_2 is inversely released from the blood into alveoli. As a result, the deoxygenated blood arriving from the pulmonary arteriole leaves oxygenated through the pulmonary venule. The barrier that separates air from blood is called alveolar-capillary barrier or also blood-air barrier; it comprises the epithelial cells lining the alveolus (pneumocytes), the capillary endothelial cells, and the basement membrane between both cell types. The integrity of the alveolar-capillary barrier can be damaged in acute lung injury, which can result in a fluid leakage from capillaries to alveolar spaces and a subsequent pulmonary oedema with a potential risk of respiratory failure.

2.2.2.4 | Liver sinusoid

The main function of the liver is to process the nutrients absorbed from the digestive tract. In particular, it synthesizes major plasma proteins, produces bile components for digestion, and detoxifies ingested toxins. These functions are performed by hepatocyte cells, which are organized in plates and in turn are arranged radially forming lobules (Figure 2-2d). In each hepatic lobule, blood flows from peripheral vascular branches to a central vein through hepatic sinusoids. Unlike continuous capillary, sinusoids are discontinuous and fenestrated (cell perforated) capillaries, which facilitate the diffusion of solutes (e.g., nutrients, proteins, and toxins) between hepatocytes and plasma. This unique liver sinusoidal endothelial cell (LSEC) phenotype—including fenestration and lack of a basement membrane—is vital in maintaining functional hepatocytes. Dysregulation of the LSEC phenotype is an early stage of liver fibrosis that can progress to cirrhosis and liver failure [29], which can only be treated by liver transplantation.

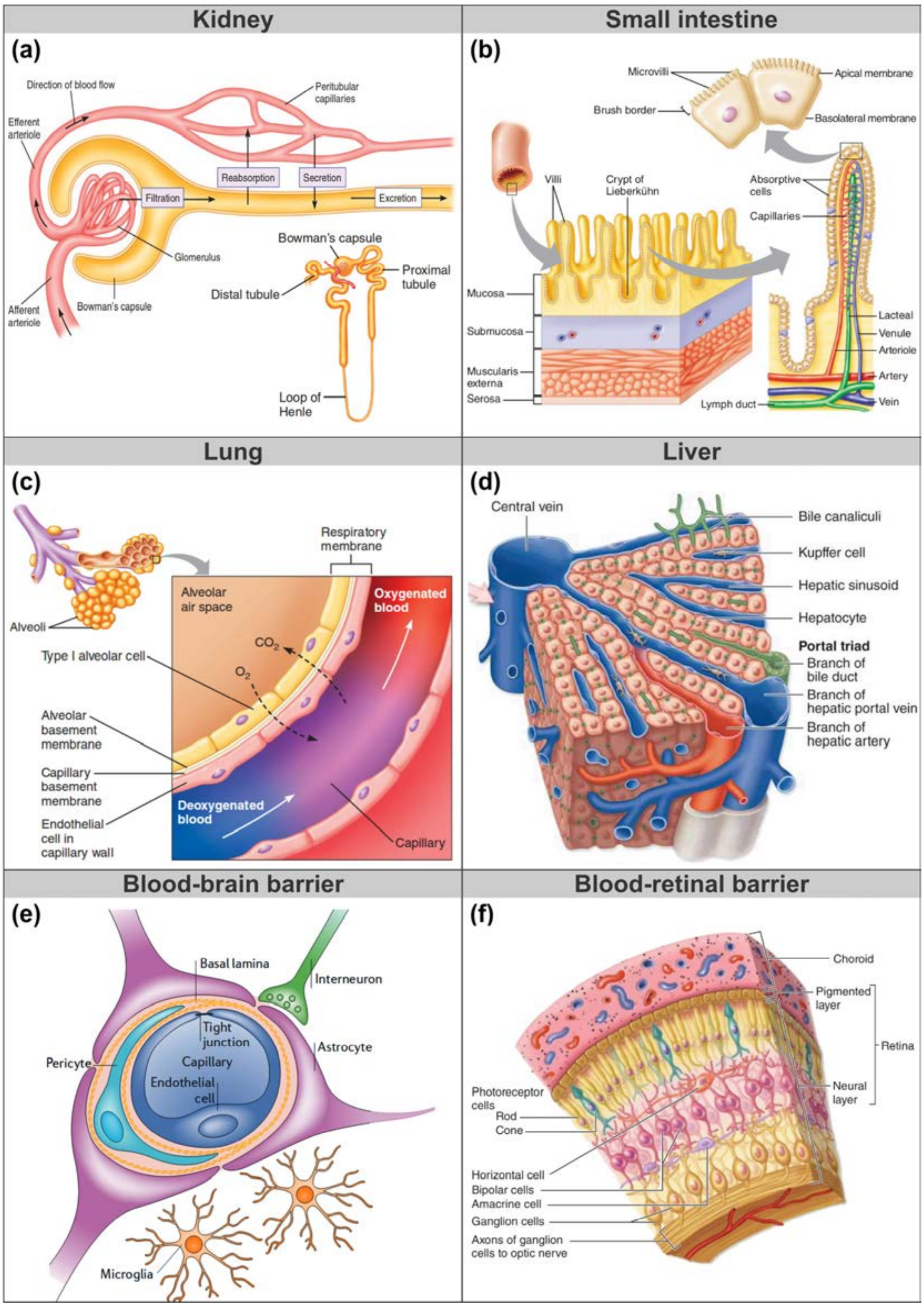

Figure 2-2 Illustrations of primary endothelial and epithelial barriers in the kidney, intestine, lung, liver, and brain. (a) Exchange processes in the renal nephron including filtration through the glomerulus and reabsorption and secretion along the renal tubule. (b) Small intestinal villi. (c) Gas exchange in the lung alveoli. (a–c) Adapted from Stanfield C L 2013 *Principles of human physiology* (Boston, MA: Pearson Education). (d) Liver sinusoid and plate of hepatocytes. (e) Blood-brain barrier formed by capillary endothelial cells surrounded by basal lamina and perivascular astrocytic end-feet. Adapted by permission from Macmillan Publishers Ltd: Nature Reviews Neuroscience [40], copyright 2006. (f) BRB comprising the inner BRB formed by microvessels of the optic nerve and outer BRB formed by the retinal pigmented epithelium. (d,f) Adapted from Mescher A L 2013 *Junqueira's Basic Histology: Text and Atlas* (New York, NY: McGraw-Hill Education / Medical).

2.2.2.5 | Blood-brain barrier

The blood-brain barrier (BBB) is a primary barrier in the brain that separates the blood from the central nervous system (CNS) [30, 31]. The BBB is formed by endothelial cells lining cerebral capillaries and microvessels surrounded by perivascular astrocytic end-feet (Figure 2-2e). Its main function is to protect the brain from potentially harmful substances (e.g., bacterial toxins and infectious agents), while homeostasis of the CNS tissue is preserved providing essential nutrients and gases. Brain capillary endothelium is among the tighter endothelia in the human body, in which well-developed tight junctions severely restrict the passage of solutes. Diverse neurological diseases—stroke, epilepsy, Alzheimer's disease, and multiple sclerosis, among others—share common BBB disruption that contributes to the severity of such diseases [32]. Understanding the underlying mechanisms regulating the BBB would be beneficial for the development of new strategies to delay diseases progression. In addition, delivering therapeutic agents to the brain presents a challenge because of the tightness of the BBB. To overcome this obstacle, strategies for drug delivery have been focused on drug manipulation and temporarily disruption of the BBB [33], although the latter has a high risk of brain injury due to the possible entry of circulating toxins.

2.2.2.6 | Blood-retinal barrier

The blood-retinal barrier is similar to the BBB but protecting the nervous tissue of the retina. The BRB comprises two barriers: the inner and the outer BRB (Figure 2-2f). The inner BRB separates the neuronal retina from the circulating blood and consists of endothelial cells lining microvessels [34]. The role of the BRB is to protect retinal neural tissue from potential harmful molecules circulating in the blood while supplying nutrients to the retina. At the opposite posterior part of the retina, the retinal pigmented epithelium forms the outer BRB which regulates the entrance of solutes from the vascular choroid to the neural retina. This cell layer, in which the apical side faces retinal photoreceptors in the outer part of the retina, transports the high nutrient requirements for photoreceptors, absorbs scattered light, and removes free radicals, among other functions. Both barriers are sealed by tight junctions that mediate highly selective diffusion of molecules. Alterations of the BRB are directly associated with two leading cause of blindness in developed countries: diabetic retinopathy and age-related macular degeneration.

2.2.3 | Cell microenvironment

There are many microenvironment factors that influence epithelial and endothelial tissues and are essential for its proper functioning (Figure 2-3). For example, most epithelia produce an extracellular matrix (ECM) that support them and interface with other tissues acting as a diffusion barrier for the exchange of molecules. Moreover, cells react to physical and biochemical stimuli in the surrounding environment, which allows them to interact with other cell types and to dynamically adapt their barrier function to particular physiological needs.

2.2.3.1 | Extracellular matrix

The ECM is a three-dimensional structure fundamentally composed of water, proteins, and polysaccharides that physically supports cells within the organs [35]. Components of the ECM are produced by cells and secreted into the extracellular space where they are assembled into diverse structures, primarily collagen fibres. There are two general organizations of ECM depending on their localization and composition: 1) the basement membrane, which is a sheet-like layer mostly composed of collagen IV and laminins that separates epithelia from connective tissue; and 2) the interstitial matrix, which surrounds cells forming a porous scaffold for tissues and mainly consists of collagen I and fibronectin. In addition to act as physical support for cells, the ECM regulates many essential cellular functions such as proliferation, migration, differentiation, and cell fate [36, 37]. Rather than being a rigid and static matrix complex, the ECM is constantly interacting with surrounding cells and remodelling itself to maintain tissue homeostasis. Cell-ECM interaction is mediated via biochemical signals coming from membrane receptor proteins (e.g., integrins) that link the matrix to the cytoskeleton and activate intracellular signalling pathways. Thus, ECM dictates important cellular behaviours. For example, Cell-ECM adhesion by specific membrane receptors marks an asymmetry of the cell surface that is involved in the establishment of cell polarity [38]. In addition, dysregulation of the ECM in pulmonary fibrosis—in which there is an excessive collagen deposition and a matrix remodelling—may undergo alveolar epithelial-mesenchymal transition (EMT) (a biological process by which polarized epithelial cell acquires a mesenchymal phenotype), thereby compromising lung epithelial barrier function [39].

2.2.3.2 | Cell-cell communication

Cell to cell interaction through messaging signals is fundamental to cooperate and thus succeed in the maintenance of tissue homeostasis. This communication is typically established using signalling biomolecules and can be divided into four categories depending on the distance between the sending cell and the receiving cell: 1) direct contact in which cells share some binding molecules or in which small molecules diffuse between apposed cells via gap junctions, 2) autocrine signalling where a molecular messenger is released and subsequently bound to the same cell, 3) paracrine signalling where the signal reaches a nearby cell, and 4) endocrine signalling in which hormones travel long distances through the bloodstream and reach distant target cells. Heterotypic cell-cell interaction is necessary to maintain the barrier function of most epithelial and endothelial tissues. For example, although the BBB is physically created at the vascular endothelium, surrounding cells (e.g., pericytes, astrocytes, and neurons) have been found to play an important role in the barrier regulation [40]. For instance, pericytes are essential during BBB development [41], and their lack or the disruption of

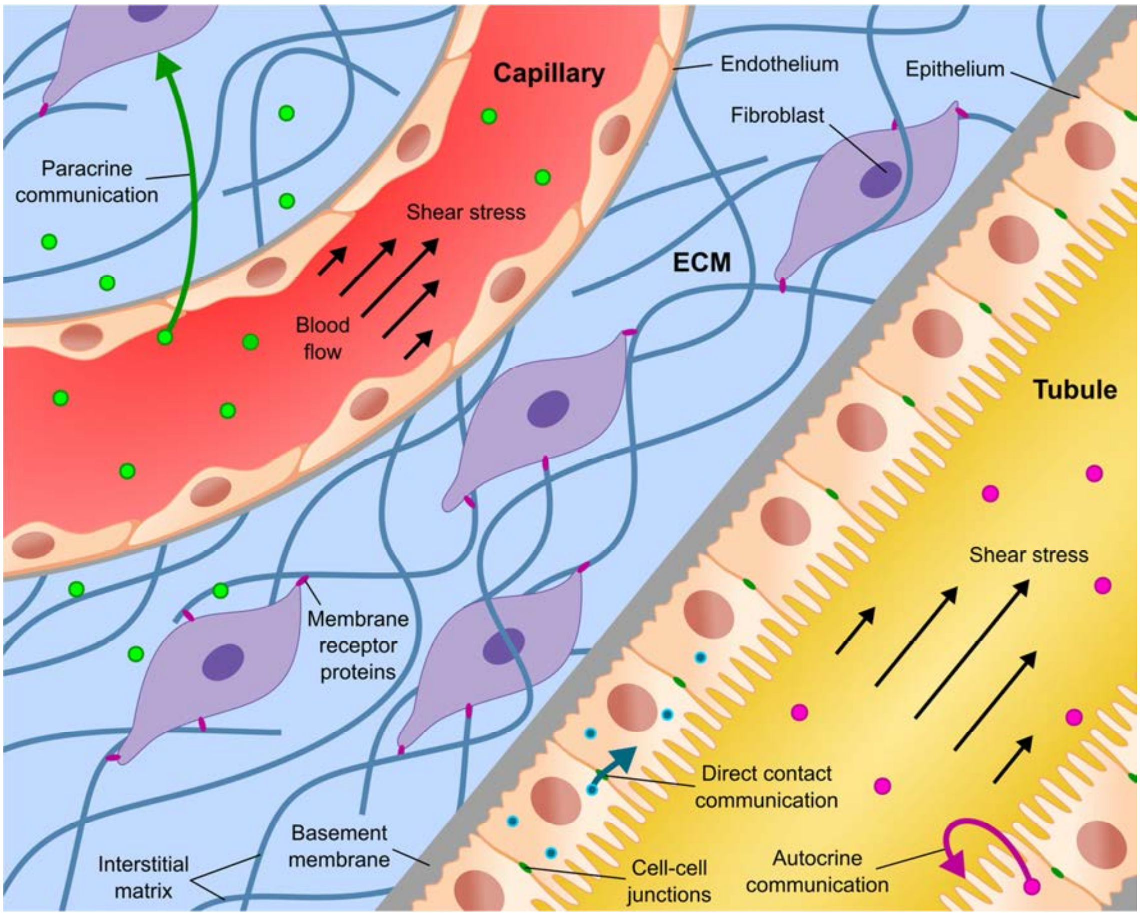

Figure 2-3 Physical and biochemical cues in the cell microenvironment. Schematic drawing of an epithelial tubule and an endothelial capillary embedded within an ECM. It includes cell-cell communications (i.e., direct contact, autocrine, and paracrine communications), flow-induced shear stress, ECM involving basement membrane and interstitial matrix components, and cell-ECM interaction through membrane receptor proteins.

their interaction with endothelial cells disrupt the BBB integrity [42, 43]. Moreover, in cultures of LSECs, the incorporation of supportive cells (i.e., hepatocytes and fibroblasts) prolongs survival and the expression of LSEC phenotypic markers *in vitro* [44].

2.2.3.3 | Biochemical cues

Some soluble factors such as hormones, cytokines, and growth factors serve as extracellular signal molecules for cell signalling and regulate fundamental cellular processes in barrier tissues. These biomolecules act as ligands that bind to cell surface receptors activating biochemical signalling. For example, growth factors stimulate cell growth, cell proliferation, and cell differentiation. In addition, a multitude of cytokines have been found to modulate epithelial barrier functions. In the gut, mucosal inflammation increases epithelial permeability via TJ disassembly, in part because activated immune cells release certain inflammatory cytokines [45, 46]. Indeed, specific cytokine inhibitors are used to restore homeostasis in intestinal inflammation. Similar increased permeability have been demonstrated in other epithelia such as airway epithelium when these are exposed to certain cytokines such as TNF-α and interferon gamma (IFN-γ) [47]. In the BBB, interleukins (IL-1α, IL-1β, and IL-6) and TNF-α cause the disruption of the barrier increasing the ion permeability of the BBB [48, 49]. In contrast, other chemical agents like some hormones (e.g., adrenomedullin and hydrocortisone) have the opposite effect on the BBB by tightening and strengthening the barrier [50, 51].

2.2.3.4 | Physical cues

Besides the biochemical cues, cells are able to sense the external physical environment such as the topography and the stiffness of the ECM. These physical features are transduced into a biochemical response through integrin-based adhesions complexes in a process known as mechanotransduction [52]. In particular, matrix stiffness regulates proliferation, migration, and cell-cell adhesion, among others, and its stiffening can lead to the progression of tumour angiogenesis [53], while the topography of the underlying ECM influences cell morphology and cell differentiation, among others [54]. For example, differentiation of stem cells into a specific cell type is not only a process regulated by biochemical cues but also by biomaterial elasticity and topography [55].

Other physical forces, like the hemodynamic shear stress and intercellular forces through adherent junctions, coexist in the cell microenvironment and critically influence cell function and cell behaviour. Endothelial cells lining blood vessels are constantly exposed to a fluid shear stress (FSS) acting on vessel walls in the direction of the blood flow. A sustained physiological variation of the FSS has been found to stimulate vascular remodelling and to increase nitric oxide production by endothelial cells [56, 57]. In addition, many *in vitro* and *in vivo* studies have reported a shear-dependent endothelial permeability [58]. As in blood vasculature, FSS is also a relevant physiological stimulus for epithelial tissues. For example, renal tubular epithelial cells are exposed to a FSS on account of the filtrate flowing across the tubular lumen and are able to transduce this mechanical force at microvilli and primary cilia processes. There are evidences that the glomerulotubular balance, which maintains a constant fraction of the filtered load resorbed, is possible in part because of this FSS mechanotransduction that would regulate ion and water reabsorption depending on the flow rate [59].

2.3 | ELECTROPHYSIOLOGICAL QUANTIFICATION OF THE BARRIER FUNCTION

Transepithelial electrical measurements have been largely used to quantify ion permeability and barrier function in cell cultures. Its major advantages are the non-invasiveness and the real timing of the measurement. On the contrary, tracer assays require long time periods for tracers to diffuse, and immunocytochemistry is qualitative and needs labelling. As a disadvantage, transepithelial electrical measurements are difficult to interpret because they are the result of a combination of many cellular electrical parameters. For this reason, some assumptions and simplifications are usually considered to interpret the results. This technique is based on the measurement of the electrical properties of the cellular sheet by means of extracellular electrodes. In particular, a voltage or current perturbation is applied between electrodes placed in both sides of the barrier. The measurements that give primary information about a cellular barrier are transepithelial voltage (V_{te}), transepithelial electrical resistance (TEER), and short-circuit current (I_{sc}). These parameters are related by Ohms law as

$$\text{TEER} = \frac{\Delta V_{te}}{\Delta I} \tag{2-1}$$

where ΔV_{te} is the change in V_{te} and ΔI is the change in the current flowed.

Transepithelial voltage. The net movement of ions across epithelia may lead to a charge imbalance between apical and basolateral sides that generates a transepithelial potential difference; this will be the sum of both apical and basolateral membrane voltages. In epithelial tissues, the transepithelial ion transport is driven by active transporters, chemical gradients, and electrical forces due to potential differences.

Transepithelial electrical resistance. TEER is the paracellular sum of two ion conductive pathways, the paracellular resistance and the transcellular resistance. This parameter is often used to monitor the cell barrier integrity during experiments and to electrically characterize barrier tissues. For example, epithelia and endothelia are traditionally grouped in two classes according to their transepithelial resistances: 1) 'leaky' epithelia when they have low TEER values and lower paracellular resistance compared to the transcellular one, and 2) 'tight' epithelia in which the TEER is much higher and the paracellular and transcellular resistances are similar.

Short-circuit current. Under particular experimental conditions in which there is no electrochemical gradient across the epithelium (i.e., apical and basal solutions are the same, and V_{te} is clamped to zero), active ion transport generates a measurable electrical current, the so-called 'short-circuit current' (I_{sc}). Although this current represents the net transport of all ions species, the active transport of one ion species could be estimated from I_{sc} variations when removing such ion from the solution.

2.3.1 | Equivalent electric circuit

The transepithelial impedance across a cellular monolayer can be described in terms of an electric circuit containing resistances and capacitances. In the most complete equivalent electric circuit (Figure 2-4a), there are 1) two capacitances (C_a and C_b) that represent the apical and the basolateral cell membranes, 2) two resistances (R_a and R_b) that describe the ion permeability of the cell membranes, and 3) a paracellular resistance (R_p) to represent the selective ion route through the TJ. An additional resistance (R_s) is often added in the circuit to describe the solution resistance between

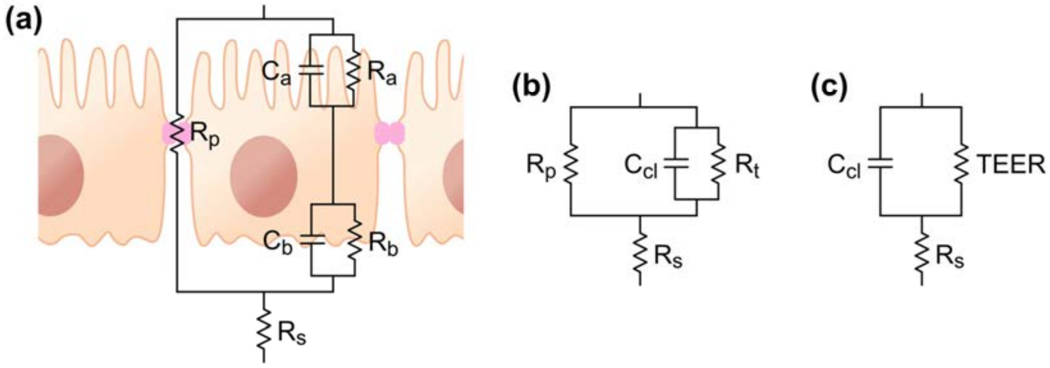

Figure 2-4 (a) Equivalent electric circuit for an epithelial cellular layer. (b) Model with lumped apical and basolateral elements. (c) Lumped model including only transepithelial electric resistance (TEER) and cell layer capacitance (Ccl). Rp, paracellular resistance; Rs, resistance of the solution; Ra, apical resistance; Rb, basolateral resistance; Ca, apical capacitance; Cb, basolateral capacitance; Rt, transcellular resistance.

the electrodes and the cell layer. This five-variable model has to be solved with additional measurements; however, it is possible to obtain a two-variable model by lumping the elements. In a first step, the contributions from apical and basolateral membranes are grouped in a single transcellular resistance (R_t) and a cell layer capacitance (C_{cl}) (Figure 2-4b). This can be done if R_aC_a and R_bC_b are similar. In a second step, the transcellular and the paracellular resistances are grouped in the TEER (Figure 2-4c).

Although the simplified model containing the TEER and the C_{cl} provides primary information about the cell barrier, sometimes it is necessary to solve the entire system. For example, it is often interesting to determine the particular ion permeability of TJ or to distinguish the electrical parameters of both membranes. For such purposes, one of the five parameters can be independently obtained and used to determine the others. In other approaches some parameters may be neglected when they do not contribute to the overall impedance (e.g., the TEER is dominated by the R_p in leaky epithelia where the R_p is much lower than the R_t).

2.3.2 | Impedance analysis

Representative impedance spectra obtained across a cell layer are shown in Figure 2-5 for the frequency range of interest (~10 Hz–1 MHz). They are simulated for different values of TEER and C_{cl}, respectively. The spectra show three well-differentiated frequency regions. At relatively high frequencies (>100 kHz), the impedance is purely resistive (phase = 0 °) and dominated by the R_s. This resistance is not altered by the cellular layer but can be affected by changes in the solution. Otherwise, at low frequencies (<100 Hz), the impedance is also resistive but associated with the TEER in series with the R_s. An advantage of impedance spectroscopy is the discrimination between R_s and TEER unlike measurements systems using a single frequency. In the frequency range ~100 Hz–100 kHz, the impedance denotes a relaxation associated with the C_{cl}. The increase of the C_{cl} results in a shift towards lower

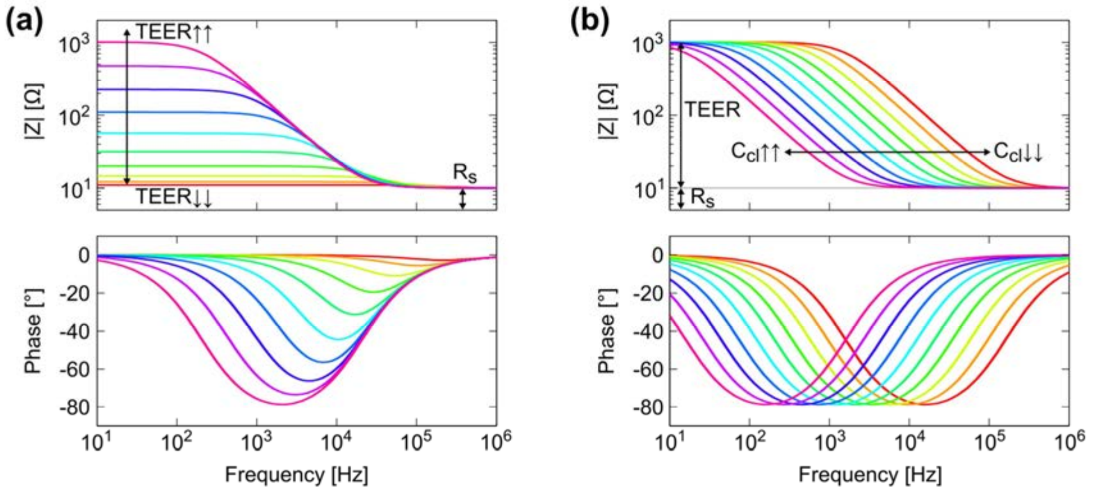

Figure 2-5 Representative impedance spectra across a cell layer; data was simulated with Rs equal to 1 kΩ, TEER values ranging 1–1000 Ω, and Ccl values ranging 0.1–10 µF.

frequencies of the relaxation whether the decrease of the C_{cl} shifts it towards higher frequencies.

2.3.3 | Measurement techniques

2.3.3.1 | Ussing chamber

The Ussing chamber was an apparatus developed by the Danish biologist Hans H. Ussing [60] in the early 1950s to measure the active transport of sodium in frog skin epithelium. Ussing and Zerahn demonstrated that the rate of active transport of ions can be calculated as an electric current across the skin if both sides are at the same potential and have similar solutions [61]. By imposing these conditions, there would be no net transfer of passive ions, and the electric current (I_{sc}) would results only from active transport processes. The original diagram representation of the apparatus is shown in Figure 2-6. It is composed of two compartments containing the same Ringer's solution (appropriately oxygenated through the air inlets) and the piece of tissue under study separating both compartments in the middle. To measure the potential difference and to pass the current across the tissue, four agar-Ringer bridges link the Ringer's solution in the compartments with reference electrodes and current carrying electrodes, respectively. The former electrodes are connected to a potentiometer for voltage sensing, whereas the latter are coupled to a battery and a potential divider in order to apply an external electromotive force for passing an electric current.

Transepithelial measurements that can be obtained from Ussing chamber include V_{te}, TEER, and I_{sc}. The V_{te} is obtained from open-circuit by reading the spontaneous potential difference. TEER is computed from Ohms law as the ratio of the change in V_{te} to the amount of current passed either by flowing a known amount of current (current-clamped) or by generating a controlled voltage step (voltage-clamped). Finally, the I_{sc} is measured clamping the V_{te} to 0 V via controlling the applied electromotive

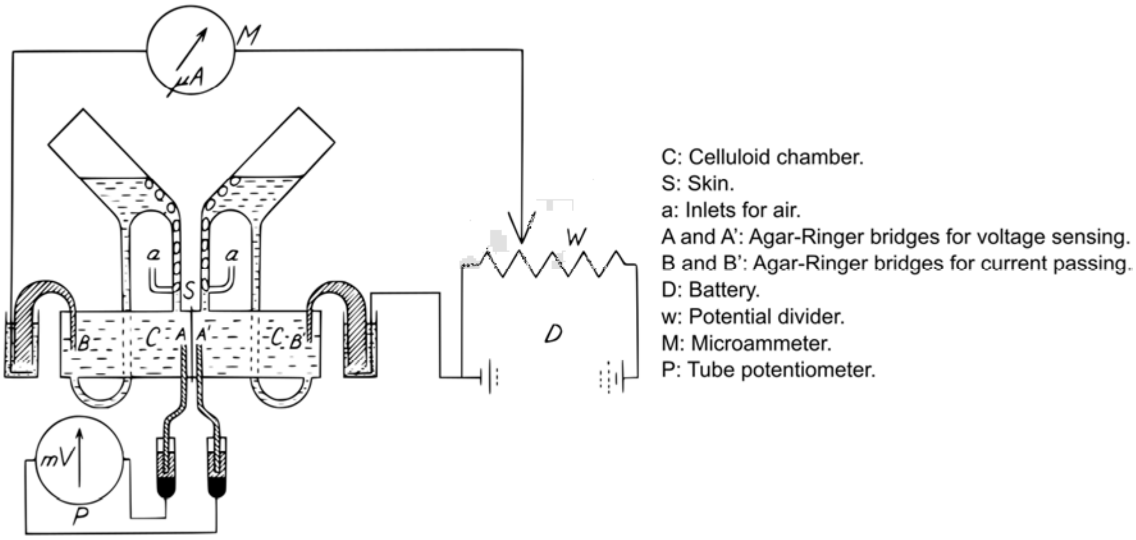

Figure 2-6 Original diagram representation of the Ussing chamber in 1951. Reproduced by permissions of John Wiley and Sons [61].

force. By combining transepithelial measurements with chemically determined net fluxes, Ussing was able to prove that the overall I_{sc} measured across the frog skin was produced by the active transport of Na^+ [61]. This was followed by other works where he demonstrated that the active transport of Na^+ in reality is a forced exchange of Na^+ against K^+ located at the inward-facing membrane [62] and also revealed the passive transport origin of the Cl^- ions [63], both remain unchanged today. Other authors rapidly adopted the Ussing chamber to study other tissues (e.g., intestinal [64], urinary bladder [65], and kidney [66]).

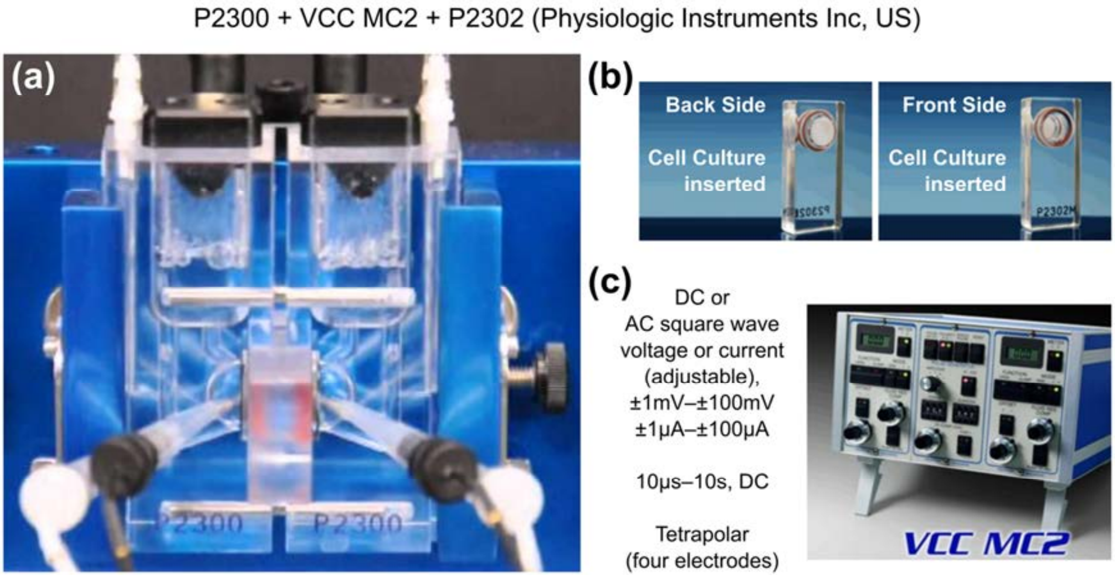

Pros: - uniform current distribution,
- ability to measure Vte, TEER, and Isc,
- compatible for mounting excised tissues.

Cons: - requires much manipulation,
- possible tissue damage during assembling,
- complicated to scale up.

Figure 2-7 (a) Commercially available Ussing-like chamber (P2300) plus (b) holder for cell culture inserts. (c) Dual channel voltage/current clamp (VCC MC2) (Physiologic Instruments Inc, US).

To date, our knowledge about active and passive transport mechanisms in epithelial tissues has vastly increased thanks to the Ussing chamber; the versatility of the apparatus is unquestionable. A primary advantage of this system is the high accuracy of the measurement because of the uniform current distribution along the epithelial sheet. Although many companies supply their own versions of the Ussing chamber, the main features of the original device are maintained (Figure 2-7). A common Ussing-like chamber can accommodate a variety of tissues using interchangeable sliders even can hold a Snapwell inserts (i.e., cell culture insert supported by a detachable ring). The tissue manipulation during assembling becomes an issue when dealing with Ussing-like chambers since this may lead to serious damage of the tissue edge. As a result, transepithelial measurements may be dramatically altered especially by shunt paths at the edges where the tissue is anchored.

2.3.3.2 | Transwell

Transwell permeable supports are cell culture inserts to be used with standard well plates mainly for transport and migration studies (Figure 2-8). In general, these devices simply comprise an insert body with a bottom filter plate. The membrane filter serves as a cell growth substrate and permits particles to diffuse through the porous of the filter (e.g., molecules and ion). Semipermeable membranes are available in a variety of specification; pore sizes are ranged from 0.4 to 8 μm depending on the application, and common materials are polyester (PET), polycarbonate (PC), or polytetrafluoroethylene (PTFE). Transwell supports have been very popular since the 1950s [67] due to their simplicity and their commercial availability. Unlike cells on culture dishes, cells grown on permeable supports have a basal side in which cells can uptake and secrete molecules. This is essential to provide an environment that better mimics the *in vivo* scenario and in turn enables cell polarization. Moreover, Transwell system facilitates the collection of samples from both tissue sides therefore permits transport studies.

Transwell models are not limited to monocultures as the bottom of the well and the opposite side of the membrane can be used to grow other cell types. Some of the human cell barriers that have been modelled with Transwell systems are the alveolar epithelium [68], BBB [69, 70], and intestinal mucosa barrier [71, 72]. Transwells obstruct direct heterotypic cell-cell contact in co-cultures where different cells types are juxtaposed on opposite sides of the membrane because of its thickness (typically 10 μm). Therefore, cell-cell interaction can be attributed exclusively to the production of soluble factors.

Figure 2-8 Transwell permeable support (Corning Life Science, Corning, NY, US).

This type of experiment has been used to identify mediators that play a major role in cell-cell communication as between human mesenchymal stem cells (hMSCs) and B-cell [73], to study the upregulation of vascular endothelial growth factor (VEGF) in co-cultures with multiple myeloma cells and bone marrow stromal cells [74], and to state that cell-cell contact is an important factor in the differentiation process of pericyte-like cells derived from stem cells [75].

The electrophysiological quantification of the barrier in Transwell cultures can be done by using a commercially available handheld probe based on chopstick-like electrodes (Figure 2-9). The probe comprises a pair of sticks with electrodes at the ends. Each stick in turn has a current carrying electrode (outer Ag electrode pair) and a pick-up electrode (inner Ag/AgCl pair). With this tetrapolar (four electrodes) configuration, it is possible to measure either the TEER or the V_{te}. The procedure to determine the TEER requires an additional measure for quantifying the contributions of the medium solution to the total resistance—the resistance can be very high when the membrane filter has low porosity (e.g., small pore size or low pore density).

A disadvantage of chopstick-like measurement systems is the proper positioning of the sticks. Since electrodes are handheld, variances in the depth or the angle of immersion may change the current distribution and thereby lowering the precision of repeated measurements. Another drawback is the non-uniform current distribution when large membrane filters are used (>12 mm in diameter), which makes normalization by the area unappropriated [76]. To overcome these limitations, chopstick electrodes can be replaced by the so-called ’Endohm series‘ (World Precision Instruments, Sarasota, FL, US). This system comprises a chamber and a cap each containing a pair of concentric electrodes. Therefore, the applied current is more uniformly distributed through the whole area providing reproducible and accurate measurements. In a comparative study, a consistent discrepancy between TEER values were found when same epithelial tissues were measured with chopstick-like electrodes and a Ussing-like chamber; measurements made with the chopsticks overestimated the TEER [77]. This discrepancy has been also reproduced in other studies [78, 79].

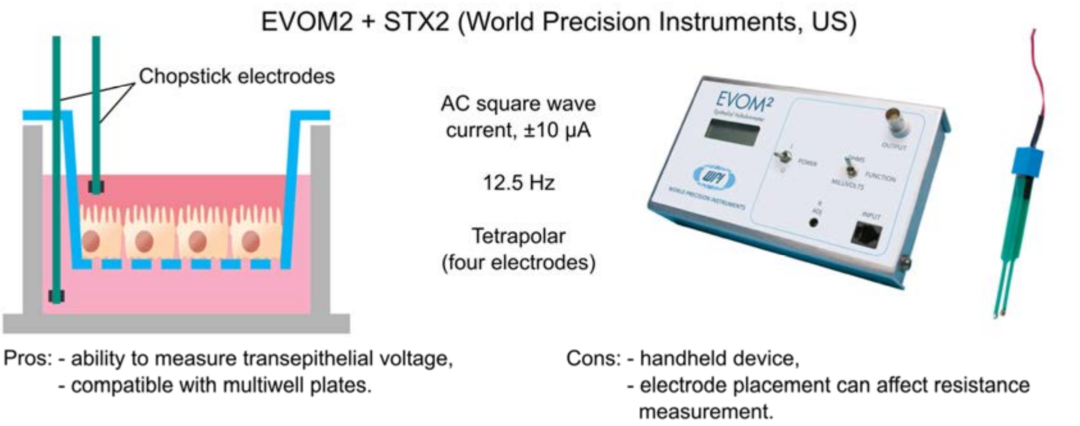

Figure 2-9 Chopstick-like electrodes for use with standard Transwell inserts (EVOM2 plus STX2, World Precision Instruments, US). EVOM, Epithelial Voltohmmete.

2.3.3.3 | ECIS

Electric cell-substrate impedance sensing (ECIS) is a technology in which cells are cultured on a surface that contains punctual sensing electrodes (Figure 2-10) [80]. The most basic ECIS cultureware for monitoring barrier function includes a small circular gold electrode of 250 µm in diameter surrounded by a relative large electrode, although there is a wide selection of electrode configurations depending on the application. This methodology measures the electrical impedance between the two electrodes in a frequency range from 25 Hz to 100 kHz. Since the working (also known as sensing) electrode is much smaller than the counter electrode, most of the measured impedance is contributed from the volume around the working electrode. As cells grow on top of this small electrode, the current path that crosses the barrier is obstructed increasing the electrical resistance. Thus, the impedance measurement directly reflects the tightness of the cell barrier [81]. Monitoring of the barrier tightness in real time has been useful in determining the role of specific proteins in the regulation of endothelial barrier function and the barrier restoration from an induced inflammatory stimulus [82]. By using different electrode designs, apart from the barrier function, ECIS technology can be used to monitor cell attachment and spreading [83], cell migration, cell proliferation, cell invasion, and cytotoxicity [84]. Electrodes can be also used for wound healing assays apart from monitoring. For such wounding purpose, a temporally elevated voltage is applied to the electrode causing the death of the cells therein. Then, the healing process can be followed in real time [85].

The number of cells that covers an ECIS electrode of 250 µm in diameter is generally in the order of hundreds; otherwise the diameter of the smallest commercially available insert is around 4.2 mm in diameter which allocates 3 orders of magnitude

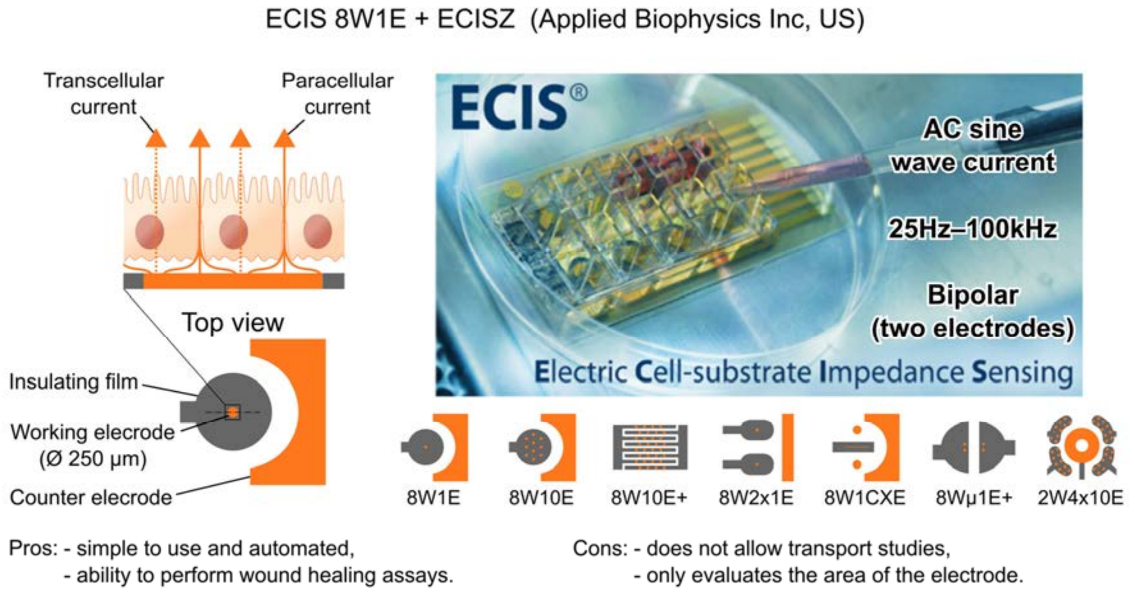
ECIS 8W1E + ECISZ (Applied Biophysics Inc, US)

Pros: - simple to use and automated,
- ability to perform wound healing assays.

Cons: - does not allow transport studies,
- only evaluates the area of the electrode.

Figure 2-10 Electric Cell-Substrate Impedance Sensing system. In this technology, cells are cultured on a surface that contains a small gold electrode (working electrode) and a large counter electrode (Applied Biophysics Inc., US).

more cells. As a result, measurements performed with ECIS technology are more sensitive to cell motility and shape of small populations of cells than methods that evaluate larger cell cultures or tissues; though a higher population of cells can be read by averaging a large collection of small electrodes. Another benefit of such experiments is the throughput and the reproducibility because of the fixed electrodes. As a disadvantage, measurements with ECIS electrodes are only representative of small areas. In addition, transport studies are not allowed in ECIS cultureware since there is no basal accessible compartment. Providing a basal region for renal epithelial cells using a porous membrane enhance cell polarization organization unlike cells cultured on flat glass substrates [86]. To create this basal region, ECIS instrumentation must be combined with insert-like filter supports by means of an adapter (e.g., 8W TransFilter Adapter, Applied Biophysics Inc, Troy, NY, US).

2.4 | MICROFABRICATION TECHNIQUES

Engineering techniques to fabricate microphysiological systems are commonly adopted from the microelectronic industry, hence the terminology ‘Organ-on-a-chip’. These techniques involve patterning, deposition, and etching processes to produce layered substrates with topographical features in the micrometre and nanometre range. These fabrication methods can be combined with other microfabrication techniques like soft lithography, where more physiologically relevant and low cost materials (e.g. elastomeric polymers) can be easily structured. In addition, the emerging 3D bioprinting is a promising tool to create complex 3D structures on demand while it is expected to become an easily accessible technology.

2.4.1 | Microelectronic technologies

Patterning a substrate is the main fabrication process that is necessary for the fabrication of the different layers that form a microelectronic device. For that, photolithography is the technique where a pattern is transferred to a photoresist that has been previously coated on a substrate. For this process, the desired geometrical pattern is defined in a transparent material (e.g., glass or PET) using opaque regions called photomask. Then, the substrate (e.g., glass or silicon wafers) is spin-coated with a thin layer of photoresist, and brought into contact with the photomask. The resist is then exposed to UV light so transparent regions are illuminated. Detailed information on photolithography technique can be found in [87]. Using positive photoresist, the exposed resist becomes soluble in a developing solution and thus removed, whereas using a negative photoresist, the unexposed resist is removed. As a result, the desired pattern is transferred to the resist on the substrate; and this could be utilized for either deposition or etching purposes.

In etching process, the unmasked regions of a substrate are physically or chemically attacked so the material is removed from the surface. There are two general types of etching methods depending on whether the etchant is in gas phase (i.e., dry etching) or liquid phase (i.e., wet etching). In dry etching the material is exposed to ion bombardment usually caused by a plasma of reactive gases. Dry etching processes can be either isotropic (same etching rate in all directions) or anisotropic (different etching rate in vertical and horizontal direction) depending on specific technology that is employed. The latter is maximized in deep reactive ion etching technique (DRIE) where very deep and narrow features can be obtained by alternative plasma etching and passivation of the lateral walls.. On the other hand, wet etching is an isotropic process where a liquid etchant chemical reaction with the unprotected substrate. This technique allows higher etching rates and has lower cost than dry etching but is inadequate for fabricating features in the sub-micron range.

Thin film deposition on a substrate is also a basic method for microfabrication. There are two established categories for this purpose depending on its chemical or physical nature. Most of the physical-based methods can be classified as physical vapour deposition (PVD) techniques, being evaporation and sputtering the most common. In the former, a source material is evaporated either thermally or by bombardment of an electron-beam, while in the latter the material is hit with gas ions to be ejected. In both techniques the atoms of the source material, which are moving freely in the environment, are then deposited on the substrate. Patterned structures can be achieved by combining this technique with a photolithography step that can be performed before the deposition using the so-called lift-off process (the resist is subsequently dissolved leaving desired pattern on the substrate; this method is called lift-off) or after the deposition (the material is then removed in an etching step and the resist is subsequently dissolved). Commonly, these techniques are used to deposit different metal layers. Chemical methods are also used to deposit thin films. In particular, in Chemical Vapour Deposition (CVD) techniques where the surface to be covered is exposed to volatile precursor gases that chemically react with thereon, are commonly used to produce nitride, oxide or carbide layers. For example, oxides and nitrides are typically deposited on top of electric tracks as isolation materials.

2.4.2 | Soft lithography

Different techniques that use "soft" materials like elastomers can be described under this category. It is especially relevant the replica moulding, where a microfabricated mould is used to replicate its pattern on an elastomeric material. Polydimethylsiloxane (PDMS) is the most popular elastomer for such purpose because it is transparent, biocompatible, and inexpensive. In addition, it can be bonded to itself and to a variety of other materials, including glass and silicon, to form multi-level structures. In this technique, the prepolymer is poured onto the mould and peeled off after being cross-linked. The obtained substrate can also give rise to a soft lithography techniques if it used as a stamp [88]. Replica moulding and microcontact printing techniques are the most representative and widely used techniques for organs-on-chips. Microcontact printing can be used to create patterns of ECM proteins onto surfaces. This is done by covering the stamp with a solution containing the protein, and bringing it into conformal contact with the surface. The stamp is then separated leaving the protein transferred in the substrate. With this technique, it is possible to create adhesive and non-adhesive regions to pattern the attachment of cells and even to create co-cultures.

The creation of microphysiological systems typically combines different elastomeric substrates fabricated via replica moulding that are finally assembled. Figure 2-11a shows the fabrication process of a microfluidic device consisting of two compartments separated by a porous membrane, in which hepatocytes are co-cultured with LSEC. Many researchers have developed microfluidic devices using a similar approach [89–91]. In general, a mould with the complementary pattern of a channel can be easily made using the SU-8 negative photoresist in a single photolithography process. In the process shown in Figure 2-11a the same mould is used to build two PDMS slabs via replica moulding that are perforated to get access to the channels. The porous membrane is then irreversibly assembled between the two PDMS slabs. The surfaces to be bonded are treated with oxygen plasma and subsequently brought into contact with each other. This plasma treatment reduces the surface hydrophobicity to promote cellular attachment and proliferation. Microfluidic channels can also be coated

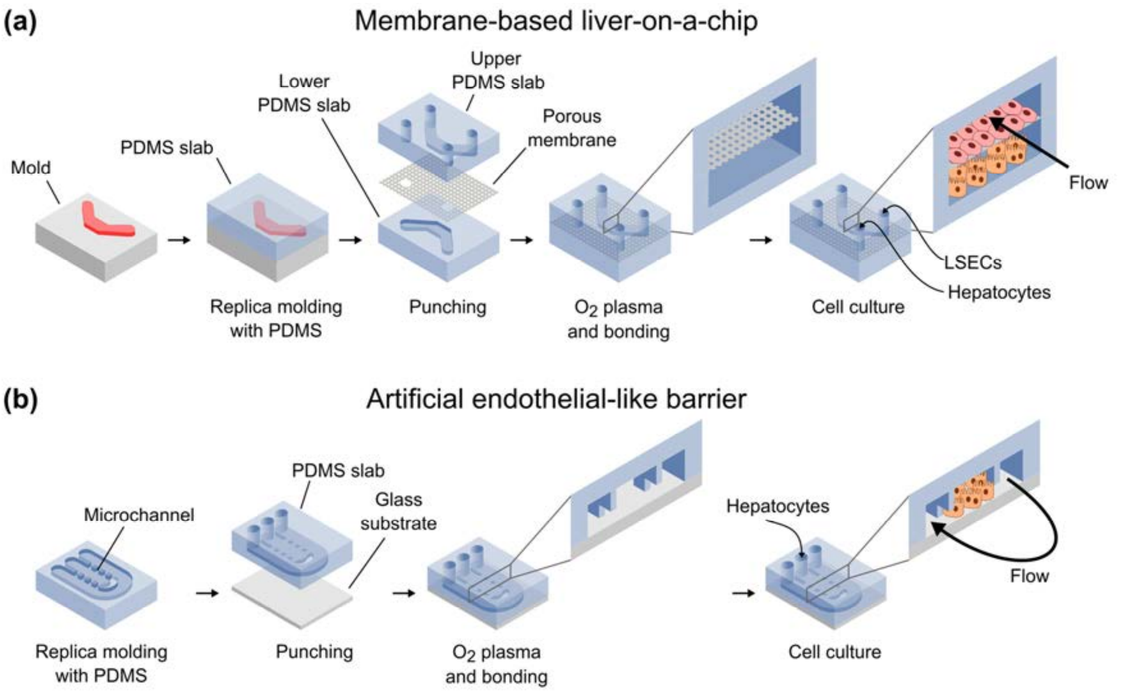

Figure 2-11 Organ-on-a-chip examples. (a) Fabrication process of a microfluidic cell culture consisting of two compartments and a porous membrane. (b) microfluidic cell culture with an artificial endothelial-like barrier of microchannels that replace the function of the LSEC. Adapted from M Mozafari, J Rajadas and D Kaplan *Nanoengineered Biomaterials for Regenerative Medicine* (Elsevier).

with ECM proteins such as collagen or fibronectin. LSEC and hepatocytes are then introduced in the upper and lower compartments, respectively. Additionally, other non-parenchymal cells can be incorporated as well. After the cells are attached, the channel containing LSEC is perfused with culture media. By using a membrane, it is possible to impose two different microenvironments; therefore endothelial cells can be subjected to FSS while cells on opposite side of the membrane would be maintained without mechanical stimuli. An important issue in this configuration is to satisfy the cells' oxygen and nutrient demand. The oxygen concentration near the cells depends on multiple factors, including channels geometry, flow velocity, number of cells, and cell consumption. The gas permeability of the PDMS facilitates the oxygenation of the cells. However, an adequate oxygen delivery must be ensured by modelling or measuring the oxygen concentration.

Figure 2-11b shows a different fabrication approach were the function of the LSEC are replaced by an artificial endothelial-like barrier made with microchannels. In this approach, which is based on the work of Lee *et al*. [92], hepatocytes are confined in a compartment surrounded by microchannels, or posters, that separate the hepatocytes from a feed channel. A PDMS substrate with the microfluidic features is fabricated like the previous example and is bonded to a flat glass substrate using oxygen plasma. Then, hepatocytes are introduced in the central compartment, and the feed channel is perfused with media.

2.4.3 | Rapid prototyping

Alternatives to soft lithography are the so-called rapid prototyping techniques [93]. These include milling [94], laser machining [95, 96], and 3D printing [97, 98]. Although they offer less resolution than soft lithography, they are less time consuming and do not require clean room facilities. Furthermore, 3D printing can be used to build complex 3D structures unlike soft lithography. This technology is advancing rapidly and is expected to have an increasing impact in microfluidic cell cultures as its resolution enhance. From the recent advances in 3D printing, it has emerged the promising technology of bioprinting. This comprises those 3D printing techniques capable of depositing biological elements such as living cells and biomaterials. The goal of this technique is to mimic living tissues for regenerative medicine or disease modelling and toxicology, among others; it basically consists in the controlled and repeated addition of bioinks (ink containing the biological material) on a received substrate. There are several methodologies for bioprinting depending on the dispensing technique; inkjet, microextrusion, and laser-assisted printing [99]. Although all of them are similar approaches, they differ basically in functional capabilities. For example, inject bioprinting is faster than the others but has worse resolution (50 µm), whereas laser-assisted printing enables single-cell resolutions [100] but requires much time of preparation. In addition, cellular viability in inject and microextrusion bioprinting is lower than in laser-assisted printing, presumably due to the physical stress on cells during dispensing.

2.5 | ENGINEERED BIOLOGICAL BARRIER MODELS

The early strategy to separate apical and basolateral domains of cell monolayers was by means of permeable supports. Epithelial cells on these membrane filters form polarized monolayers with transport and permeability qualities of *in vivo* transporting epithelia [101, 102]. Beyond these traditional cultures, MPS are refining *in vitro* models by partially emulating the cell microenvironment and the microarchitecture of native tissues. Recent advances in biomaterials and microfabrication technologies have allowed scientists to attempt novel compartmentalization approaches to develop barrier models. In the following, it is described existing strategies for modelling biological barriers involving microengineering technologies. Current compartmentalized approaches are shown in Figure 2-12.

2.5.1 | Membrane-based devices

Membrane-based devices commonly use a semipermeable membrane to split a chamber into two compartments. Most of these devices are made of thermoplastic or elastomeric materials (typically PDMS). A device based on this strategy is commercially available by Emulate Inc. (Boston, MA, US); its main field of applications have been in drug development and toxicity. In a recent study, it has been successfully used to retrospectively predict the prothrombotic side effect of a drug candidate for treatment of autoimmune disorders [103]. Importantly, this side effect was unknown during preclinical testing and was only revealed in human clinical trials. Similar membrane-based systems have been widely used in the literature to model the BBB [104, 105], the alveolar-capillary barrier [6, 106], the hepatic sinusoid [89, 107], and renal tubular epithelia [86, 108], among others. For example, Kilic *et al*. developed

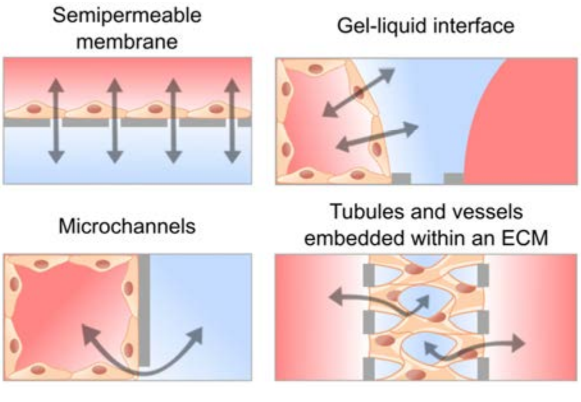

Figure 2-12 Compartmentalized approaches for engineering cellular barriers including membrane-based microfluidic device, side-by-side compartments connected through microchannels, gel-liquid interface using phaseguides, and perfusable tubules and microvascular network within an ECM.

a brain-on-a-chip platform in which human brain microvascular endothelial cells were co-cultured with pluripotent human cells differentiated into mature neuronal and astroglial cells [104]. This relevant central neuronal system environment was able to emulate the migration of neuronal progenitor cells under chemokine gradients only in the presence of the supporting endothelial cells. With this membrane-based approach, Blundell *et al*. constructed an *in vitro* model of placental barrier, which protects the foetus from harmful substances and regulates the transport of nutrients from the maternal to the foetal blood [109]. For this purpose, a co-culture of human trophoblasts (specialised placental epithelial cells) and foetal endothelial cells were plated on either side of the semipermeable membrane under flow conditions. The model reproduced the efflux transport of a gestational diabetes drug (i.e., glyburide), mostly by active transporters in trophoblast cells [110]. *In vitro* models that faithfully recapitulate transport functions of placental barrier are essential to predict the exposure of foetus to drug compounds that may compromise foetal development during pregnancy.

Instead of using a rigid permeable support, a flexible membrane (e.g., PDMS) can be utilized to apply a mechanical stretching to the cells. With this approach Hug *et al*. created a ’lung-on-a-chip‘ that models the alveolar-capillary barrier [6]. They co-cultured microvascular endothelial cells in a compartment containing culture medium

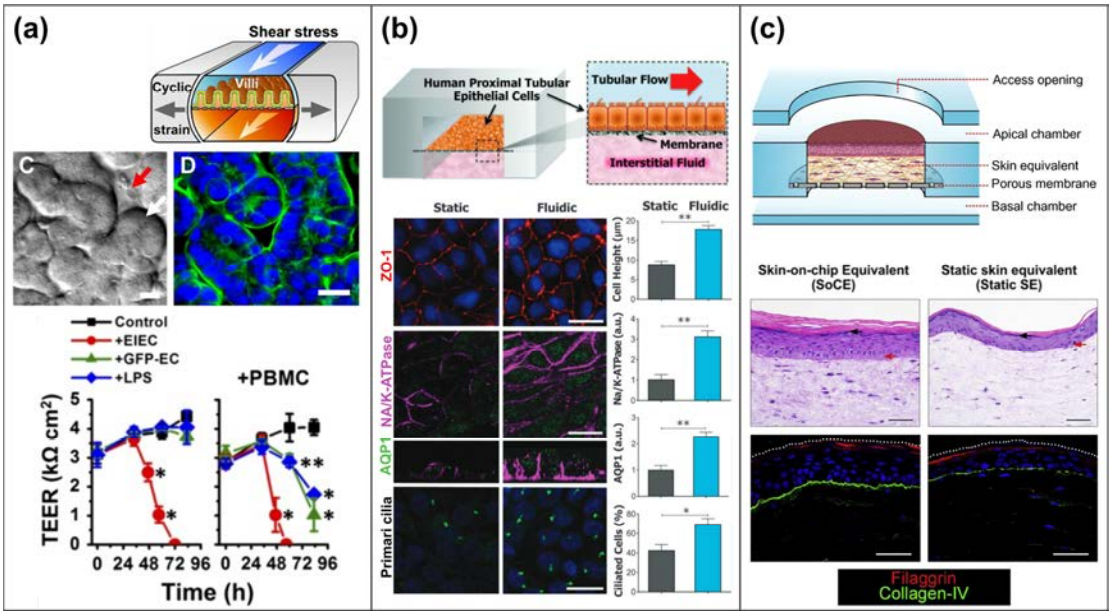

Figure 2-13 Engineered biological barrier models involving semipermeable membranes. (a) A gut-on-a-chip microfluidic device with spontaneously formation of villi resulting from mechanical cues.[113] TEER profile shows intestinal barrier injury in the presence of pathogenic bacteria (EIEP) or immune cells plus either non-pathogenic bacteria (GFP-EC) or lipopolysaccharide (LPS) endotoxin. (b) A human kidney proximal tubule-on-a-chip. Immunofluorescence images and bar plots shows increased cell height and increased expression of the tight junction protein ZO-1, aquaporin 1 (AQP1; green), Na/K-ATPase (magenta), and primary cilia in epithelial cells under flow conditions. Adapted from [115] with permission from The Royal Society of Chemistry. (c) Microfluidic platform for the development of human skin equivalents. Histological and immunofluorescence images reveal an improved epidermal morphogenesis and dermoepidermal junction when the tissue is maintained in a dynamic air-liquid interface [116].

together with alveolar epithelial cells in a superimposed compartment filled with air. The authors managed to cyclically stretch the tissue using a vacuum system at the sides of the compartments thus mimicking the breathing motion of the lung. This system was able to reproduce the effects of a pulmonary oedema by administrating a cytokine (interleukin-2) in the microvascular side concurrent with the cyclic mechanical strain [111]. The same device was also used to create a human intestinal model using the colorectal adenocarcinoma cell line (Caco-2). Interestingly, the application of mechanical cues—fluid flow and mechanical deformation as in gut peristalsis—spontaneously undergoes the formation of villi and crypts, including differentiation of Caco-2 cells into four different cell types [112]. In another study, it was analysed whether mechanical deformations of villi affects bacterial overgrowth and inflammation [113]. The study demonstrated that cessation of epithelial deformation triggers bacterial overgrowth, and also that immune cells and endotoxin induce villus injury and intestinal barrier breakdown because of the production of proinflammatory cytokines by epithelial cells (Figure 2-13a).

Mechanical forces due to fluid flow in blood vessels and epithelial tubules can be reproduced in microfluidic devices to mimic an *in vivo*-like environment. For instance, Jang *et al*. created a device with a microchannel lined by kidney tubular cells from the collecting duct [86]. The device consisted of a porous membrane and two PDMS channels that accommodate lumen and interstitial sides. Results demonstrated that cells subjected to fluidic flow exhibit enhanced cell polarization, cytoskeletal reorganization, and molecular transport in comparison with cells grown on glass substrate under static conditions. In addition, the device was used to investigate the role of FSS in translocation of aquaporin-2 (a vasopressin-regulated apical water channel) [114]. A model of kidney proximal tubule was also developed in that microfluidic device for nephrotoxicity assessment [115]; proximal epithelial cells were subjected to flow and exposed to the nephrotoxin cisplatin (Figure 2-13b). The tubule-on-a-chip better predicted nephrotoxicity in the human kidney compared to conventional cultures and even reproduced nephrotoxicity recovery after injection of cimetidine which has shown to suppress its toxic effects in canines. A dynamic environment was also used to promote the development of human skin equivalents. Sriram *et al.* cultured keratinocytes (cells that form the outermost layer of the skin) on a fibrin-based dermal matrix containing fibroblasts (i.e., a dermal equivalent) previously integrated into a microfluidic platform for continuous perfusion and ventilation of the tissue (Figure 2-13c) [116]. By maintaining the tissue in the dynamic air-liquid interface, the skin model exhibited improved epidermal differentiation, barrier function (i.e., lower permeability), and a more robust dermoepidermal junction compared to skin equivalents cultured in standard tissue culture inserts. Importantly, the dermoepidermal junction had a basement membrane with increased expression of proteins from the collagen and laminin families, which are essential for cells to attach to the ECM and thus prevent epidermal detachment.

Membrane-based microfluidic devices have also been designed to allocate several epithelial and endothelial cell monolayers. Wufuer *et al*. developed a 'skin-on-a-chip' model that mimics the cell layer physiology of the human skin consisting of epidermal, dermal, and endothelial layers [117]. The device was composed of three layers of silicone elastomer stacked together with two intermediate porous membranes. With the device, the authors optimized a model of skin inflammation and oedema by applying a proinflammatory cytokine (TNF-α). In addition, they also demonstrated the ability of the device as a drug testing by reversing the pathological scenario through the administration of a well-known drug (dexamethasone) to treat the induced inflammation. A cell sheet stratification technique has also been used to construct several layered tissues. This technique is based on harvesting and stratifying contiguous cell sheets on a culture insert by means of a custom-made manipulator. Using this methodology, Kim *et al*. fabricated a stacking of three cell layers mimicking a hepatic plate (i.e., hepatocytes forming layers of 1–2 cell thick) surrounded by two monolayers of sinusoidal endothelial cells [118]. This heterotypic 3D configuration contributed to the upregulation of hepatocyte-specific functions for a long period, especially the maintenance of hepatocyte phenotype which is rapidly lost in conventional homotypic *in vitro* cultures. Similar 3D cell stacking can be currently constructed by using bioprinting techniques. Horvath *et al*. created alveolar-capillary barriers *in vitro* by a sequence of prints, including an endothelial cell layer, an ECM layer, and an epithelial cell layer [106]. This methodology demonstrated high reproducibility and capability to achieve a very thin tissue barrier, comparable to the physiological thickness of the basement membrane found in native tissues (1.6 μm) which is critical for an adequate oxygen uptake.

2.5.2 | Microchannels

Microchannels that physically link two side-by-side chambers have been also used as a compartmentalization strategy [119]. In this approach, cells are cultured in one of the chambers to form a cell monolayer that completely covers the inner surfaces. With a microchannel size of a few microns, epithelial or endothelial cells lining the chamber would be unable to pass through the microchannels whereas biomolecules could diffuse through them. In addition, supporting cells in the adjacent compartment could extend cytoplasmic processes to enable a direct contact between heterotypic cells (e.g., astrocytic end-feet extended along the microchannels). This kind of microfluidic chip is commercially available from SynVivo Inc (Huntsville, AL, US). The device consists of a PDMS slab containing the fluidic microstructures bonded to a glass slide, which facilitates real-time imaging. In a work by Deosarkar *et al*., the SynVivo chip was used to develop a model of BBB by culturing rat brain capillary endothelial cells with either astrocytes or an astrocyte conditioned medium (Figure 2-14a) [120]. Both cell cultures exhibited improved barrier formation that was supported by permeability to tracers and electrical resistant measurements, in contrast to just endothelial cultures. This device

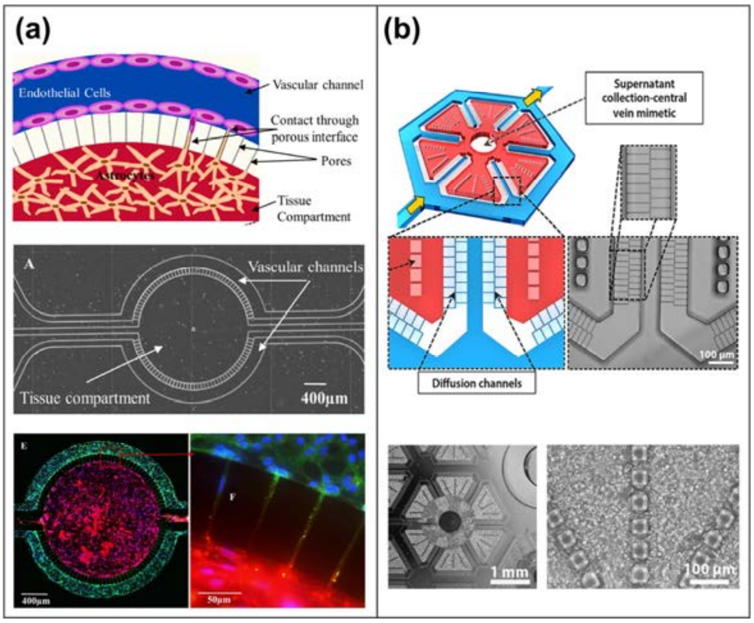

Figure 2-14 Engineered biological barrier models involving microchannels. (a) Neonatal BBB model consisted of side-by-side chambers connected through microchannels.[109] Immunofluorescence image shows direct contact communication between endothelial cells (ZO-1; green) and astrocytes (astrocytic marker GFAP; red). (b) Scalable liver-on-a-chip microdevice for long-term maintenance of hepatocyte function *in vitro*, in which microchannels artificially mimic the fenestrated endothelial cells of the liver [111].

has also been used to quantify drugs and antibodies that cross the BBB in order to find therapeutic candidates that could reach the brain [121].

Engineered microchannels have also been used as a microfluidic endothelial-like barrier. Several authors have artificially reproduced the very leaky endothelium of the liver sinusoid by the microchannels themselves (Figure 2-14f). Despite the lack of cell functionalities (i.e., no endothelial cells), a non-biological barrier can simulate some mass transport properties of blood vessels to maintain for long term the phenotype and functions of primary hepatocytes in cell cultures [122, 123].

2.5.3 | Gel-liquid interface

Gel-liquid interfaces can physically support the cells while enabling a direct contact interaction between tissues. This interface can be microfabricated by means of phaseguides structures that act as a capillary pressure barriers [124]. The function of these structures is to selectively pattern a gel in a central lane by meniscus pinning, so cells could proliferate in the interface between the gel (e.g., ECM hydrogel) and the liquid (e.g., culture medium) in adjacent lanes. This technology is commercially available by Mimetas (Leiden, NL) in a high-throughput microfluidic platform called OrganPlate. Trietsch *et al.* used it to develop up to 40 replicas in a single platform of a model of intestinal tract epithelium (Figure 2-15a) [125]. They created perfusable polarized epithelial tubes using Caco-2 cells and assessed its barrier integrity during drug-induced cell death. Alternatively, other work managed to form a temporary gel-like membrane that can be later removed after cell proliferation [126]. Therefore, a direct cell-cell contact is promoted and there is no diffusion resistance at the interface between cell types.

A hydrogel channel can also be defined using equally spaced post structures. The surface tension caused by these structures will prevent the hydrogel from entering in between the posts [127]. Wang *et al*. developed a microfluidic device able to trap primary glomerular microtissues into ECM semilunar substrates and succeed in forming glomerular filtration barriers including endothelial cells, basement membrane, and podocytes that entirely covered the ECM surface (Figure 2-15b) [128]. In particular, the microdevice was found suitable for modelling diabetic nephropathy—a chronic loss of kidney function in people with diabetes mellitus—since microtissues under high glucose conditions exhibited, in a dose-dependent manner, barrier dysfunction, increased albumin permeability, and excessive reactive oxygen species production, which are closely associated in the progression of diabetic nephropathy. To permit co-cultures and thus emulate heterotypic cell-cell interactions, cells can be added to the gel preparation before filling the channels. For instance, a neurovascular unit consisting of human microvascular endothelial cells mimicking cerebral blood vessels, primary rat neurons, and astrocytes was constructed with multiple side-by-side ECM and fluidic channels (Figure 2-15c) [129].

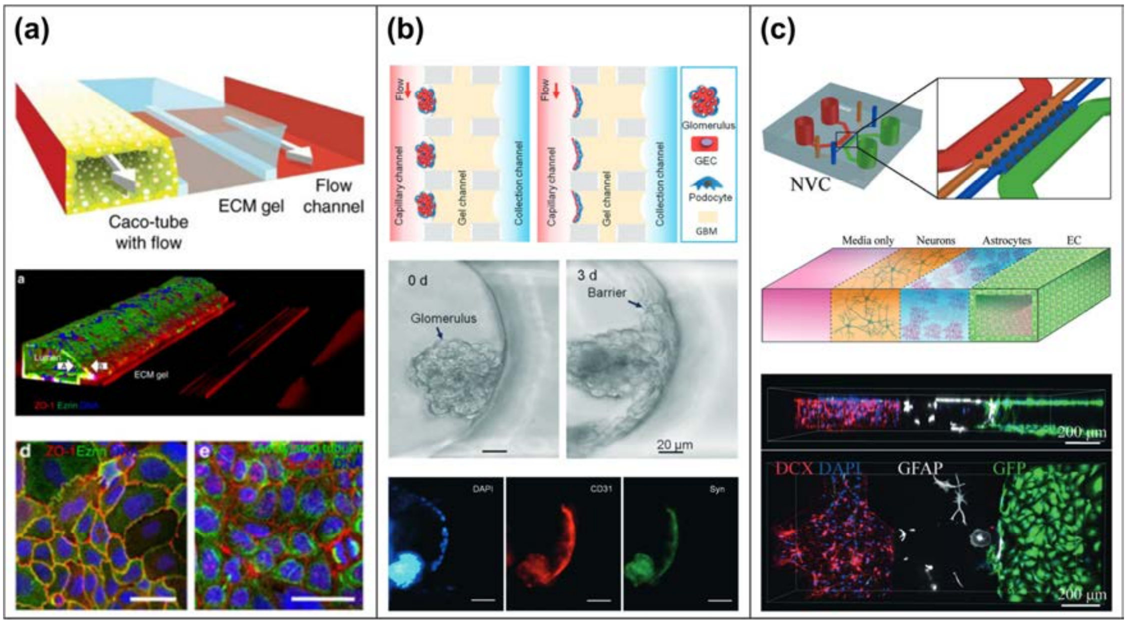

Figure 2-15 Engineered biological barrier models involving gel-liquid interface. (a) Intestinal epithelium tubule in a microfluidic channel created with a gel interface.[125] As revealed by immunofluorescence, cells form a confluent layer lining the whole channel which results in a perfusable lumen. (b) Glomerulus-on-a-chip microdevice. Glomerular microtissues are adhered to a gel surface and self-assembled into a continuous barrier of endothelial cells (CD31; red) and podocytes (synaptopodin; green) under flow perfusion. Adapted from [128] with permission from The Royal Society of Chemistry. (c) Three-dimensional neurovascular microfluidic model that enables heterotypic cell-cell interactions; it comprises human microvascular endothelial cells mimicking cerebral blood vessels, primary rat neurons, and astrocytes. Adapted from [129] with permission from The Royal Society of Chemistry.

Moreover, gel-liquid approach has enabled cell migration studies in response to specific cytokines such as tumour cell intravasation (i.e., migration towards blood vessels) under TNFα exposure [130] or tumour cell extravasation (i.e., migration from blood vessels) under chemokine CXCL5 [131]. In another work, cell migration caused by EMT was initiated in proximal tubular epithelial cells covering a basement membrane extract in a microfluidic device [132]. In response to serum proteins, cells become myofibroblasts and migrated within the gel. EMT has been proposed to be an early stage of fibrotic disorders, such as kidney interstitial fibrosis which is characterized by an excessive accumulation of ECM in the interstitial space. Since observation of EMT process is extremely difficult *in vivo*, MPS have become relevant *in vitro* tools to reproduce and follow in real time this process.

Three-dimensions characteristic features of native tissues have been reproduced in *in vitro* by structuring gel surfaces. For example, hydrogel scaffolds with an array of finger-like elements that mimic *in vivo* villi were developed to support intestinal epithelial cells [133]. For this purpose, a microfabricated alginate mould is used to create the 3D scaffold by pouring a pre-gel solution that is subsequently polymerized and detached from the mould after dissolving the alginate [134]. In that study, the expression of MUC17 (which is a transmembrane mucin responsible for the protective layer of mucus against pathogens) was higher in presence of the 3D organization than in 2D models and, interestingly, its knockdown compromised the intestinal barrier function. On the other hand, TEER measurements and tracer assays have evidenced a leaker barrier for intestinal epithelial cells cultured on 3D villi-like structures compared to Transwell inserts [133, 135], which is accounted for a decreased expression of tight junctions [136] and an increased cell culture area in the 3D model.

2.5.4 | Tubules and vessels embedded within an ECM

The latter microengineered approach consists in embedded tubules or microvascular networks into an ECM. Such epithelia and endothelia can be constructed either by creating fluidic microchannels that are later lined with cells or by forming channels of hydrogel laden with cells that results in branching microvessels. The primary advances of these approaches are the relevant 3D architecture and the capacity to perfuse the microvessels or tubules.

Homan *et al*. reported a bioprinting methodology to create 3D renal proximal tubules on demand (Figure 2-16a) [7]. They constructed a convoluted tubule by printing a sacrificial ink that was embedded within an ECM and subsequently removed. Finally, the convoluted tubular channel (~350 µm in diameter) was filled with cells, perfused with culture medium, and allowed to form a monolayer lining the channel. The 3D *in vitro* tubule, besides recreating a cyclosporine-dependent nephrotoxicity, exhibited enhanced epithelial phenotype (i.e., cell height, microvilli development, and albumin uptake) than conventional 2D cell cultures.

Similar bioprinting methodology was employed by Kolesky *et al.* to develop a perfusable vascular network contained by an ECM (Figure 2-16b) [137]. They managed to obtain a thick (>1cm) 3D fluidic network interconnecting various lattice patterns of sacrificial ink. After liquefying and evacuating the ink, channels of the network were lined with human umbilical vein endothelial cells (hUVECs) to form a vascularization system. In addition, hMSCs and fibroblasts were incorporated in the surrounding ECM as a parenchyma and connective tissue, respectively. The long-term administration of specific growth factors via the vascular network promoted the osteogenic differentiation of hMSCs *in situ*; thus being able to recapitulate heterogeneous complex tissue architectures and enabling its maturation.

Another methodology is the so-called ‘viscous finger patterning’ that can be used to create lumens with circular cross-sectional geometries. For this purpose, a droplet of culture medium is placed on the inlet of a microchannel previously loaded with pre-polymerized hydrogel solution. As a result, the culture medium flows through the centre of the microchannel displacing the hydrogel [138]. After polymerization of the hydrogel, there remains a patterned lumen that can be lined with endothelial cells to mimic a blood vessel [139]. Furthermore, endothelial cells can be combined with supporting cells by seeding them first on the luminal wall or by incorporating them in the hydrogel solution. For example, a co-culture of primary human brain microvascular

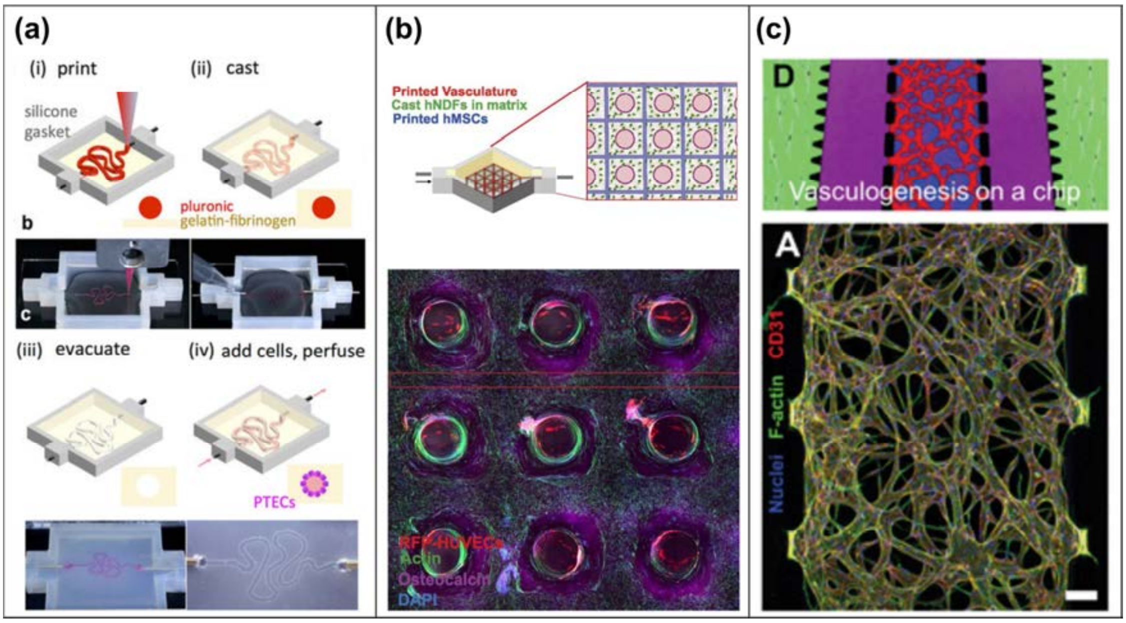

Figure 2-16 Engineered biological barrier models involving tubules and vessels embedded within an ECM. (d) Bioprinting method for creating 3D human renal proximal tubules *in vitro* that are fully embedded within an ECM, including printing of a sacrificial ink, casting of an ECM, evacuation of the ink, and cell seeding.[7] (e) Three-dimensional bioprinting of thick vascularized tissue consisted of a perfusable vascular network using hUVECs surrounded by hMSCs and fibroblasts.[137] Immunofluorescence image shows osteogenic differentiation (Osteocalcin; violet) of hMSCs *in situ* after administration of specific growth factors via the vascular network. (f) A perfusable microvascular network grown in a hydrogel channel. The obtained network exhibits relevant morphological characteristics of *in vivo* blood vessels. Adapted from [142] with permission from The Royal Society of Chemistry.

endothelial cells, pericytes, and astrocytes was developed with this technique to mimic the BBB [140]. Under inflammatory stimulation with TNF-α and compared to Transwell cultures, the vascular system showed a profile of secreted cytokines that closely mimicked those observed in the living brain.

Relatively complex vascular structures can also be engineered using soft lithography techniques instead of 3D printing. For example, a scaffold made of biodegradable elastomer was constructed by stacking several microfluidic layers [141]. In that work, the authors built a scalable vascular system containing fluidic branches that were covered with hUVECs. Combining this engineered vessel network with parenchymal cells such as rat hepatocytes or cardiomyocytes, they constructed functional vascularized liver and cardiac tissues, respectively. In particular, the latter was implanted in rat femoral vessels via direct anastomosis, which supports its applicability for regenerative medicine.

Unlike systems with defined vasculature, the development of microvessel networks within an ECM can closely mirror their *in vivo* morphology. Kim et al. demonstrated the spontaneous formation of interconnected networks of microvessels in a microfluidic device using hUVECs (Figure 2-16c) [142]. The device consisted of five side-by-side channels separated by posts, in which the central channel was filled with hydrogel. Either the hydrogel laden with the endothelial cells or the cells coating one of the sides of the hydrogel resulted in the proliferation of a long-term stable perfusable microvascular network; the *sine qua non* of this formation were growth factors secreted by supporting cells (i.e., human normal lung fibroblasts) that were co-cultured in a lateral channel. In addition, endothelial cells exposed to FSS exhibited some physiological responses (i.e., cytoskeleton reorganization and nitric oxide synthesis) of *in vivo* vessels. A very similar device was used to model choroidal neovascularization in age-related macular degeneration, wherein new blood vessels from the retinal choroid abnormally grew towards the retinal pigmented epithelium compromising the outer BRB [143]. They combined a perfusable blood vessel network embedded in an ECM with a cell monolayer of retinal epithelial cells attached to the ECM, where both tissues were separated by a gap channel. The administration of VEGF at high concentrations in the apical side of the retinal epithelium induced the proliferation of new vessels that penetrated the RPE monolayer. Otherwise, bevacizumab (a current drug for the age-related macular degeneration treatment) was found to inhibit choroidal neovascularization caused by VEGF and therefore vessel invasion. In a different approach, it was developed a platform based on a standard 96-well plate with six microfluidic units for similar purposes, including a hydrogel chamber for vasculogenesis and two microfluidic channels for continuous nutrients supply [144]. The device was found suitable for generating perfusable microvessels networks and especially for screening of drugs, as they tested the efficacy of well-known anti-angiogenic and anti-cancer drugs in a tumoral environment by co-culturing cancer cells.

2.6 | REFERENCES

[1] Tsukita S, Furuse M, Itoh M. Multifunctional strands in tight junctions. *Nat Rev Mol Cell Biol* 2001; 2: 285–293.

[2] Förster C. Tight junctions and the modulation of barrier function in disease. *Histochem Cell Biol* 2008; 130: 55–70.

[3] Zihni C, Mills C, Matter K, et al. Tight junctions: from simple barriers to multifunctional molecular gates. *Nat Rev Mol Cell Biol* 2016; 17: 564–580.

[4] Sawada N. Tight junction-related human diseases. *Pathol Int* 2013; 63: 1–12.

[5] Benam KH, Dauth S, Hassell B, et al. Engineered In Vitro Disease Models. *Annu Rev Pathol Mech Dis* 2015; 10: 195–262.

[6] Huh D, Matthews BD, Mammoto A, et al. Reconstituting Organ-Level Lung Functions on a Chip. *Science* 2010; 328: 1662–1668.

[7] Homan KA, Kolesky DB, Skylar-Scott MA, et al. Bioprinting of 3D Convoluted Renal Proximal Tubules on Perfusable Chips. *Sci Rep* 2016; 6: 34845.

[8] Yeste J, García-Ramírez M, Illa X, et al. A compartmentalized microfluidic chip with crisscross microgrooves and electrophysiological electrodes for modeling the blood–retinal barrier. *Lab Chip* 2018; 18: 95–105.

[9] Moraes C, Mehta G, Lesher-Perez SC, et al. Organs-on-a-Chip: A Focus on Compartmentalized Microdevices. *Ann Biomed Eng* 2012; 40: 1211–1227.

[10] Colegio OR, Van Itallie CM, McCrea HJ, et al. Claudins create charge-selective channels in the paracellular pathway between epithelial cells. *AJP Cell Physiol* 2002; 283: C142–C147.

[11] Yu ASL, Enck AH, Lencer WI, et al. Claudin-8 Expression in Madin-Darby Canine Kidney Cells Augments the Paracellular Barrier to Cation Permeation. *J Biol Chem* 2003; 278: 17350–17359.

[12] Terryn S, Jouret F, Vandenabeele F, et al. A primary culture of mouse proximal tubular cells, established on collagen-coated membranes. *AJP Ren Physiol* 2007; 293: F476–F485.

[13] Mehta D. Signaling Mechanisms Regulating Endothelial Permeability. *Physiol Rev* 2006; 86: 279–367.

[14] Komarova Y, Malik AB. Regulation of Endothelial Permeability via Paracellular and Transcellular Transport Pathways. *Annu Rev Physiol* 2010; 72: 463–493.

[15] Blaine J, Chonchol M, Levi M. Renal Control of Calcium, Phosphate, and Magnesium Homeostasis. *Clin J Am Soc Nephrol* 2015; 10: 1257–1272.

[16] Vandenbroucke E, Mehta D, Minshall R, et al. Regulation of Endothelial Junctional Permeability. *Ann N Y Acad Sci* 2008; 1123: 134–145.

[17] Ebnet K (ed). *Cell Polarity 1: Biological Role and Basic Mechanisms*. Cham: Springer International Publishing. Epub ahead of print 2015. DOI: 10.1007/978-3-319-14463-4.

[18] Niessen CM. Tight Junctions/Adherens Junctions: Basic Structure and Function. *J Invest Dermatol* 2007; 127: 2525–2532.

[19] Meşe G, Richard G, White TW. Gap Junctions: Basic Structure and Function. *J Invest Dermatol* 2007; 127: 2516–2524.

[20] Shin K, Fogg VC, Margolis B. Tight Junctions and Cell Polarity. *Annu Rev Cell Dev Biol* 2006; 22: 207–235.

[21] Claude P. Morphological factors influencing transepithelial permeability: A model for the resistance of the Zonula Occludens. *J Membr Biol* 1978; 39: 219–232.

[22] Hou J, Goodenough DA. Claudin-16 and claudin-19 function in the thick ascending limb: *Curr Opin Nephrol Hypertens* 2010; 19: 483–488.

[23] Angelow S, Ahlstrom R, Yu ASL. Biology of claudins. *AJP Ren Physiol* 2008; 295: F867–F876.

[24] Weber CR. Dynamic properties of the tight junction barrier. *Ann N Y Acad Sci* 2012; 1257: 77–84.

[25] Weber CR, Liang GH, Wang Y, et al. Claudin-2-dependent paracellular channels are dynamically gated. *eLife* 2015; 4: e09906.

[26] Anderson JM, Van Itallie CM. Physiology and Function of the Tight Junction. *Cold Spring Harb Perspect Biol* 2009; 1: a002584.

[27] Steed E, Balda MS, Matter K. Dynamics and functions of tight junctions. *Trends Cell Biol* 2010; 20: 142–149.

[28] Turner JR. Intestinal mucosal barrier function in health and disease. *Nat Rev Immunol* 2009; 9: 799–809.

[29] Greuter T, Shah VH. Hepatic sinusoids in liver injury, inflammation, and fibrosis: new pathophysiological insights. *J Gastroenterol* 2016; 51: 511–519.

[30] Obermeier B, Daneman R, Ransohoff RM. Development, maintenance and disruption of the blood-brain barrier. *Nat Med* 2013; 19: 1584–1596.

[31] Abbott NJ, Patabendige AAK, Dolman DEM, et al. Structure and function of the blood–brain barrier. *Neurobiol Dis* 2010; 37: 13–25.

[32] Blanchette M, Daneman R. Formation and maintenance of the BBB. *Mech Dev* 2015; 138: 8–16.

[33] Chen Y, Liu L. Modern methods for delivery of drugs across the blood–brain barrier. *Adv Drug Deliv Rev* 2012; 64: 640–665.

[34] Campbell M, Humphries P. The blood-retina barrier: tight junctions and barrier modulation. *Adv Exp Med Biol* 2012; 763: 70–84.

[35] Mouw JK, Ou G, Weaver VM. Extracellular matrix assembly: a multiscale deconstruction. *Nat Rev Mol Cell Biol* 2014; 15: 771–785.

[36] Gattazzo F, Urciuolo A, Bonaldo P. Extracellular matrix: A dynamic microenvironment for stem cell niche. *Biochim Biophys Acta BBA - Gen Subj* 2014; 1840: 2506–2519.

[37] Rozario T, DeSimone DW. The extracellular matrix in development and morphogenesis: A dynamic view. *Dev Biol* 2010; 341: 126–140.

[38] Yeaman C, Grindstaff KK, Nelson WJ. New perspectives on mechanisms involved in generating epithelial cell polarity. *Physiol Rev* 1999; 79: 73–98.

[39] Kim KK, Kugler MC, Wolters PJ, et al. Alveolar epithelial cell mesenchymal transition develops in vivo during pulmonary fibrosis and is regulated by the extracellular matrix. *Proc Natl Acad Sci* 2006; 103: 13180–13185.

[40] Abbott NJ, Rönnbäck L, Hansson E. Astrocyte–endothelial interactions at the blood–brain barrier. *Nat Rev Neurosci* 2006; 7: 41–53.

[41] Daneman R, Zhou L, Kebede AA, et al. Pericytes are required for blood–brain barrier integrity during embryogenesis. *Nature* 2010; 468: 562–566.

[42] Armulik A, Genové G, Mäe M, et al. Pericytes regulate the blood–brain barrier. *Nature* 2010; 468: 557–561.

[43] Thomsen LB, Burkhart A, Moos T. A Triple Culture Model of the Blood-Brain Barrier Using Porcine Brain Endothelial cells, Astrocytes and Pericytes. *PLOS ONE* 2015; 10: e0134765.

[44] March S, Hui EE, Underhill GH, et al. Microenvironmental regulation of the sinusoidal endothelial cell phenotype in vitro. *Hepatology* 2009; 50: 920–928.

[45] Luissint A-C, Parkos CA, Nusrat A. Inflammation and the Intestinal Barrier: Leukocyte–Epithelial Cell Interactions, Cell Junction Remodeling, and Mucosal Repair. *Gastroenterology* 2016; 151: 616–632.

[46] Bruewer M, Luegering A, Kucharzik T, et al. Proinflammatory Cytokines Disrupt Epithelial Barrier Function by Apoptosis-Independent Mechanisms. *J Immunol* 2003; 171: 6164–6172.

[47] Coyne CB. Regulation of Airway Tight Junctions by Proinflammatory Cytokines. *Mol Biol Cell* 2002; 13: 3218–3234.

[48] Coelho-Santos V, Leitão RA, Cardoso FL, et al. The TNF-α/Nf-κB Signaling Pathway has a Key Role in Methamphetamine–Induced Blood–Brain Barrier Dysfunction. *J Cereb Blood Flow Metab* 2015; 35: 1260–1271.

[49] de Vries HE, Blom-Roosemalen MCM, Oosten M van, et al. The influence of cytokines on the integrity of the blood-brain barrier in vitro. *J Neuroimmunol* 1996; 64: 37–43.

[50] Honda M, Nakagawa S, Hayashi K, et al. Adrenomedullin Improves the Blood–Brain Barrier Function Through the Expression of Claudin-5. *Cell Mol Neurobiol* 2006; 26: 109–118.

[51] Förster C, Burek M, Romero IA, et al. Differential effects of hydrocortisone and TNFα on tight junction proteins in an *in vitro* model of the human blood-brain barrier: Hydrocortisone and BBB properties in brain endothelial cell line. *J Physiol* 2008; 586: 1937–1949.

[52] Geiger B, Spatz JP, Bershadsky AD. Environmental sensing through focal adhesions. *Nat Rev Mol Cell Biol* 2009; 10: 21–33.

[53] Bordeleau F, Mason BN, Lollis EM, et al. Matrix stiffening promotes a tumor vasculature phenotype. *Proc Natl Acad Sci* 2017; 114: 492–497.

[54] Janson IA, Putnam AJ. Extracellular matrix elasticity and topography: Material-based cues that affect cell function via conserved mechanisms. *J Biomed Mater Res A* 2015; 103: 1246–1258.

[55] Higuchi A, Ling Q-D, Chang Y, et al. Physical Cues of Biomaterials Guide Stem Cell Differentiation Fate. *Chem Rev* 2013; 113: 3297–3328.

[56] Li Y-SJ, Haga JH, Chien S. Molecular basis of the effects of shear stress on vascular endothelial cells. *J Biomech* 2005; 38: 1949–1971.

[57] Davies PF. Hemodynamic shear stress and the endothelium in cardiovascular pathophysiology. *Nat Clin Pract Cardiovasc Med* 2009; 6: 16–26.

[58] Tarbell JM. Shear stress and the endothelial transport barrier. *Cardiovasc Res* 2010; 87: 320–330.

[59] Weinbaum S, Duan Y, Satlin LM, et al. Mechanotransduction in the renal tubule. *Am J Physiol-Ren Physiol* 2010; 299: F1220–F1236.

[60] Larsen EH. Hans Henriksen Ussing. 30 December 1911 -- 22 December 2000. *Biogr Mem Fellows R Soc* 2009; 55: 305–335.

[61] Ussing HH, Zerahn K. Active Transport of Sodium as the Source of Electric Current in the Short-circuited Isolated Frog Skin. *Acta Physiol Scand* 1951; 23: 110–127.

[62] Koefoed-Johnsen V, Ussing HH. The Nature of the Frog Skin Potential. *Acta Physiol Scand* 1958; 42: 298–308.

[63] Johnsen VK, Levi H, Ussing HH. The Mode of Passage of Chloride Ions through the Isolated Frog Skin. *Acta Physiol Scand* 1952; 25: 150–163.

[64] Vidyasagar S, MacGregor G. Ussing Chamber Technique to Measure Intestinal Epithelial Permeability. In: Ivanov AI (ed) *Gastrointestinal Physiology and Diseases*. New York, NY: Humana Press, pp. 49–61.

[65] Bentley PJ. Amiloride: a potent inhibitor of sodium transport across the toad bladder. *J Physiol* 1968; 195: 317–330.

[66] Misfeldt DS, Hamamoto ST, Pitelka DR. Transepithelial transport in cell culture. *Proc Natl Acad Sci U S A* 1976; 73: 1212–1216.

[67] Grobstein C. Morphogenetic Interaction between Embryonic Mouse Tissues separated by a Membrane Filter. *Nature* 1953; 172: 869–871.

[68] Fang X, Neyrinck AP, Matthay MA, et al. Allogeneic Human Mesenchymal Stem Cells Restore Epithelial Protein Permeability in Cultured Human Alveolar Type II Cells by Secretion of Angiopoietin-1. *J Biol Chem* 2010; 285: 26211–26222.

[69] Hatherell K, Couraud P-O, Romero IA, et al. Development of a three-dimensional, all-human in vitro model of the blood–brain barrier using mono-, co-, and tri-cultivation Transwell models. *J Neurosci Methods* 2011; 199: 223–229.

[70] Liu D, Lin B, Shao W, et al. In Vitro and in Vivo Studies on the Transport of PEGylated Silica Nanoparticles across the Blood–Brain Barrier. *ACS Appl Mater Interfaces* 2014; 6: 2131–2136.

[71] Leonard F, Collnot E-M, Lehr C-M. A Three-Dimensional Coculture of Enterocytes, Monocytes and Dendritic Cells To Model Inflamed Intestinal Mucosa in Vitro. *Mol Pharm* 2010; 7: 2103–2119.

[72] Antunes F, Andrade F, Araújo F, et al. Establishment of a triple co-culture in vitro cell models to study intestinal absorption of peptide drugs. *Eur J Pharm Biopharm* 2013; 83: 427–435.

[73] Corcione A. Human mesenchymal stem cells modulate B-cell functions. *Blood* 2006; 107: 367–372.

[74] Gupta D, Treon SP, Shima Y, et al. Adherence of multiple myeloma cells to bone marrow stromal cells upregulates vascular endothelial growth factor secretion: therapeutic applications. *Leukemia* 2001; 15: 1950–1961.

[75] Loibl M, Binder A, Herrmann M, et al. Direct Cell-Cell Contact between Mesenchymal Stem Cells and Endothelial Progenitor Cells Induces a Pericyte-Like Phenotype In Vitro. *BioMed Res Int* 2014; 2014: 1–10.

[76] Yeste J, Illa X, Gutiérrez C, et al. Geometric correction factor for transepithelial electrical resistance measurements in transwell and microfluidic cell cultures. *J Phys Appl Phys* 2016; 49: 375401.

[77] Karp PH, Moninger TO, Weber SP, et al. An In Vitro Model of Differentiated Human Airway Epithelia: Methods for Establishing Primary Cultures. In: *Epithelial Cell Culture Protocols*. New Jersey: Humana Press, pp. 115–137.

[78] Duff T, Carter S, Feldman G, et al. Transepithelial resistance and inulin permeability as endpoints in in vitro nephrotoxicity testing. *Altern Lab Anim ATLA* 2002; 30 Suppl 2: 53–59.

[79] Jovov B, Wills NK, Lewis SA. A spectroscopic method for assessing confluence of epithelial cell cultures. *Am J Physiol* 1991; 261: C1196-1203.

[80] Giaever I, Keese CR. Use of Electric Fields to Monitor the Dynamical Aspect of Cell Behavior in Tissue Culture. *IEEE Trans Biomed Eng* 1986; BME-33: 242–247.

[81] Szulcek R, Bogaard HJ, van Nieuw Amerongen GP. Electric Cell-substrate Impedance Sensing for the Quantification of Endothelial Proliferation, Barrier Function, and Motility. *J Vis Exp* 2014; e51300.

[82] Pronk MCA, van Bezu JSM, van Nieuw Amerongen GP, et al. RhoA, RhoB and RhoC differentially regulate endothelial barrier function. *Small GTPases* 2017; 0: 1–19.

[83] Wegener J, Keese CR, Giaever I. Electric Cell–Substrate Impedance Sensing (ECIS) as a Noninvasive Means to Monitor the Kinetics of Cell Spreading to Artificial Surfaces. *Exp Cell Res* 2000; 259: 158–166.

[84] Müller J, Thirion C, Pfaffl MW. Electric cell-substrate impedance sensing (ECIS) based real-time measurement of titer dependent cytotoxicity induced by adenoviral vectors in an IPI-2I cell culture model. *Biosens Bioelectron* 2011; 26: 2000–2005.

[85] Gamal W, Borooah S, Smith S, et al. Real-time quantitative monitoring of hiPSC-based model of macular degeneration on Electric Cell-substrate Impedance Sensing microelectrodes. *Biosens Bioelectron* 2015; 71: 445–455.

[86] Jang K-J, Suh K-Y. A multi-layer microfluidic device for efficient culture and analysis of renal tubular cells. *Lab Chip* 2010; 10: 36–42.

[87] Franssila S. *Introduction to Microfabrication*. 2nd ed. Chichester, UK: John Wiley & Sons, 2010.

[88] Qin D, Xia Y, Whitesides GM. Soft lithography for micro- and nanoscale patterning. *Nat Protoc* 2010; 5: 491–502.

[89] Du Y, Li N, Yang H, et al. Mimicking liver sinusoidal structures and functions using a 3D-configured microfluidic chip. *Lab Chip* 2017; 17: 782–794.

[90] Prodanov L, Jindal R, Bale SS, et al. Long-term maintenance of a microfluidic 3D human liver sinusoid: Maintenance of a Microfluidic 3D Human Liver Sinusoid. *Biotechnol Bioeng* 2016; 113: 241–246.

[91] Kang YBA, Sodunke TR, Lamontagne J, et al. Liver sinusoid on a chip: Long-term layered co-culture of primary rat hepatocytes and endothelial cells in microfluidic platforms: Liver Sinusoid on a Chip. *Biotechnol Bioeng* 2015; 112: 2571–2582.

[92] Lee PJ, Hung PJ, Lee LP. An artificial liver sinusoid with a microfluidic endothelial-like barrier for primary hepatocyte culture. *Biotechnol Bioeng* 2007; 97: 1340–1346.

[93] O'Neill PF, Ben Azouz A, Vázquez M, et al. Advances in three-dimensional rapid prototyping of microfluidic devices for biological applications. *Biomicrofluidics* 2014; 8: 052112.

[94] Guckenberger DJ, de Groot TE, Wan AMD, et al. Micromilling: a method for ultra-rapid prototyping of plastic microfluidic devices. *Lab Chip* 2015; 15: 2364–2378.

[95] Khan Malek CG. Laser processing for bio-microfluidics applications (part I). *Anal Bioanal Chem* 2006; 385: 1351–1361.

[96] Khan Malek CG. Laser processing for bio-microfluidics applications (part II). *Anal Bioanal Chem* 2006; 385: 1362–1369.

[97] Au AK, Lee W, Folch A. Mail-order microfluidics: evaluation of stereolithography for the production of microfluidic devices. *Lab Chip* 2014; 14: 1294–1301.

[98] Ho CMB, Ng SH, Li KHH, et al. 3D printed microfluidics for biological applications. *Lab Chip* 2015; 15: 3627–3637.

[99] Murphy SV, Atala A. 3D bioprinting of tissues and organs. *Nat Biotechnol* 2014; 32: 773–785.

[100] Guillotin B, Souquet A, Catros S, et al. Laser assisted bioprinting of engineered tissue with high cell density and microscale organization. *Biomaterials* 2010; 31: 7250–7256.

[101] Cereijido M. Polarized monolayers formed by epithelial cells on a permeable and translucent support. *J Cell Biol* 1978; 77: 853–880.

[102] Misfeldt DS, Hamamoto ST, Pitelka DR. Transepithelial transport in cell culture. *Proc Natl Acad Sci* 1976; 73: 1212–1216.

[103] Barrile R, van der Meer AD, Park H, et al. Organ-on-Chip Recapitulates Thrombosis Induced by an anti-CD154 Monoclonal Antibody: Translational Potential of Advanced Microengineered Systems. *Clin Pharmacol Ther* 2018; In press.

[104] Kilic O, Pamies D, Lavell E, et al. Brain-on-a-chip model enables analysis of human neuronal differentiation and chemotaxis. *Lab Chip* 2016; 16: 4152–4162.

[105] Booth R, Kim H. Characterization of a microfluidic in vitro model of the blood-brain barrier (μBBB). *Lab Chip* 2012; 12: 1784–1792.

[106] Horváth L, Umehara Y, Jud C, et al. Engineering an in vitro air-blood barrier by 3D bioprinting. *Sci Rep* 2015; 5: 7974.

[107] Illa X, Vila S, Yeste J, et al. A Novel Modular Bioreactor to In Vitro Study the Hepatic Sinusoid. *PLoS ONE* 2014; 9: e111864.

[108] Yeste J, Martínez-Gimeno L, Illa X, et al. A perfusion chamber for monitoring transepithelial NaCl transport in an in vitro model of the renal tubule. *Biotechnol Bioeng* 2018; 115: 1604–1613.

[109] Blundell C, Tess ER, Schanzer ASR, et al. A microphysiological model of the human placental barrier. *Lab Chip* 2016; 16: 3065–3073.

[110] Blundell C, Yi Y-S, Ma L, et al. Placental Drug Transport-on-a-Chip: A Microengineered In Vitro Model of Transporter-Mediated Drug Efflux in the Human Placental Barrier. *Adv Healthc Mater* 2018; 7: 1700786.

[111] Huh D, Leslie DC, Matthews BD, et al. A Human Disease Model of Drug Toxicity-Induced Pulmonary Edema in a Lung-on-a-Chip Microdevice. *Sci Transl Med* 2012; 4: 159ra147-159ra147.

[112] Kim HJ, Ingber DE. Gut-on-a-Chip microenvironment induces human intestinal cells to undergo villus differentiation. *Integr Biol* 2013; 5: 1130.

[113] Kim HJ, Li H, Collins JJ, et al. Contributions of microbiome and mechanical deformation to intestinal bacterial overgrowth and inflammation in a human gut-on-a-chip. *Proc Natl Acad Sci* 2016; 113: E7–E15.

[114] Jang K-J, Cho HS, Kang DH, et al. Fluid-shear-stress-induced translocation of aquaporin-2 and reorganization of actin cytoskeleton in renal tubular epithelial cells. *Integr Biol* 2011; 3: 134–141.

[115] Jang K-J, Mehr AP, Hamilton GA, et al. Human kidney proximal tubule-on-a-chip for drug transport and nephrotoxicity assessment. *Integr Biol* 2013; 5: 1119–1129.

[116] Sriram G, Alberti M, Dancik Y, et al. Full-thickness human skin-on-chip with enhanced epidermal morphogenesis and barrier function. *Mater Today* 2017; In press.

[117] Wufuer M, Lee G, Hur W, et al. Skin-on-a-chip model simulating inflammation, edema and drug-based treatment. *Sci Rep* 2016; 6: 37471.

[118] Kim K, Utoh R, Ohashi K, et al. Fabrication of functional 3D hepatic tissues with polarized hepatocytes by stacking endothelial cell sheets *in vitro*: Functional 3-D hepatic tissues with polarized hepatocyte sheet. *J Tissue Eng Regen Med* 2017; 11: 2071–2080.

[119] Prabhakarpandian B, Shen M-C, Nichols JB, et al. SyM-BBB: a microfluidic blood brain barrier model. *Lab Chip* 2013; 13: 1093–1101.

[120] Deosarkar SP, Prabhakarpandian B, Wang B, et al. A Novel Dynamic Neonatal Blood-Brain Barrier on a Chip. *PLOS ONE* 2015; 10: e0142725.

[121] Terrell-Hall TB, Nounou MI, El-Amrawy F, et al. Trastuzumab distribution in an *in-vivo* and *in-vitro* model of brain metastases of breast cancer. *Oncotarget* 2017; 8: 83734–83744.

[122] Banaeiyan AA, Theobald J, Paukštyte J, et al. Design and fabrication of a scalable liver-lobule-on-a-chip microphysiological platform. *Biofabrication* 2017; 9: 015014.

[123] Lee PJ, Hung PJ, Lee LP. An artificial liver sinusoid with a microfluidic endothelial-like barrier for primary hepatocyte culture. *Biotechnol Bioeng* 2007; 97: 1340–1346.

[124] Vulto P, Podszun S, Meyer P, et al. Phaseguides: a paradigm shift in microfluidic priming and emptying. *Lab Chip* 2011; 11: 1596–1602.

[125] Trietsch SJ, Naumovska E, Kurek D, et al. Membrane-free culture and real-time barrier integrity assessment of perfused intestinal epithelium tubes. *Nat Commun* 2017; 8: 262.

[126] Tibbe MP, Leferink AM, van den Berg A, et al. Microfluidic Gel Patterning Method by Use of a Temporary Membrane for Organ-On-Chip Applications. *Adv Mater Technol* 2018; 3: 1700200.

[127] Shin Y, Han S, Jeon JS, et al. Microfluidic assay for simultaneous culture of multiple cell types on surfaces or within hydrogels. *Nat Protoc* 2012; 7: 1247–1259.

[128] Wang L, Tao T, Su W, et al. A disease model of diabetic nephropathy in a glomerulus-on-a-chip microdevice. *Lab Chip* 2017; 17: 1749–1760.

[129] Adriani G, Ma D, Pavesi A, et al. A 3D neurovascular microfluidic model consisting of neurons, astrocytes and cerebral endothelial cells as a blood–brain barrier. *Lab Chip* 2017; 17: 448–459.

[130] Zervantonakis IK, Hughes-Alford SK, Charest JL, et al. Three-dimensional microfluidic model for tumor cell intravasation and endothelial barrier function. *Proc Natl Acad Sci* 2012; 109: 13515–13520.

[131] Bersini S, Jeon JS, Dubini G, et al. A microfluidic 3D in vitro model for specificity of breast cancer metastasis to bone. *Biomaterials* 2014; 35: 2454–2461.

[132] Zhou M, Ma H, Lin H, et al. Induction of epithelial-to-mesenchymal transition in proximal tubular epithelial cells on microfluidic devices. *Biomaterials* 2014; 35: 1390–1401.

[133] Kim SH, Chi M, Yi B, et al. Three-dimensional intestinal villi epithelium enhances protection of human intestinal cells from bacterial infection by inducing mucin expression. *Integr Biol* 2014; 6: 1122–1131.

[134] Sung JH, Yu J, Luo D, et al. Microscale 3-D hydrogel scaffold for biomimetic gastrointestinal (GI) tract model. *Lab Chip* 2011; 11: 389–392.

[135] Costello CM, Hongpeng J, Shaffiey S, et al. Synthetic small intestinal scaffolds for improved studies of intestinal differentiation: Synthetic Small Intestinal Scaffolds for Improved. *Biotechnol Bioeng* 2014; 111: 1222–1232.

[136] Li N, Wang D, Sui Z, et al. Development of an Improved Three-Dimensional *In Vitro* Intestinal Mucosa Model for Drug Absorption Evaluation. *Tissue Eng Part C Methods* 2013; 19: 708–719.

[137] Kolesky DB, Homan KA, Skylar-Scott MA, et al. Three-dimensional bioprinting of thick vascularized tissues. *Proc Natl Acad Sci* 2016; 113: 3179–3184.

[138] Bischel LL, Lee S-H, Beebe DJ. A Practical Method for Patterning Lumens through ECM Hydrogels via Viscous Finger Patterning. *J Lab Autom* 2012; 17: 96–103.

[139] Bischel LL, Young EWK, Mader BR, et al. Tubeless microfluidic angiogenesis assay with three-dimensional endothelial-lined microvessels. *Biomaterials* 2013; 34: 1471–1477.

[140] Herland A, van der Meer AD, FitzGerald EA, et al. Distinct Contributions of Astrocytes and Pericytes to Neuroinflammation Identified in a 3D Human Blood-Brain Barrier on a Chip. *PLOS ONE* 2016; 11: e0150360.

[141] Zhang B, Montgomery M, Chamberlain MD, et al. Biodegradable scaffold with built-in vasculature for organ-on-a-chip engineering and direct surgical anastomosis. *Nat Mater* 2016; 15: 669–678.

[142] Kim S, Lee H, Chung M, et al. Engineering of functional, perfusable 3D microvascular networks on a chip. *Lab Chip* 2013; 13: 1489–1500.

[143] Chung M, Lee S, Lee BJ, et al. Wet-AMD on a Chip: Modeling Outer Blood-Retinal Barrier In Vitro. *Adv Healthc Mater* 2017; 7: 1700028.

[144] Phan DTT, Wang X, Craver BM, et al. A vascularized and perfused organ-on-a-chip platform for large-scale drug screening applications. *Lab Chip* 2017; 17: 511–520.

3

Transepithelial electrical resistance measurements in Transwell and microfluidic cell cultures

TEER measurements are regularly used in *in vitro* models to quantitatively evaluate the cell barrier function. Although it would be expected that TEER values obtained with the same cell type and experimental setup were comparable, values reported in the literature show a large dispersion for unclear reasons. This work highlights a possible error in a widely used formula to calculate the TEER, in which it may be erroneously assumed that the entire cell culture area contributes equally to the measurement. In this study, we have numerically calculated this error in some cell cultures previously reported. In particular, it is evidenced that some TEER measurements resulted in errors when measuring low TEERs, especially when using Transwell inserts 12 mm in diameter or microfluidic systems that have small chamber heights. To correct this error, it is proposed the use of a geometric correction factor (GCF) for calculating the TEER. In addition, a simple method to determine the GCF of a particular measurement system is described, so that it can be applied retrospectively. Finally, it is proposed and experimentally validated an interdigitated electrodes (IDE) configuration where the entire cell culture area contributes equally to the measurement, and it also implements minimal electrode coverage so that the cells can be visualised alongside TEER analysis.

Most of the contents of this chapter have been published in:

[1] **Yeste J**, Illa X, Guimerà A, Villa R. A novel strategy to monitor microfluidic in-vitro blood-brain barrier models using impedance spectroscopy. In: van den Driesche S (ed). Bellingham, WA: SPIE, p. 95180N.

[2] **Yeste J**, Illa X, Gutiérrez C, Solé M, Guimerà A, Villa R. Geometric correction factor for transepithelial electrical resistance measurements in transwell and microfluidic cell cultures. *J Phys Appl Phys* 2016; 49: 375401.

3.1 | INTRODUCTION

Most current *in vitro* barrier models are based on Transwell inserts [1–4] and microfluidic cell cultures [5–11]. TEER measurements have been consistently used in *in vitro* systems [2–4, 12–16] to evaluate the cell barrier function, which is essential to quantify the barrier function and to ensure model integrity during experiments. It would be expected that the TEER values obtained with the same cell type and experimental setup be comparable. However, there are discrepancies between TEER values reported in the literature [17]. Therefore, it is important to assess current measurement methods to clarify whether errors in the measurement could account for the differences between TEER values.

The electrode configurations broadly used to measure TEER are bipolar (two-electrodes) and tetrapolar (four-electrodes) [18, 19] configurations. Bipolar electrode systems are commonly used [20, 21] because they can be easily integrated into *in vitro* models, but have the disadvantage of being influenced by the electrode polarization impedance at the electrode-electrolyte interface. Tetrapolar electrode systems overcome this limitation. In these systems, the current is injected through a pair of electrodes (current carrying electrodes) while another pair of electrodes (pick-up electrodes) measures the voltage drop. Nevertheless, special care has to be taken when designing tetrapolar systems because they are more vulnerable to error than bipolar systems [22]. Moreover, small electrodes and channels in microfluidic systems imply an increase of the electrode polarization impedance, and a non-uniform electrical current distribution caused by the high electrical resistance along the microchannels.

To compare data from different studies, TEER is usually calculated by multiplying the measured resistance by the total cell culture area, resulting in a value independent of the area. This work highlights a possible error in the application of this formula, in which it may be erroneously assumed that the entire area contributes equally to the measurement as illustrated in Figure 3-1. Instead of using the total cell culture area, it is suggested to use an area that is weighted by the region contributing most to the measurement [16, 23]. The contribution of each region to the measurement depends highly on the current distribution. Since the current distribution is influenced by the electrode configuration, the geometry of the cell culture, and even the TEER, the values reported in the literature may be scattered owing to many different measurement

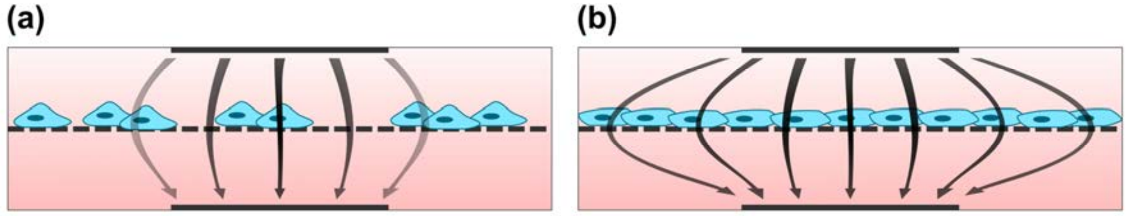

Figure 3-1 Illustration of the electrical current distribution (arrows) across (a) leaky and (b) tight barriers when measuring the TEER.

systems in use, especially for microfluidic cell cultures. Here, a GCF for calculating the TEER is proposed as a method to correct this issue.

This chapter presents a numerical and an experimental study of different tetrapolar electrode configurations that are currently being used for TEER measurements in Transwell and microfluidic cell cultures. The study compares chopstick electrodes [24–27] (the gold standard for measuring TEER in Transwell cultures), two electrode configurations integrated in microfluidic systems based on previously reported literature [5, 6, 9], and an electrode configuration here proposed based on IDE. In particular, the finite element method (FEM) is used to study the sensitivity distribution along the cell culture area and the GCF that should be used instead of the total cell culture area to calculate the TEER.

Herein, it is shown that some TEER measurements performed with the Transwell culture inserts, 12 mm in diameter, or the microfluidic systems that have small chamber heights lead to errors when measuring low TEERs if no GCF is used. Hence, part of the reported dispersion of TEER values could be attributed to a calculation error.

Finally, the proposed IDE configuration where the entire cell culture area contributes equally to the measurement was experimentally validated to perform TEER measurements. For this purpose, a custom-made bioreactor with integrated electrodes was built, and a monolayer of human cerebral microvascular endothelial cells was measured. Importantly, this system based on IDE configuration implemented minimal electrode coverage so that the cells can be visualised alongside TEER analysis.

3.2 | MATERIALS AND METHODS

3.2.1 | Simulation model

The electrical current distribution for the different electrode configurations were analysed using FEM models developed with a commercial software package (COMSOL Multiphysics version 5.0 and its AC/DC module). Two different simulation models were developed: (1) the Transwell model (Figure 3-2b) with a tetrahedral mesh of $\sim800\cdot10^3$ elements, and (2) the microfluidic model (Figure 3-2a) with a triangular mesh of $\sim17\cdot10^3$ elements. In both models, a constant DC current of 1 A was injected through the current carrying electrodes, while pick-up electrodes were set as floating potential and zero current. The rest of the outer boundaries were defined as electrical insulations.

In detail, the Transwell model (model A) is a 3D representation of a conventional cell culture insert with chopstick electrodes. A cross-sectional schematic is shown in Figure 3-3a. The model was created for 6.5 and 12 mm diameter inserts. These diameters are recommended for normalizing TEER measurements performed with chopstick electrodes, and are widely used [28–34].

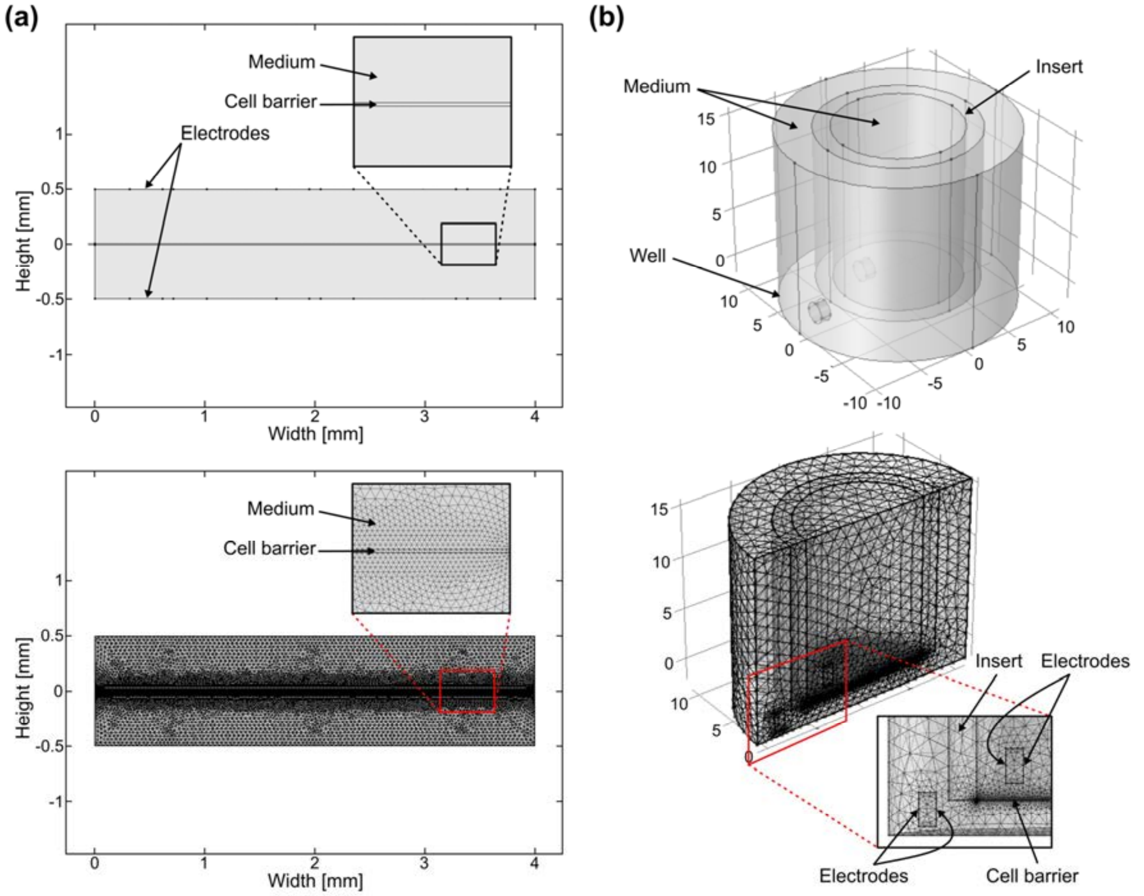

Figure 3-2 Geometric model and mesh of (a) the microfluidic system and (b) the Transwell system (insert of 12 mm in diameter). The Transwell and microfluidic models were solved for ~$800 \cdot 10^3$ elements with ~$3.2 \cdot 10^6$ degrees of freedom and ~$17 \cdot 10^3$ elements with ~$70 \cdot 10^3$ degrees of freedom, respectively. Assuming the same current distribution along the depth axis in the microfluidic model, the final solution can be achieved by multiplying the obtained current by the chamber depth.

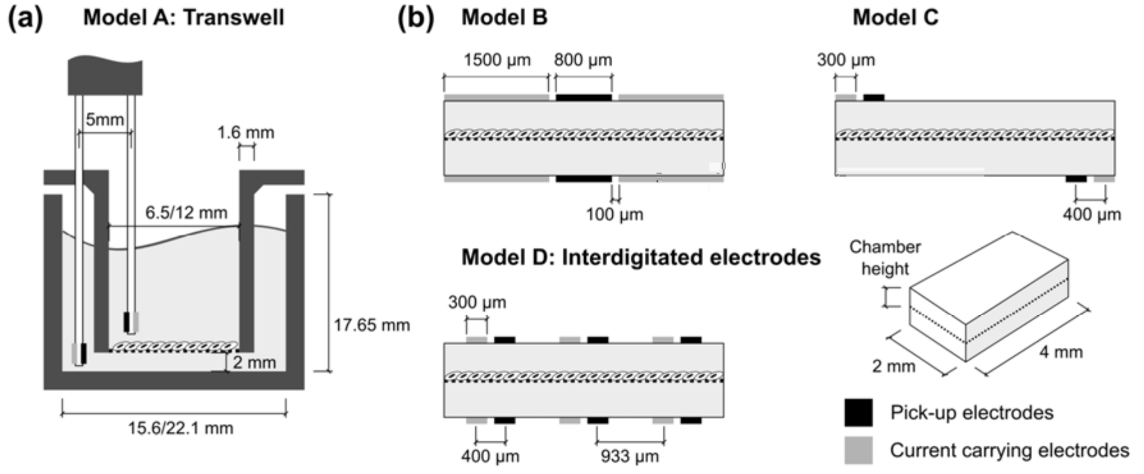

Figure 3-3 Geometrical dimensions for (a) the simulated Transwell model (6.5 and 12 mm diameter inserts), and (b) the microfluidic model with electrode configurations reported in the literature (model B–C) and the one here proposed (model D). Chamber height ranges from 100 to 500 µm. Note that figure is not drawn to scale.

The microfluidic model (model B–D) is a 2D vertical cross-section of a microfluidic cell culture. Schemes of the different electrode configurations are shown in Figure 3-3b. The model comprises two superimposed microfluidic chambers, TEER measurement electrodes placed in upper and lower surfaces of the top and bottom chamber, respectively, and a small volume that represents a cell layer in the middle of the two chambers. Cell barriers with different TEER values were simulated by changing the conductivity of this volume.

Three different electrode configurations using the microfluidic model were simulated:

1. Model B is inspired in the work by Booth *et al* [5]. It comprises small pick-up electrodes placed in the middle of the chambers and surrounded by large current carrying electrodes that cover 75 % of the cell culture area.
2. Model C has one pair of current carrying and pick-up electrodes at the surfaces of both chambers but in opposite sides. Despite the fact that the electrodes are planar and placed on the chamber surface, results are similar to those expected for models where wire electrodes are located at specific positions of the chamber [9, 35].
3. Model D, which is presented here, has IDE to improve the uniformity of the current distribution while reducing the space occupied by the electrodes; hence allowing microscopic visualisation of the cell culture. In particular, pairs of fingers (including a pick-up and a current carrying electrode) are placed facing each other and distributed equally along the top and bottom surfaces of the top and bottom chambers, respectively.

A porous membrane that supports the cells restricts the medium path to small pores and adds a resistance in series with the cell barrier. Membranes are commercially available in a broad range of pore sizes and densities. For instance, a porous membrane of 10 µm in thickness and 0.4 µm of pore size will be equivalent to a resistance of $0.5\ \Omega\ \mathrm{cm}^2$ and $12\ \Omega\ \mathrm{cm}^2$ for pore densities of 10^8 and $4\cdot10^6$ pores cm^{-2}, respectively. Since TEER and transport studies require high pore density membranes to allow maximum diffusion and the resistance of these membranes are much lower than the measured resistance, the influence of the resistance of a porous membrane is neglected in this study.

Note that the herein presented results are obtained for a given model and geometry (Figure 3-3), therefore, it is expected that results slightly differ for other conditions, such as different dimensions or low pore density membranes. Moreover, an electrical capacitance (equivalent to a flat platinum electrode ~0.2 F m^{-2} [36]) between electrode and electrolyte was used in preliminary studies to simulate the electrode polarization impedance. As this electrical capacitance had little effect in the current distribution, electrode polarization impedance has not been taken into account in the results presented here. It is also noteworthy that the simulated model only considers the volume of the two chambers as the electrical current density is confined to the volume between the electrodes (i.e., volume of the upper and lower chambers); thus, the rest of the microfluidic system (i.e., inlet and outlet tubes) hardly affect the measurement. Details on the simulation parameters are provided in the following table:

Table 3-1 Summary of the parameters used in the simulation study.

	Symbol	Value
Medium electrical conductivity	σ_m	1.5 [S m^{-1}]
Medium relative permittivity	ε_m	78
Cell barrier height	h	10 [µm]
Cell barrier area	A	8 [mm^2]
Cell barrier conductivity	σ	$\frac{h}{\mathrm{TEER_t} \cdot A}$ [S m^{-1}]

3.2.2 | Sensitivity evaluation

When measuring the TEER of a cell barrier, not all the zones contribute equally to the measured impedance. Intuitively, the volumes close to the electrodes contribute more than the volumes that are far away from them. The sensitivity s of each zone can be calculated as reported by Grimnes and Martinsen [22]:

$$s = \frac{\boldsymbol{J}_1 \boldsymbol{J}_2}{I^2}, \tag{3-1}$$

where $\boldsymbol{J}_1$ and $\boldsymbol{J}_2$ are the current density fields when a current I is injected through the current carrying electrodes and pick-up electrodes, respectively. A higher absolute value of the sensitivity means a greater influence on the total measured impedance. When the electrical resistivity of a volume is increased, and if the sensitivity is positive, higher electrical impedance is measured. Otherwise, if sensitivity is negative, lower electrical impedance is measured.

3.2.2.1 | Geometric correction factor evaluation

In Transwell and microfluidic systems, apart from the TEER, the total measured impedance also has contributions from the medium, the porous membrane support, and in case of bipolar systems, the electrode polarization impedance. For this reason, the TEER is experimentally obtained as

$$\mathrm{TEER} = (R - R_{\mathrm{blank}})\, A, \tag{3-2}$$

where R is the total measured impedance, R_{blank} is the impedance measured without cells, and A is the total cell culture area used to normalize the TEER value.

In this study, the error of the TEER measurement without GCF is calculated as the difference between the TEER obtained from simulation according to equation (3-2) ($\mathrm{TEER_s}$), and the theoretical TEER ($\mathrm{TEER_t}$) used as a parameter for the electrical conductivity of the small volume in the middle of the two chambers which represents a cell layer (i.e., the parameter σ in Table 3-1):

$$\mathrm{error} = \frac{\mathrm{TEER_s} - \mathrm{TEER_t}}{\mathrm{TEER_t}}. \tag{3-3}$$

To correct this error and to expand the equation (3-2) to cases where not all the cell culture area contributes to the measurement, the inclusion of a GCF in the TEER calculation is presented:

$$\mathrm{GCF} = \frac{\mathrm{TEER_t}}{\mathrm{TEER_s}}, \tag{3-4}$$

$$\mathrm{TEER_{GCF}} = (R - R_{\mathrm{blank}})\, A\, \mathrm{GCF}. \tag{3-5}$$

3.2.3 | Simulation strategy

The numerical study was performed by applying a constant current through the current carrying electrodes (current density field $\boldsymbol{J}_1$). To calculate the sensitivity following equation (3-1), an additional simulation was made by exchanging pick-up and current carrying electrodes, i.e., current was applied through the previous pick-up electrodes and voltage was recorded through the previous current carrying electrodes (current density field $\boldsymbol{J}_2$). The Transwell model and each microfluidic model were simulated for different insert diameters (6.5 and 12 mm) and different chamber heights (from 100 to 500 µm), respectively. Simulations were conducted with parametric sweeps of the $\mathrm{TEER_t}$ (from 0 to 10^3 Ω cm^2) spanning the range of the values reported in the literature [37, 38]. The error and GCF were calculated according to equation (3-3) and (3-4) using the current density field $\boldsymbol{J}_1$, where R and the R_{blank} were obtained using Ohm’s law. In particular, R_{blank} was obtained when using the lowest $\mathrm{TEER_t}$, as if there was no cell layer.

The simulation strategy was carried out in two steps: firstly, the sensitivity distribution along the cell barrier was simulated and compared between the different models; secondly, the error of the TEER measurement and the GCF were calculated for each model.

3.2.4 | Experimental validation of interdigitated electrodes configuration

An IDE configuration based on model D was evaluated using a custom-made bioreactor composed of an upper plate, a lower plate, and a permeable membrane, where human cerebral microvascular endothelial cells were cultured to measure the TEER. Figure 3-4 depicts the assembling parts of the bioreactor.

3.2.4.1 | Bioreactor design and fabrication

Ti/Au (20 nm/100 nm) electrodes were patterned on a 188 µm thick cyclo-olefin polymer (COP) film (ZF14–188, Zeon Europe GmbH, DE) in a standard lift-off process. The COP film was bonded to a thicker COP substrate, 4 mm thick (Zeonor 1420R, Zeon Europe GmbH, DE), by means of a double-side pressure-sensitive adhesive (PSA) (ARcare 8939, Adhesive Research Inc., IE). Fluid inlets and outlets were defined in the plates using a CNC milling machine (MDX-40A, Roland DG Corporation, ES) and fluidic connections (male mini luer plugs, Microfluidic ChipShop GmbH, DE) were finally assembled. In order to decrease the electrode polarization impedance, the electrodes were electrochemically coated with a layer of platinum black [39].Impedance spectra measured before and after coating are provided in Figure 3-5.

A commercial porous membrane (Cyclopore polycarbonate (PC) thin clear membrane, 47 mm in diameter, 1 µm of pore size, GE Healthcare Europe GmbH, ES) was modified to be integrated into the bioreactor. Two PSA sheets were cut using a cutting plotter (CAMM-1 Servo GX-24, Roland DG Corporation, ES) to define the cell culture area and bonded to both sides of the membrane. Silicone sheets (platinum cured sheet, 500 µm thick, Silex Ltd., UK) were cut and placed between the plates and the membrane. Apart from defining the chamber height, the silicone sheets also act as the sealing gaskets of the system. The final assembly of the bioreactor was made by sandwiching the modified porous membrane between the upper and lower plates.

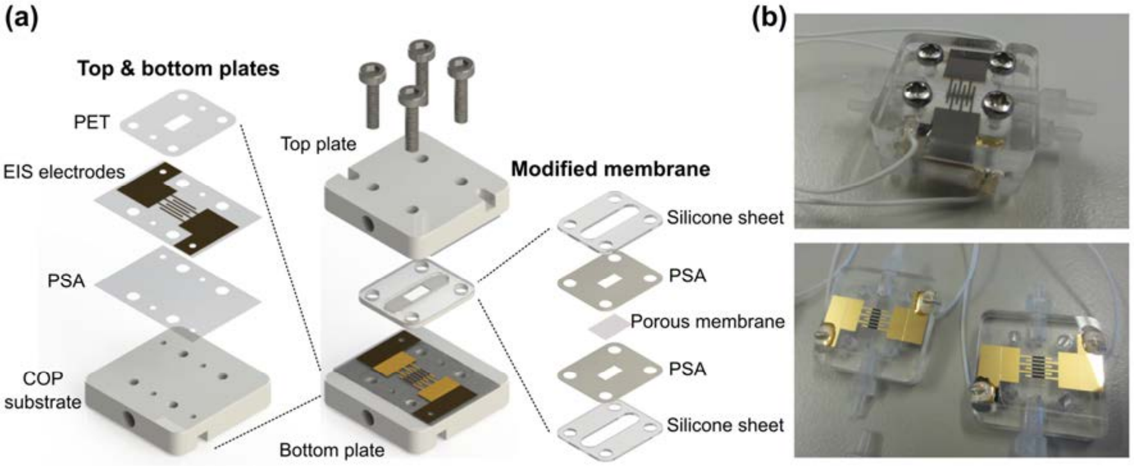

Figure 3-4 Bioreactor fabrication. Assembling parts of the bioreactor including (a) a schematic decomposition of the plates and the modified membrane, and (b) pictures of the bioreactor.

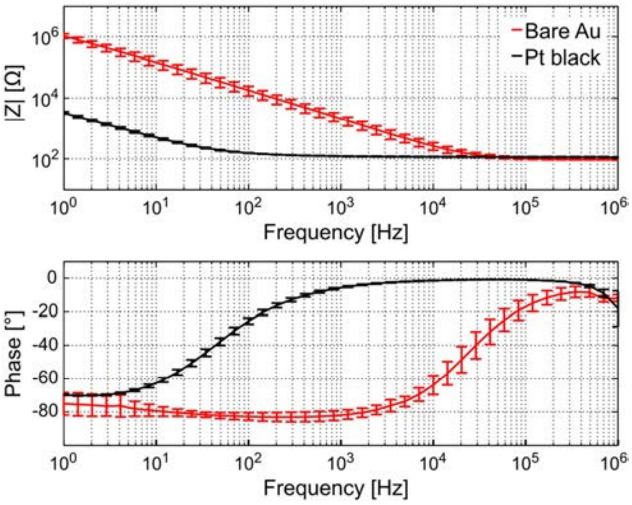

Figure 3-5 Bode plot of the electrode-electrolyte impedance measured in NaCl 0.9 % (w/v) of the fabricated IDEs (vs an auxiliary electrode) before (red line) and after (black line) electrochemical coating of platinum black at -0.2 V during 30 s (n = 3).

3.2.4.2 | Cell culture

Human cerebral microvascular endothelial cell line hCMEC/D3 (obtained from Dr. Couraud, Paris, France), which has been widely used as a model of human blood-brain barrier [40–42], was used to experimentally validate the bioreactor. The modified membranes were sterilized by exposure to UV light for 30 min on each side and placed on a 12-well plate. Before cell seeding, membranes were coated with collagen type I (150 µg ml^{-1} in sterile distilled water), incubated at 37 °C for 1 h, and rinsed three times with phosphate-buffered saline (PBS). Cells were plated on the cell culture area defined on the modified membrane at a concentration of 1.8x10^5 cells cm^{-2} in EBM-2 (Lonza) medium supplemented with 5 % (v/v) foetal bovine serum (FBS) (Sigma-Aldrich), 1.4 µM hydrocortisone (Sigma-Aldrich), 5 µg ml^{-1} ascorbic acid (Sigma-Aldrich), 1 % chemically defined lipid concentrate (Life Technologies), 10 mM HEPES (Life Technologies), 1 ng ml^{-1} human fibroblast growth factor-basic (bFGF) (Sigma-Aldrich) and the antibiotics penicillin (100 U ml^{-1}) and streptomycin (100 µg ml^{-1}). Cells were maintained at 37 °C in a humidified atmosphere containing 5 % CO_2, refreshing growth medium every 2–3 days until used for impedance measurements.

3.2.4.3 | Impedance spectroscopy

TEER values of the cell cultures were obtained using EIS. Impedance spectra were measured at 20 frequencies, ranging from 100 Hz to 1 MHz, using an impedance analysis system [43]. Impedance measurements were performed prior to cell seeding ($\boldsymbol{Z}_{\text{blank}}$) and at 44, 68, 92, and 168 h after cell seeding ($\boldsymbol{Z}_{\text{measured}}$). Each membrane was used for only one measurement to minimize cell damage during handling. The $\boldsymbol{Z}_{\text{blank}}$ was then subtracted from the $\boldsymbol{Z}_{\text{measured}}$ and fitted (using the least-squares method in Matlab) to an equivalent electric circuit that describes the impedance spectra of a cell barrier. This circuit is composed of three elements: two electrical resistances that represent the resistance at low frequencies (i.e., the TEER) and the resistance at high frequencies, here called intercellular resistance (R_i), and a constant phase element (CPE) that describes the dielectric properties of many cell membranes and whose impedance is

$$\mathbf{Z}_{\mathrm{CPE}} = \frac{1}{K(\mathrm{j}\omega)^{\alpha}} \tag{3-6}$$

where j is the imaginary unit, ω is the angular frequency, and K and α are CPE coefficients. Even though the cell membrane of one cell behaves as a capacitance as described in the previous chapter, a CPE usually provides a much better fit to the impedance data, presumably because of the diversity of morphology in cell membranes [44, 45].

3.3 | RESULTS AND DISCUSSION

3.3.1 | Sensitivity distribution

The sensitivity distribution was calculated using the FEM models presented to determine the contribution of each zone of the cell barrier to the measured impedance. This was evaluated according to equation (3-1) and normalized by multiplying by the squared cell culture area. Thus, the optimal sensitivity should be constant and equal to 1. The sensitivity profile along the cell barrier when TEER is measured in the different models is shown in Figure 3-6. As expected, zones close to the electrodes contribute more than zones that are far away and sensitivity uniformity increases with TEER. Notably, sensitivity peaks are placed below the electrodes while sensitivity valleys are found in the middle of pair of electrodes, except for model B, where the major contribution comes from between the pick-up electrodes.

In the Transwell model, the sensitivity field is highly affected by introducing the chopstick electrodes in the periphery of the Transwell insert. Consequently, the sensitivity is non-uniformly distributed and the zone close to the electrode has a higher contribution to the impedance measurement. This accounts for small variations of TEER due to non-reproducibility placement of the chopstick electrodes, which are manually positioned. For a better reproducibility of TEER measurements in Transwell inserts, some commercial systems automates the placement of the chopstick electrodes (REMS AutoSampler, World Precision Instruments Inc., US).

Concerning the microfluidic models, models B and D have a more uniform sensitivity than model C, which presents large differences between zones of the culture area. These differences are higher at both ends of the chamber and lower at the centre. In particular, the sensitivity at the centre is below the 25 % of the optimal when measuring a TEER of $10^1\ \Omega\ \mathrm{cm}^2$. Therefore, impedance measurements performed with model C configuration are just representative of a small zone of the cell culture area.

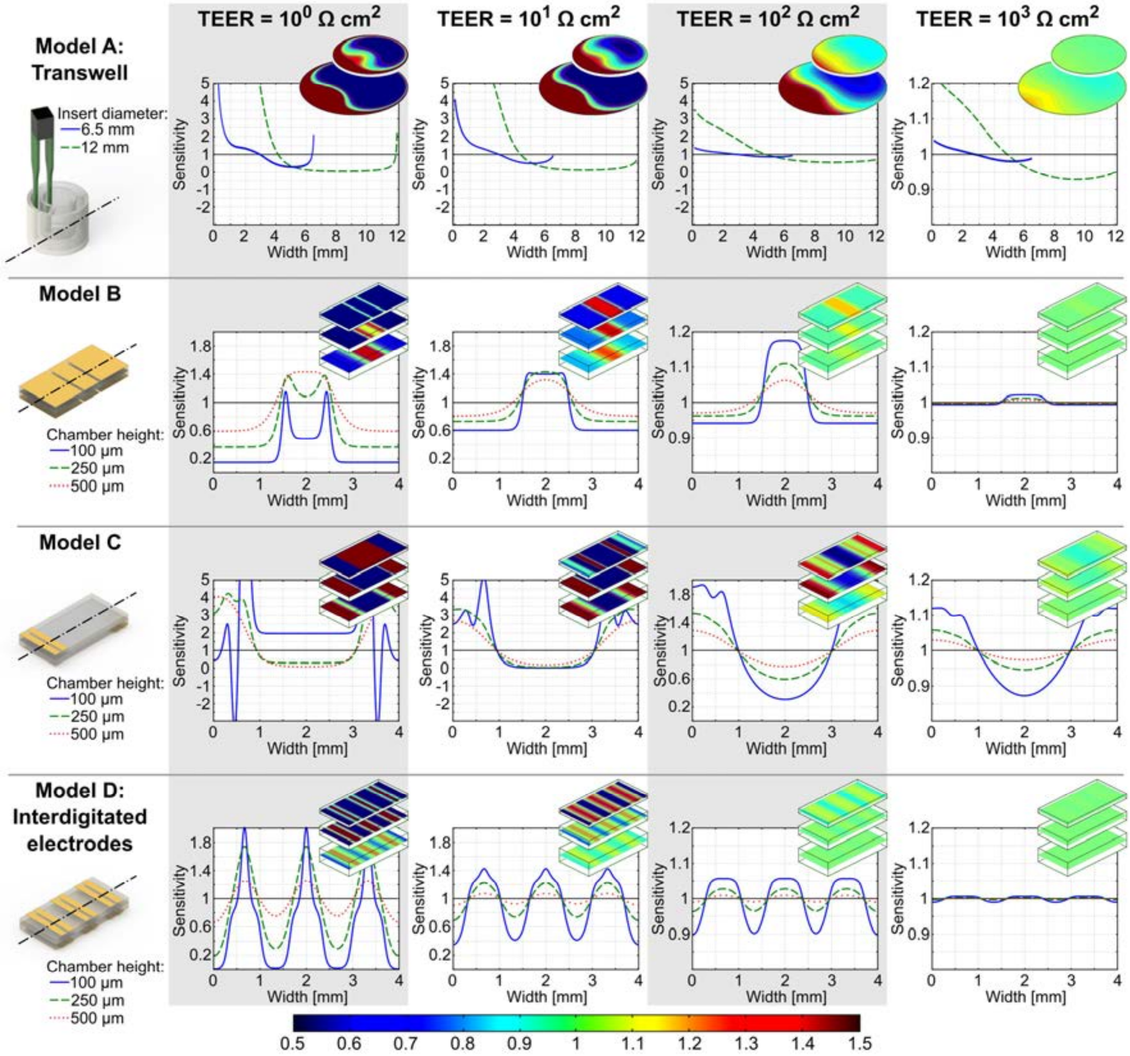

Figure 3-6 Sensitivity distribution along the cell barrier through the axis (dash-dotted line) shown in the 3D scheme of the model at the left of the figure when TEER is measured in a Transwell culture insert using chopstick electrodes (model A) and in the microfluidic model using the three electrode configurations (model B–D). Results are presented for different TEERs (10^0, 10^1, 10^2, 10^3 Ω cm^2), Transwell insert diameters (6.5 and 12 mm) and chamber heights (100, 250, and 500 µm). Data are normalized by multiplying by the squared cell culture area, A^2. Attached to each line graph there is a 2D image to better clarify the sensitivity distribution. Note that axis have different scales.

A dependency of the TEER on the sensitivity has been found for all models. In particular, the higher the TEER, the more uniform is the sensitivity distribution. For the studied models, there are little sensitivity differences when TEER is greater than 10^3 Ω cm^2 (less than 5 % for model B, D and Transwell inserts 6.5 mm in diameter, 12 % for model C, and 23 % for Transwell inserts 12 mm in diameter).

Another feature that highly affects the sensitivity is the chamber geometry, as the sensitivity differs widely between different insert diameters and chamber heights. The sensitivity field in a Transwell insert is less uniform as its diameter increases, because larger Transwell inserts have zones further away from the chopstick electrodes that contribute little to the measurement. For example, in 12 mm Transwell inserts and TEERs of 10^1 Ω cm^2, the sensitivity field over half of the cell barrier area is less than

25 % of the optimal sensitivity. Furthermore, decreasing the chamber height in microfluidic models is usually detrimental for the sensitivity field. Thus, the most uniform sensitivity is achieved for the larger chamber height (500 µm) in all models.

3.3.2 | Geometric correction factor

TEER may be calculated incorrectly using equation (3-2) because of a non-uniform sensitivity field. This error has been calculated according to equation (3-3) and it is shown in Figure 3-7 for the different simulated models Using the equation (3-5) here proposed, which includes a GCF, can solve this issue. The GCF value that should be used in the calculation of TEER for the different simulated models is shown in Figure 3-8. A GCF close to 1 means that there is no error when calculating TEER using the total cell culture area. Otherwise, a GCF away from 1 means that there is a significant error.

In general, the higher the TEER, the less is the error (i.e., error closer to 0 in Figure

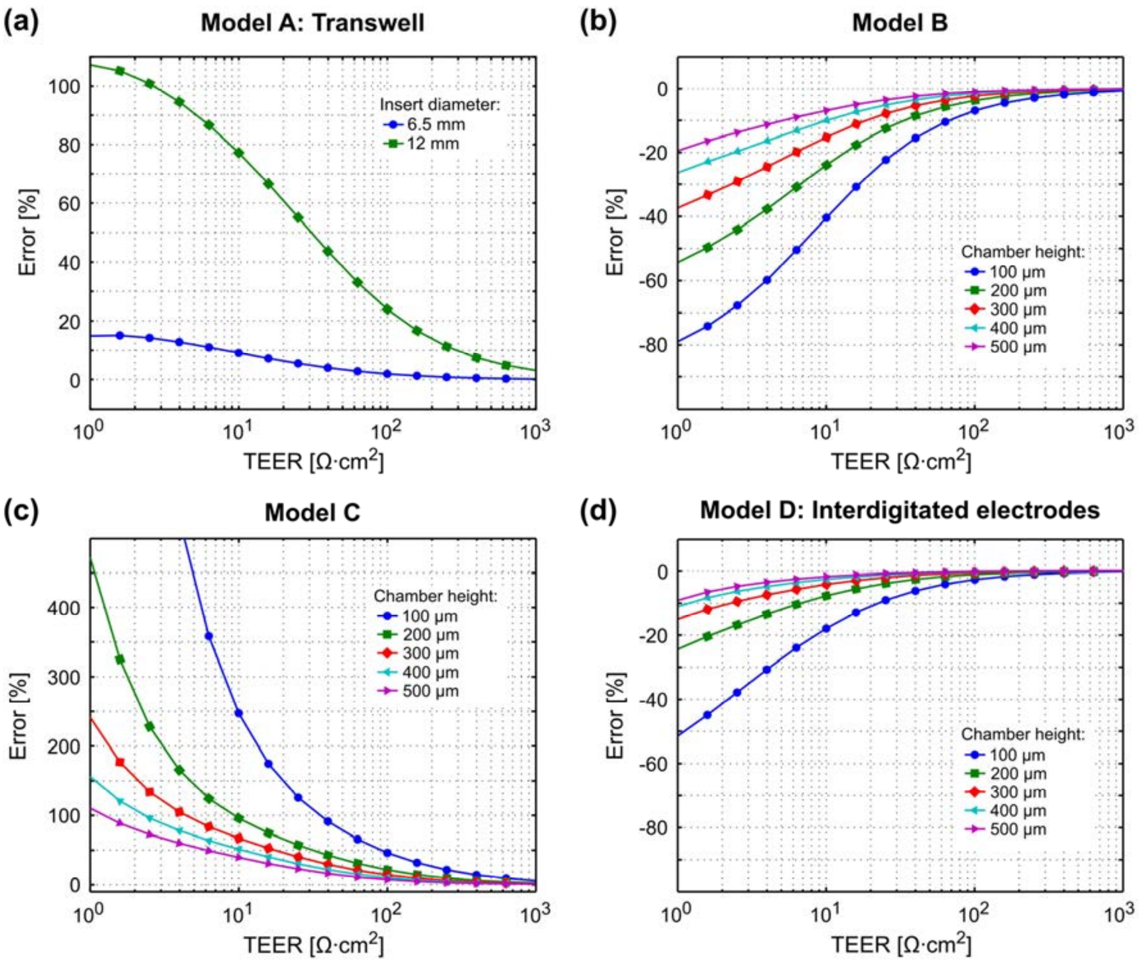

Figure 3-7 Error (%) when TEER is measured in (a) a Transwell insert using chopstick electrodes (model A) and in (b–d) microfluidic models using the three electrodes configurations ((b) models B, (c) C, and (d) D). Results are presented for different Transwell insert diameters (6.5 and 12 mm) and chamber heights (from 100 to 500 µm).

3-7 and GCF closer to 1 in Figure 3-8). This is in agreement with the results of the previous section. In all models, GCF is closer to 1 (0.95–1) for a TEER of 10^3 Ω cm^2 and it is expected to be maintained for higher TEERs. Unfortunately, for lower TEER values, the error considerably increases. For example, for a TEER of 10^1 Ω cm^2, GCF in Transwell inserts are 0.92 (6.5 mm in diameter) and 0.56 (12 mm in diameter), while for microfluidic models with 200 µm in height are 1.32 (model B), 0.51 (model C) and 1.09 (model D). Thus, using a GCF becomes important for cell cultures with low TEERs. Another important aspect to consider is that the GCF is lower than 1 in model A and C, which means an overestimation of TEER, whereas GCF is higher than 1 in model B and D, which means an underestimation of TEER. Therefore, there will be large differences when comparing measurements systems with GCF > 1 against those with GCF < 1.

It is well known that the TEER measurements performed with chopstick electrodes in Transwell inserts 24 mm or larger in diameter should not be multiplied by their area. Nevertheless, we evidence that measurements of low TEER values with

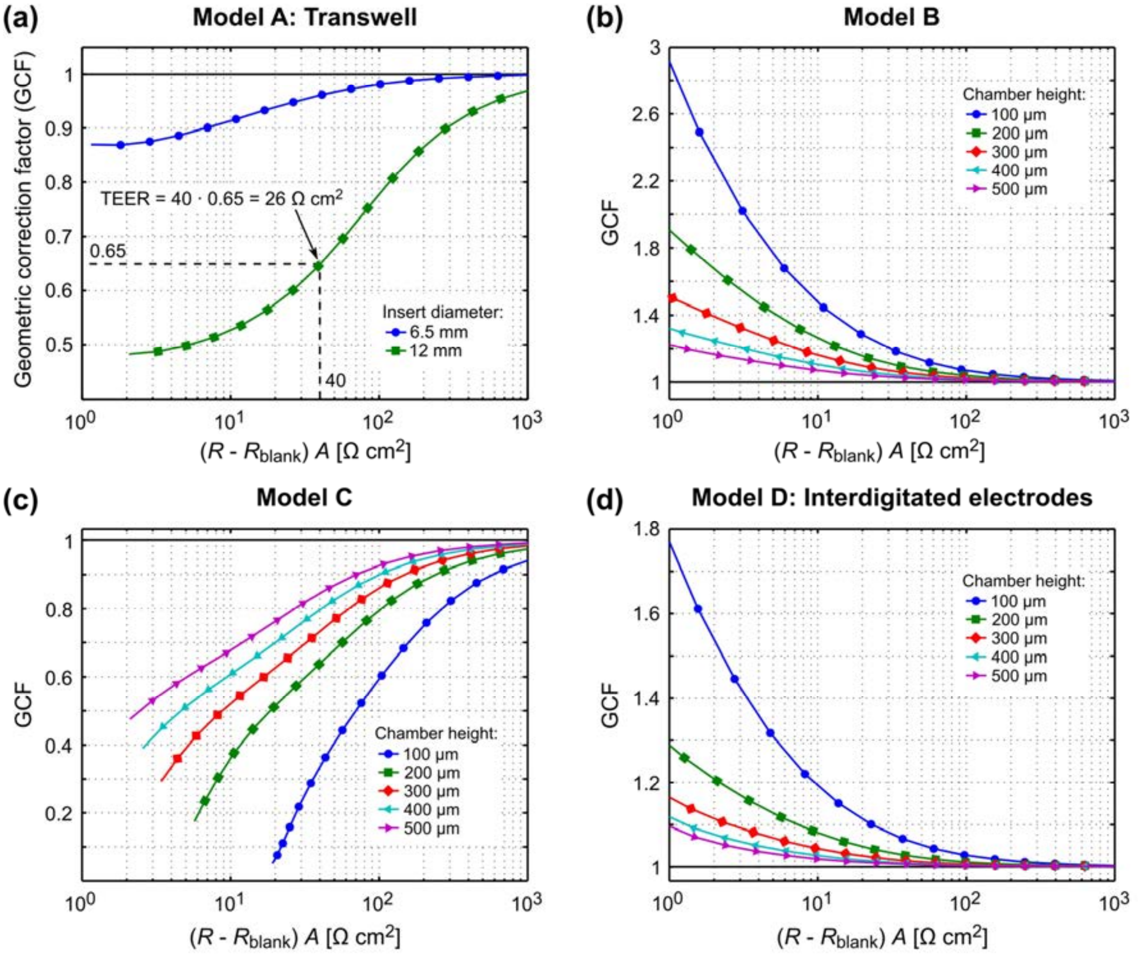

Figure 3-8 GCF when TEER is measured in (a) a Transwell insert using chopstick electrodes (model A) and in (b–d) microfluidic models using the three electrodes configurations ((b) models B, (c) C, and (d) D). Results are presented for different Transwell insert diameters (6.5 and 12 mm) and chamber heights (from 100 to 500 µm). Example of how to apply the GCF in Transwell inserts of 12 mm in diameter (a); a TEER of 40 Ω cm^2 calculated using the total cell culture area would be 26 Ω cm^2 after be corrected.

inserts 12 mm in diameter are also inaccurate and should need a GCF, as shown in Figure 3-8a.

For the microfluidic models, GCF value is highly dependent on the chamber height. In particular, GCF for a TEER of $10^1\ \Omega\ \mathrm{cm}^2$ varies by 27 % (model B), -44 % (model C), and 12 % (model D) by just changing the height from 200 µm to 100 µm. This illustrates the importance of considering the chamber geometry and the electrode size and placement when designing TEER measurement electrodes.

In model B, it could be understood that a large current electrode is more appropriate, but this is not entirely true in tetrapolar electrode configurations because there are zones of positive and negative sensitivity. In this case, maximum sensitivity is concentrated between pick-up electrodes (Figure 3-6). In model C, the accuracy is worse than in model B as the narrowness of the chamber obstruct the electrical current to flow through the cell barrier in areas away from the electrodes. This is similar to what happens in bipolar configurations with electrodes placed at inlets and outlets of the microfluidic chambers. Therefore, placing the electrodes at inlets and outlets of microfluidic systems can become a limiting factor for obtaining an accurate TEER measurement if it is determined according to equation (3-2) without any correction.

Interestingly, the model D has a GCF closer to 1 than both model B and C despite covering less than half of the surface area with electrodes. An optimal accuracy in model D is achieved when the distance between the centres of the pick-up and current carrying electrodes (400 µm) is comparable to the chamber height. For that reason, GCF becomes significant for chamber height of 100 µm (1.2 at TEER of $10^1\ \Omega\ \mathrm{cm}^2$). A strategy to reduce the error in lower chamber heights could be to decrease the distance between current carrying and pick-up electrodes.

3.3.3 | Experimental impedance measurements

Geometrical dimensions of the fabricated bioreactor slightly differed from those in model D (Figure 3-9a). The sensitivity distribution and the error for this particular electrode configuration were calculated as in the previous simulation study (Figure 3-9b). These results demonstrate a good accuracy of the measurement system in a wide range of TEER values. EIS measurements performed before cell seeding and 7 days after seeding of an hCMEC/D3 monolayer are shown in Figure 3-9d. The impedance at low frequencies (associated with paracellular pathways) was purely resistive and increased from 125 Ω to 359 Ω after 7 days of cell culture, while the impedance at high frequencies (associated with paracellular and intracellular pathways) remained almost unchanged. This behaviour is due to the growth of the cell culture that implied a tightening of the space between cells.

In detail, TEER increased from $10.4 \pm 1.8\ \Omega\ \mathrm{cm}^2$ at 44 h to $18.7 \pm 2.4\ \Omega\ \mathrm{cm}^2$ at 7 days (Figure 3-9e). TEER values reported in the literature for hCMEC/D3 monolayers under static conditions are typically in the range from 10 to $40\ \Omega\ \mathrm{cm}^2$ [1, 3, 40].

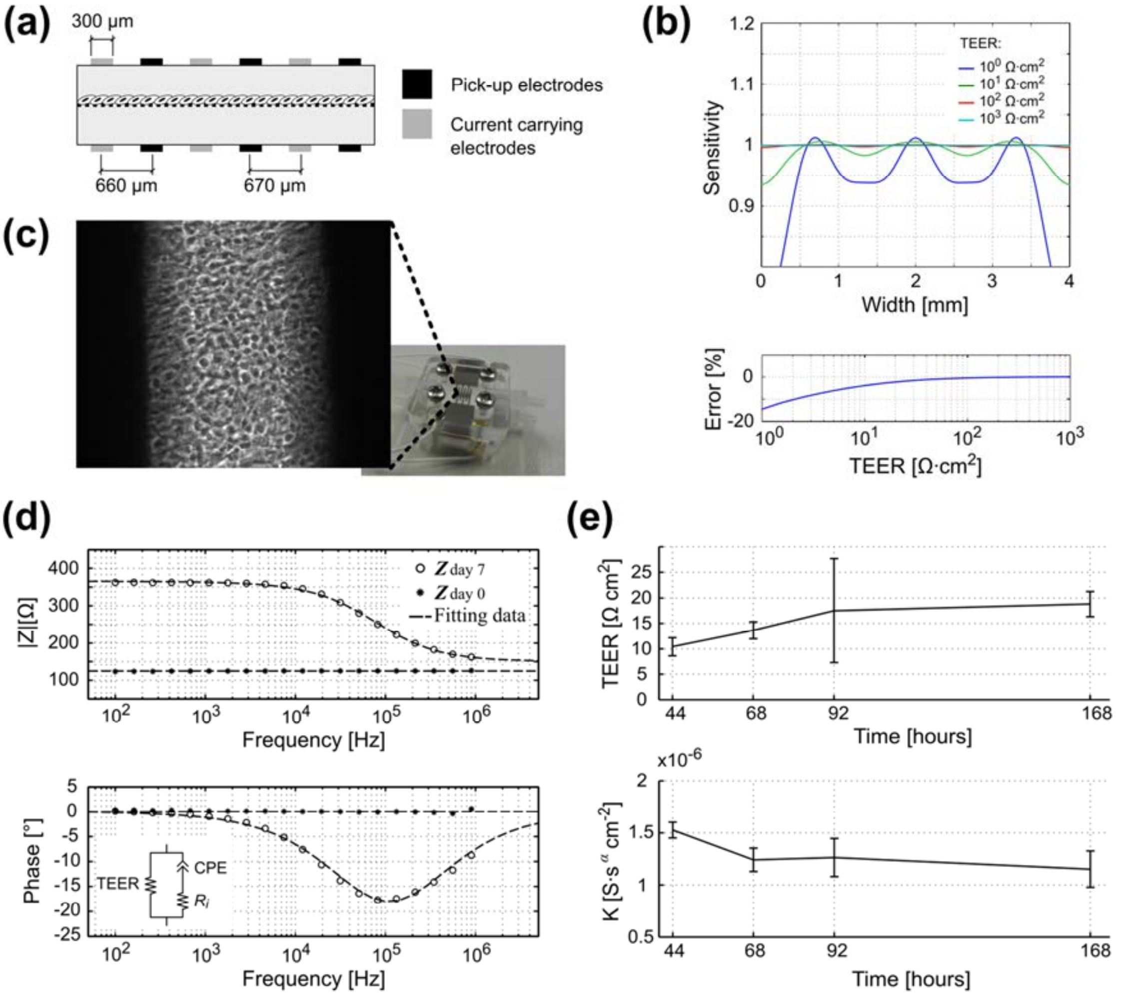

Figure 3-9 Experimental validation of interdigitated electrodes (IDE) configuration. (a) Cross-sectional schematic of the fabricated bioreactor. (b) Numerical study of the sensitivity distribution over the cell barrier and expected error (%). (c) Phase-contrast image of the cells within the bioreactor. Note that the image corresponds to the space between opaque electrodes. Impedance spectroscopy data (d) before cell seeding (asterisks) and after 7 days of hCMEC/D3 culture (circles). (e) Time course of the fitting data (dashed line) according to the equivalent electric circuit including TEER, R_i, and CPE (n = 2).

Concerning the K parameter (related to the CPE), it decreased from $1.53 \pm 0.08\ \mu S\ s^{\alpha}\ cm^{-2}$ at 44 h to $1.15 \pm 0.17\ \mu S\ s^{\alpha}\ cm^{-2}$ at 7 d. The rest of the parameters did not show any time dependency ($R_i = 39.6 \pm 9.8\ \Omega$, $\alpha = 0.84 \pm 0.02$).

TEER could be directly determined by the resistance difference between high and low frequencies [17, 23], thereby a blank measure would not be necessary. In this study, all measured impedances at 1 MHz were not purely resistive (phase equal to -7.1 ± 1.9 °); thus, the direct determination of TEER using the estimated resistance at high frequencies (parallel resistance of TEER and R_i) would have implied a variation of $2.6 \pm 0.6\ \Omega\ cm^2$. I suggest that this low resistance presumably accounts for the electrical resistivity of the intercellular space, being slightly higher than the extracellular media. In any case, this resistance may be negligible and ignored when measuring tight endothelia which have TEER values that are some orders of magnitude higher.

3.4 | CONCLUSIONS

Despite the disparities of TEER values reported in the literature, few works have studied their sources. In this chapter, it is highlighted the geometric determinants when dealing with TEER measurements and the feasibility of using a GCF to calculate the TEER. In addition, the sensitivity distribution has been presented as an important aspect to consider when designing TEER measurement electrodes.

As a result, the errors when no GCF is used are higher for low TEER values when using larger Transwell insert diameters or lower microfluidic chamber heights. Interestingly, but not surprisingly, measuring TEER in Transwell systems using chopstick electrodes, the gold standard method in which most of the TEER values obtained in microfluidic systems are compared, is not exempt from error. It has been found that such error has different sign for different systems, resulting in large differences when comparing systems that have errors of opposite sign.

By numerical simulations, it is described a simple method to determine the GCF of a particular measurement system that can correct this error, so that the correction can be applied retrospectively to their measurements. In addition, system with nonobvious current distribution that report TEER values in units of Ω instead of $\Omega\ \mathrm{cm}^2$, such as Transwell inserts of 24 mm in diameter or peculiar microfluidic cell cultures [46], could determine their particular GCF that allows comparing their TEER values with those reported in the literature.

A proposed IDE configuration based on the obtained simulation results was also presented and experimentally validated by integrating the impedance measurement electrodes in a custom-made bioreactor. This configuration, besides being more accurate for measuring the TEER, also allows the optical visualisation of the cell culture which is usually necessary. These characteristics should be very useful for the development of future microfluidic systems that pretend to emulate and monitor different cell barrier functions.

3.5 | REFERENCES

[1] Hatherell K, Couraud P-O, Romero IA, et al. Development of a three-dimensional, all-human in vitro model of the blood–brain barrier using mono-, co-, and tri-cultivation Transwell models. *J Neurosci Methods* 2011; 199: 223–229.

[2] Nakagawa S, Deli MA, Kawaguchi H, et al. A new blood-brain barrier model using primary rat brain endothelial cells, pericytes and astrocytes. *Neurochem Int* 2009; 54: 253–263.

[3] Eigenmann DE, Xue G, Kim KS, et al. Comparative study of four immortalized human brain capillary endothelial cell lines, hCMEC/D3, hBMEC, TY10, and

BB19, and optimization of culture conditions, for an in vitro blood–brain barrier model for drug permeability studies. *Fluids Barriers CNS* 2013; 10: 33.

[4] Tsata V, Velegraki A, Ioannidis A, et al. Effects of Yeast and Bacterial Commensals and Pathogens of the Female Genital Tract on the Transepithelial Electrical Resistance of HeLa Cells. *Open Microbiol J* 2016; 10: 90–96.

[5] Booth R, Kim H. Characterization of a microfluidic in vitro model of the blood-brain barrier (μBBB). *Lab Chip* 2012; 12: 1784–1792.

[6] Walter FR, Valkai S, Kincses A, et al. A versatile lab-on-a-chip tool for modeling biological barriers. *Sens Actuators B Chem* 2016; 222: 1209–1219.

[7] Prabhakarpandian B, Shen M-C, Nichols JB, et al. SyM-BBB: a microfluidic blood brain barrier model. *Lab Chip* 2013; 13: 1093–1101.

[8] Jang K-J, Suh K-Y. A multi-layer microfluidic device for efficient culture and analysis of renal tubular cells. *Lab Chip* 2010; 10: 36–42.

[9] Ferrell N, Desai RR, Fleischman AJ, et al. A microfluidic bioreactor with integrated transepithelial electrical resistance (TEER) measurement electrodes for evaluation of renal epithelial cells. *Biotechnol Bioeng* 2010; 107: 707–716.

[10] Huang H-C, Chang Y-J, Chen W-C, et al. Enhancement of Renal Epithelial Cell Functions through Microfluidic-Based Coculture with Adipose-Derived Stem Cells. *Tissue Eng Part A* 2013; 19: 2024–2034.

[11] Huh D, Matthews BD, Mammoto A, et al. Reconstituting Organ-Level Lung Functions on a Chip. *Science* 2010; 328: 1662–1668.

[12] Wegener J, Abrams D, Willenbrink W, et al. Automated multi-well device to measure transepithelial electrical resistances under physiological conditions. *BioTechniques* 2004; 37: 590–597.

[13] Gaillard PJ, Voorwinden LH, Nielsen JL, et al. Establishment and functional characterization of an in vitro model of the blood-brain barrier, comprising a co-culture of brain capillary endothelial cells and astrocytes. *Eur J Pharm Sci* 2000; 12: 215–222.

[14] Benson K, Cramer S, Galla H-J. Impedance-based cell monitoring: barrier properties and beyond. *Fluids Barriers CNS* 2013; 10: 5.

[15] Vogel PA, Halpin ST, Martin RS, et al. Microfluidic transendothelial electrical resistance measurement device that enables blood flow and postgrowth experiments. *Anal Chem* 2011; 83: 4296–4301.

[16] Srinivasan B, Kolli AR, Esch MB, et al. TEER Measurement Techniques for In Vitro Barrier Model Systems. *J Lab Autom* 2015; 20: 107–126.

[17] Odijk M, Meer AD van der, Levner D, et al. Measuring direct current transepithelial electrical resistance in organ-on-a-chip microsystems. *Lab Chip* 2015; 15: 745–752.

[18] Bera TK. Bioelectrical Impedance Methods for Noninvasive Health Monitoring: A Review. *J Med Eng* 2014; 2014: 1–28.

[19] Brown BH, Wilson AJ, Bertemes-Filho P. Bipolar and tetrapolar transfer impedance measurements from volume conductor. *Electron Lett* 2000; 36: 2060–2062.

[20] Griep LM, Wolbers F, Wagenaar B de, et al. BBB ON CHIP: microfluidic platform to mechanically and biochemically modulate blood-brain barrier function. *Biomed Microdevices* 2013; 15: 145–150.

[21] Douville NJ, Tung Y-C, Li R, et al. Fabrication of two-layered channel system with embedded electrodes to measure resistance across epithelial and endothelial barriers. *Anal Chem* 2010; 82: 2505–2511.

[22] Grimnes S, Martinsen ØG. Sources of error in tetrapolar impedance measurements on biomaterials and other ionic conductors. *J Phys Appl Phys* 2007; 40: 9–14.

[23] Wegener J, Seebach J. Experimental tools to monitor the dynamics of endothelial barrier function: a survey of in vitro approaches. *Cell Tissue Res* 2014; 355: 485–514.

[24] Blume L-F, Denker M, Gieseler F, et al. Temperature corrected transepithelial electrical resistance (TEER) measurement to quantify rapid changes in paracellular permeability. *Pharmazie* 2010; 65: 19–24.

[25] Smith J, Wood E, Dornish M. Effect of Chitosan on Epithelial Cell Tight Junctions. *Pharm Res* 2004; 21: 43–49.

[26] Gye MC. Changes in the expression of claudins and transepithelial electrical resistance of mouse Sertoli cells by Leydig cell coculture. *Int J Androl* 2003; 26: 271–278.

[27] Fajdiga S, Koninkx JFJG, Tooten PCJ, et al. Interference of Salmonella enteritidis and Lactobacillus spp. with IL-8 levels and transepithelial electrical resistance of enterocyte-like caco-2 cells. *Folia Microbiol (Praha)* 2006; 51: 268–272.

[28] Neuhaus W, Plattner VE, Wirth M, et al. Validation of in vitro cell culture models of the blood–brain barrier: Tightness characterization of two promising cell lines. *J Pharm Sci* 2008; 97: 5158–5175.

[29] Sultana R, McBain AJ, O’Neill CA. Strain-Dependent Augmentation of Tight-Junction Barrier Function in Human Primary Epidermal Keratinocytes by Lactobacillus and Bifidobacterium Lysates. *Appl Environ Microbiol* 2013; 79: 4887–4894.

[30] Xie Y, Ye L, Zhang X, et al. Transport of nerve growth factor encapsulated into liposomes across the blood–brain barrier: In vitro and in vivo studies. *J Controlled Release* 2005; 105: 106–119.

[31] Man S, Ubogu EE, Williams KA, et al. Human Brain Microvascular Endothelial Cells and Umbilical Vein Endothelial Cells Differentially Facilitate Leukocyte Recruitment and Utilize Chemokines for T Cell Migration. *J Immunol Res* 2008; 2008: 1–8.

[32] Calabro AR, Konsoula R, Barile FA. Evaluation of in vitro cytotoxicity and paracellular permeability of intact monolayers with mouse embryonic stem cells. *Toxicol In Vitro* 2008; 22: 1273–1284.

[33] Bridger PS, Menge C, Leiser R, et al. Bovine Caruncular Epithelial Cell Line (BCEC-1) Isolated from the Placenta Forms a Functional Epithelial Barrier in a Polarised Cell Culture Model. *Placenta* 2007; 28: 1110–1117.

[34] Ablonczy Z, Crosson CE. VEGF modulation of retinal pigment epithelium resistance. *Exp Eye Res* 2007; 85: 762–771.

[35] Huang C, Ramadan Q, Wacker JB, et al. Microfluidic chip for monitoring Ca2+ transport through a confluent layer of intestinal cells. *RSC Adv* 2014; 4: 52887–52891.

[36] Franks W, Schenker I, Schmutz P, et al. Impedance characterization and modeling of electrodes for biomedical applications. *IEEE Trans Biomed Eng* 2005; 52: 1295–1302.

[37] Garberg P, Ball M, Borg N, et al. In vitro models for the blood–brain barrier. *Toxicol In Vitro* 2005; 19: 299–334.

[38] Deli MA, Ábrahám CS, Kataoka Y, et al. Permeability Studies on In Vitro Blood–Brain Barrier Models: Physiology, Pathology, and Pharmacology. *Cell Mol Neurobiol* 2005; 25: 59–127.

[39] Gabriel G, Erill I, Caro J, et al. Manufacturing and full characterization of silicon carbide-based multi-sensor micro-probes for biomedical applications. *Microelectron J* 2007; 38: 406–415.

[40] Weksler BB, Subileau EA, Perrière N, et al. Blood-brain barrier-specific properties of a human adult brain endothelial cell line. *FASEB J* 2005; 19: 1872–1874.

[41] Poller B, Gutmann H, Krähenbühl S, et al. The human brain endothelial cell line hCMEC/D3 as a human blood-brain barrier model for drug transport studies. *J Neurochem* 2008; 107: 1358–1368.

[42] Cucullo L, Couraud P-O, Weksler B, et al. Immortalized human brain endothelial cells and flow-based vascular modeling: A marriage of convenience for rational neurovascular studies. *J Cereb Blood Flow Metab* 2008; 28: 312–328.

[43] Guimerà A, Gabriel G, Parramon D, et al. Portable 4 Wire Bioimpedance Meter with Bluetooth Link. In: Dössel O, Schlegel WC, Magjarevic R (eds) *World Congress on Medical Physics and Biomedical Engineering*. Berlin: Springer, pp. 868–871.

[44] Grimnes S, Martinsen ØG. . In: *Bioimpedance and Bioelectricity Basics, 2nd Edition*. Amsterdam: Elsevier, pp. 283–332.

[45] Ando Y, Mizutani K, Wakatsuki N. Electrical impedance analysis of potato tissues during drying. *J Food Eng* 2014; 121: 24–31.

[46] Deosarkar SP, Prabhakarpandian B, Wang B, et al. A Novel Dynamic Neonatal Blood-Brain Barrier on a Chip. *PLOS ONE* 2015; 10: e0142725.

4

A perfusion chamber for monitoring transepithelial NaCl transport in an in vitro model of the renal tubule

Transepithelial electrical measurements in the renal tubule have provided a better understanding of how kidney regulates electrolyte and water homeostasis through the reabsorption of molecules and ions (e.g., H_2O and NaCl). While experiments and measurement techniques using native tissue are difficult to prepare and to reproduce, cell cultures conducted largely with the Ussing chamber lack the effect of FSS which is a key physiological stimulus in the renal tubule. To overcome these limitations, it is presented a modular perfusion chamber with integrated electrodes for long-term culture of renal epithelial cells under flow that allows the continuous and simultaneous monitoring of both transepithelial electrical parameters and transepithelial NaCl transport. The latter is obtained from electrical conductivity measurements since Na^+ and Cl^- are the ions that contribute most to the electrical conductivity of a standard physiological solution. The system was validated with tight and leaky epithelial monolayers that were characterized electrophysiologically for 5 days under different flow conditions (i.e., apical perfusion, basal, or both). In addition, apical to basal chemical gradients of NaCl (140/70 and 70/140 mM) were imposed in order to demonstrate the feasibility of this methodology for quantifying and monitoring in real time the transepithelial reabsorption of NaCl, which is a primary function of the renal tubule.

Most of the contents of this chapter have been published in:

[1] **Yeste J**, Martínez-Gimeno L, Illa X, Laborda P, Guimerà A, Sánchez-Marín JP, Villa R, Giménez I. A perfusion chamber for monitoring transepithelial NaCl transport in an in vitro model of the renal tubule. *Biotechnol Bioeng* 2018; 115: 1604–1613.

4.1 | INTRODUCTION

Transepithelial electrical measurements of the renal tubule—carried out by *in vivo* micropuncture [1], *ex vivo* isolated microperfused tubule [2–4], or *in vitro* cell culture [5]—have provided a better understanding of the renal function and its reabsorption capacity. Although the best methodology is to use native tissue, these experiments and measurement techniques have poor reproducibility and are time-limited and difficult to prepare. In addition, the size and architecture of the renal tubule has made difficult to apply *in vitro* tools, like the versatile Ussing chamber [6, 7] that has been instrumental in understanding function of other epithelia (e.g., intestinal or placental epithelia), to excised tubules. For these reasons and also due to ethical issues of animal testing, *in vitro* research for polarized renal epithelium has been limited to studies on Transwell devices [8, 9]. Nowadays microfluidic cell cultures have become more popular as cells can be exposed to fluid shear stress (FSS) [10–12], which is an important physiological stimulus for renal epithelial cells [13]. Despite conventional Ussing-like chambers do not allow the effect of FSS, they are still widely used for electrophysiological measurements of the renal tubule. Therefore, sensing capabilities in these microphysiological systems, similar to those of the Ussing chamber, will be useful to study the renal function in a more physiological microenvironment.

In addition to the TEER, the cell layer capacitance (C_{cl}) can be also obtained by means of EIS [14, 15], which can yield information about the membrane surface area and how much it is folded since the capacitance of unfolded biological membranes is relatively constant around 1 $\mu F\ cm^{-2}$ [16]. This parameter serves to identify the formation of complex surface morphologies such as microvilli structures [17, 18]. Some authors have developed microfluidic systems with integrated electrodes [19, 20] or also organic electrochemical transistors [21] for the evaluation of renal epithelial cells under flow.

Renal reabsorption takes place in the renal tubule, which is divided into proximal tubule (PT), loop of Henle, and distal nephron (comprising the distal convoluted tubule [DCT], connecting tubule, and collecting ducts). Each segment exhibits different absorptive capabilities and is exposed to particular electrochemical gradients across epithelium. For example, the PT reabsorbs the 65 % of the filtered Na^+, whereas the thick ascending limb (TAL) segment of the loop of Henle and the DCT reabsorb the 25 % and the 5 %, respectively [22]. Na^+ and Cl^- are reabsorbed in the renal tubule from the luminal space to the peritubular capillaries. As a result, much of these ions return from the filtrate to the bloodstream instead of being excreted. Renal epithelial cells manage this reabsorption transporting ions from apical side, which faces lumen, to basolateral side that contacts capillaries in the intertubular space.

An important mechanical stimulus for renal epithelial cells is FSS. Although poorly understood, mechanotransduction that initiates signalling cascade is mediated on the microvilli and primary cilia through motion, molecular sensors, or both. In tubular epithelial cells cultured *in vitro*, physiological levels of FSS alters cytoskeletal organization and transport proteins resulting in enhanced epithelial cell phenotype [23–25]. On the other hand, pathological levels of FSS may be responsible for losing of epithelial characteristics that may account for the progression of chronic kidney disease [26, 27], which is estimated to affect 8–16 % of the adult population worldwide.

In the previous chapter, it was described a chamber system with integrated electrodes to perform impedance analysis of epithelial or endothelial cell monolayers. In this chapter, it is presented a similar platform system adapted to have a larger cultivation area and to permit three simultaneous experiments under flow conditions. This perfusion chamber has enabled long-term culture of renal epithelial cells under flow and has allowed—using the same electrodes—the continuous and simultaneous monitoring of transepithelial electrical parameters and transepithelial NaCl transport. Since Na^+ and Cl^- are the ions that contribute most to the electrical conductivity of a standard physiological solution, their concentration can be estimated from the conductivity. Therefore, it is possible to determine the transport of NaCl by measuring the electrical conductivity in the apical and basal compartments. In the present study, we have electrophysiologically characterized in the perfusion chamber epithelial monolayers obtained with two rat cell lines representing the PT (NRK-52E) and TAL (raTAL) segments in the nephron. This *in vitro* model of the renal tubule was used to validate the measurement system capable to measure the TEER, the C_{cl}, and the conductivity of apical and basal compartments. For that purpose, an apical to basal gradient of NaCl in both epithelial monolayers was imposed in order to follow the transport of NaCl. In this way, it is possible to monitor in real time the transcellular chemical gradient of NaCl either imposed or produced by active transporters.

4.2 | MATERIALS AND METHODS

4.2.1 | Perfusion chamber design and fabrication

The custom-made perfusion chamber is similar to that described in the previous chapter. The device is composed of two plates and a disposable membrane with three cell culture areas of 0.8 cm^2 (4 x 20 mm) (Figure 4-1a and Figure 4-1b). In detail, Ti/Au (200/20 nm) electrodes were patterned on 188 µm thick COP film in a standard lift-off process. This film was then thermally bonded to a 2 mm thick COP substrate by means of a hot press (PW 40, Paul Otto Weber GmbH, DE) at 136 ºC and 10 kN for 7 min. To define the fluidic channels, a 100 µm thick COP film was cut using a cutting plotter (CAMM-1 Servo GX-24, Roland DG Corporation, ES) and bonded on top of the electrodes. For that, we employed a thermally-solvent assisted method consisting in 10 min of cyclohexane vapour exposure followed by 20 min of pressure at 65 ºC and 5 kN. Plates were completely made of COP and had integrated electrodes to perform EIS. Pads of the electrodes were soldered to electric wires and covered with epoxy. Fluid inlets and outlets were defined in the plates using the CNC milling machine. The electrodes were then electrochemically coated with a layer of platinum black [28] in order to decrease the electrode polarization impedance

Polyethylene terephthalate (PET) porous membranes of 0.4 µm of pore size (ipCELLCULTURE membranes, it4ip SA, BE) and polycarbonate (PC) porous membranes of 1 µm of pore size (Whatman Cyclopore, GE Healthcare Europe GmbH, Barcelona, ES) were modified to be integrated into the perfusion chamber. Two silicone sheets (platinum cured sheet, Silex Ltd., UK) of 0.5 mm in thickness were cut using a cutting plotter and bonded to both sides of the membrane using double-side pressure-sensitive adhesive (PSA) (ARcare 8939, Adhesives Research Ireland Ltd., Limerick, IE). These silicone sheets were used to define the apical and basal compartments (5 x 25 mm in area), both resulting in a total height of 0.7 mm (silicone plus PSA and COP) and a volume of ~87 µL. The final assembly of the device was made by sandwiching the modified membrane between the plates and, in turn, between two steel plates that were screwed together to keep the system fluidically sealed. Altogether, the perfusion chamber comprises three replicas of a double compartment system separated by a porous membrane and with independent electrodes; therefore, three experiments can be performed simultaneously.

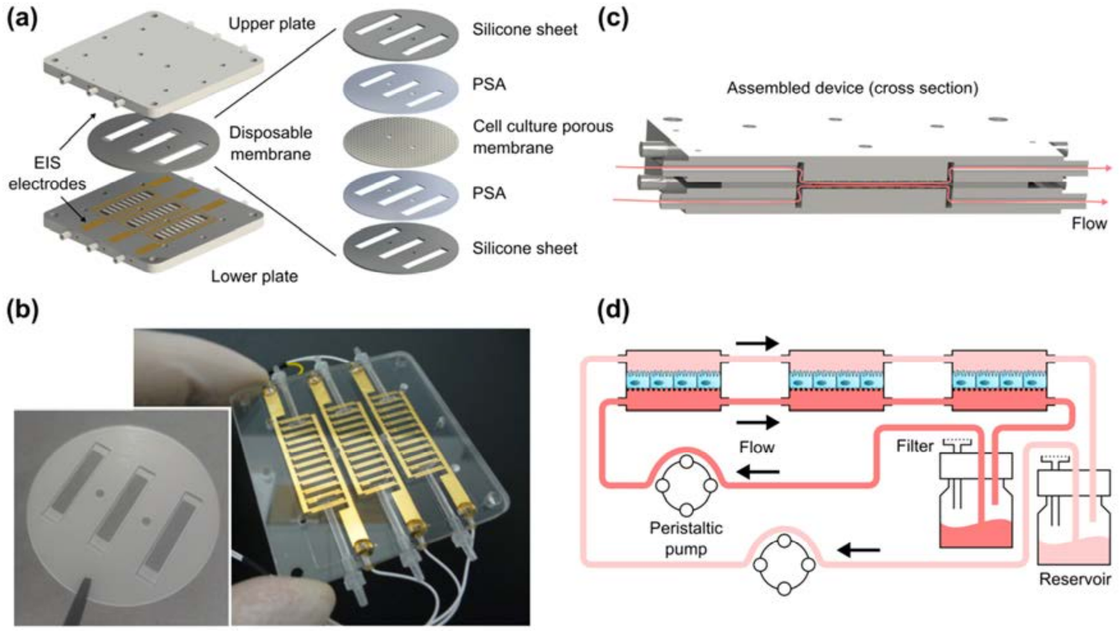

Figure 4-1 Perfusion chamber assembling and experimental set-up. (a) Assembling parts of the system including upper plate, lower plate, and disposable membrane. There is also included a schematic decomposition of the disposable membrane fabrication. This is formed through a stack of layers consisted of two silicone sheets (0.5 mm in thickness), two double-sided PSA layers, and a tissue-culture treated polyethylene terephthalate (PET) porous membrane of 0.4 µm of pore size and 10 µm in thickness. (b) Pictures of the disposable membrane and a plate. Note that upper and lower plates are identical. (c) Cross-section of the assembled device with detail (pink arrows) of flow paths. (d) Schematic representation of the fluidic system. Two identical fluidic circuits were mounted to control independently the apical and basal flow. The three apical or basal compartments were connected in series with silicone tubing, and the circuit was closed through a reservoir and a peristaltic pump.

4.2.2 | Cell culture

Epithelial monolayers were obtained with two immortalized rat cell lines representing PT (NRK-52E, ATCC, Manassas, VA) and TAL (raTAL; donation from N. Ferreri, New York Medical College Valhalla, NY, [29]) phenotypes. Both cell lines were adapted to grow on low-serum culture medium supplemented with insulin (5 µg mL^{-1}), transferrin (5 µg mL^{-1}), sodium selenite (60 nM), dexamethasone (0.05 µM), triiodothyronine (1 nM), and epidermal growth factor 10 (ng mL^{-1}) (Sigma-Aldrich, Quimica SL, Madrid, ES), specifically tailored to meet renal epithelial cell needs [30]. The device culture membrane was sterilized by exposure to UV light for 30 min on each side, and the rest of the system was sterilized by autoclave at 121 ºC for 15 min. Prior to cell seeding, membrane was coated with collagen type I 0.4 mg mL^{-1}, 50 µg cm^{-2} (100 µL per channel) in phosphate-buffered saline (PBS), incubated at 37 ºC for 1 h, and rinsed three times with PBS. Cells were seeded on each culture area of the membrane at a concentration of ~40.000 cells per channel in 300 µL complete culture medium and maintained inside a Petri dish for 2 h until cell attachment. In experiments involving both cell lines, NRK-52E cells were seeded on one of the three cell culture areas of the membrane, while raTAL cells were seeded on the other two ones. Then, unattached cells were carefully aspirated, and the Petri dish was filled with culture medium and maintained at 37 ºC and 5 % CO_2, refreshing culture medium every 2–3 days. Cells typically reached confluence after 2 days. On day 4–5, membrane and plates were assembled to expose the cells to flow perfusion and to perform EIS (Figure 4-2). On coverslips, cells formed an efficient barrier at the 3rd day post-confluence as revealed by ZO-1 expression (Figure 4-3)

Epithelial monolayers were confirmed by means of phase-contrast microscopy and a Ca^{2+} switch protocol. In the latter procedure, the culture medium in the chamber was replaced with medium containing 1 mM of ethylenediaminetetraacetic acid (EDTA) and without $CaCl_2$. After maintaining the cells under these conditions for 12 min, the medium in the chamber was returned to the normal culture medium that includes 1 mM of $CaCl_2$.

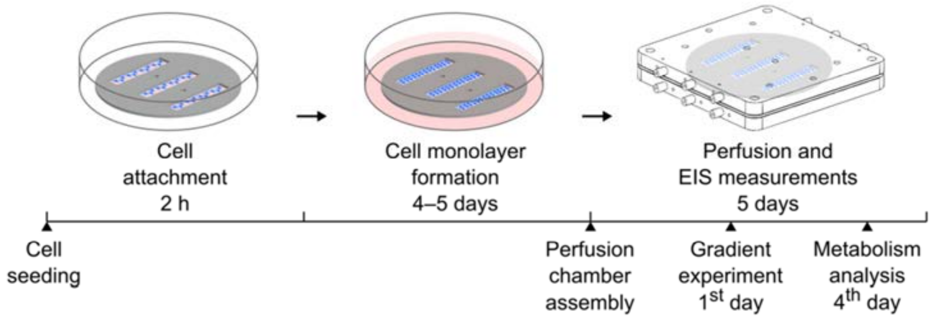

Figure 4-2 Experimental set-up procedure including cell seeding and attachment on the membrane (2 h), cell proliferation (4–5 days), and perfusion chamber assembly.

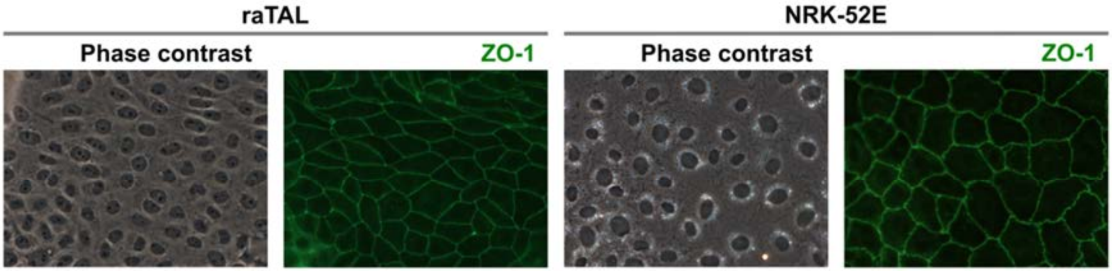

Figure 4-3 Phase-contrast images and ZO-1 expression at the 3rd day post-confluence for NRK-52E and raTAL cells plated on coverslips.

4.2.3 | Fluid shear stress

Fluid shear stress (FSS) in a channel of infinite parallel plates can be calculated as

$$\tau = \frac{6\mu Q}{wh^2} \tag{4-1}$$

where h is the height of the channel, w is the width of the channel, Q is the flow rate, and μ is the fluid viscosity. According to equation (4-1) and for a particular flow rate of 0.2 mL min^{-1}, the FSS exerted over the cells in our device was 0.07 dyn cm^{-2}.

To prevent cells from being exposed to flow perturbations at the inlet and outlet, the culture area was located in the centre of the compartment and separated from the ends 2.5 mm. We used the finite element method to study the distribution of the FSS along the cell culture area (Figure 4-4). Navier-Stokes and continuity equations were solved for a laminar flow in the stationary domain using COMSOL Multiphysics version 5.0 and its Fluid flow module.

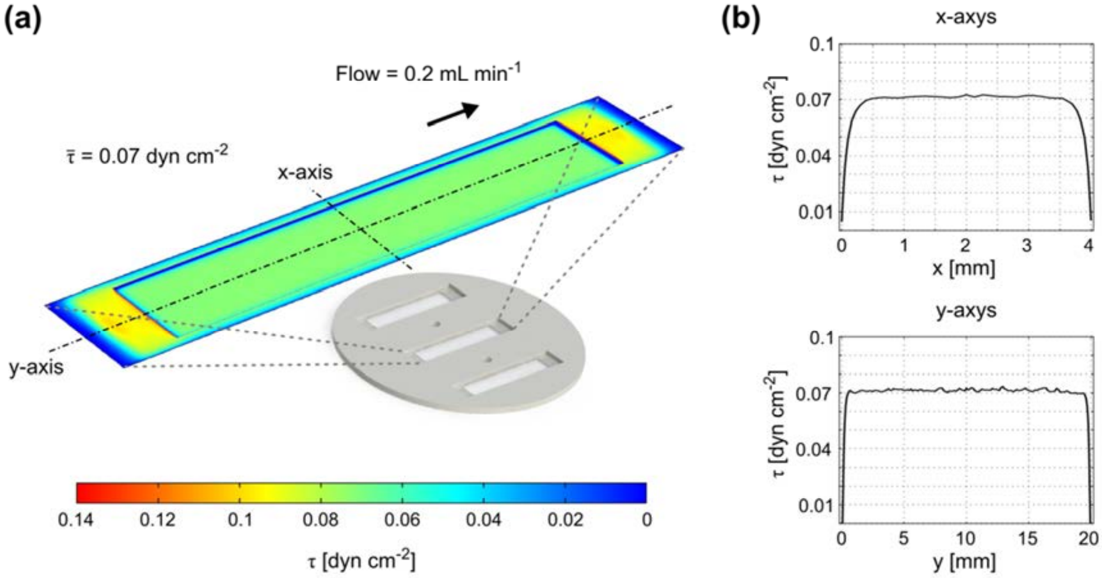

Figure 4-4 FSS (τ) distribution for a laminar flow of 0.2 mL min^{-1}. The average FSS for the whole cell culture area was 0.07 dyn cm^{-2}. (a) Plot representation of the bottom surface of the fluidic channel, in which the inner rectangle is the cell culture area. Outside the cell culture area there is a non-permeable PET surface that belongs to the PSA. (b) Charts of the FSS profile along the x and y axis.

4.2.4 | Fluidic set-up and experimental design

Compartments of the device were fluidically connected using silicone tubing (0.8 mm in internal diameter [ID] and 2.4 mm in outer diameter [OD]) as depicted in Figure 4-1d. Apical and basal compartments were perfused with independent fluidic circuits using two reservoirs and a peristaltic pump (Reglo ICC, Cole-Parmer GmbH, Wertheim, DE). The volume of the culture medium for apical and basal circuits was replaced every 4 days (10 mL for each). Three-way stopcocks were placed at the inlets and outlets of each compartment to provide a way to collect samples after experiments with static conditions. Culture medium samples from the reservoir or collected from the compartments were analysed for glucose, lactate, and ion concentrations using an automated analyser (AU680 Chemistry Analyzer, Beckman Coulter Inc., Brea, CA).

After assembling the membrane in the device, cells were apically and basally perfused with culture medium at a flow rate of 0.2 mL min^{-1} (FSS of 0.07 dyn cm^{-2}, Figure 4-4) during 1 day to stabilize the cells exposed to flow before each experiment. Apical and basal fluids were flowed in the same direction, and effluxes were recirculated. With this fluidic set-up, the NaCl chemical gradient is expected to reach a steady state in which the NaCl absorption (apical to basal) is equal to the NaCl backflow (basal to apical).

Figure 4-5 Experimental setup including assembly of the perfusion chamber in the top-right corner.

4.2.5 | Imposed transepithelial NaCl chemical gradient

To validate the measurement system to provide an estimate of NaCl concentration, an experiment was performed imposing different apical to basal chemical gradients for Na^+ and Cl^-. This strategy allowed the assessment of the transepithelial ion transport as well as the monitoring of the transepithelial electrical parameters under different ion gradients. First, culture mediums were replaced by Ringer's solutions and left for stabilization for 1 to 2 h. Standard Ringer's solution was composed of (in mM) 140 NaCl, 4 KCl, 1 $MgCl_2$, 1 $CaCl_2$, 5 Glucose, 10 Hepes, and pH 7.4. Then, one of the solutions bathing the apical or basal compartments was replaced by a modified Ringer's solution containing 70 mM of NaCl (substituted isoosmotically with N-Methyl-Glucamine (NMG)/gluconate), and flow was stopped to avoid any further diffusion from the compartments. Meanwhile, the opposite compartment was still perfused with standard Ringer's solution (140 mM NaCl). All solutions were allowed to equilibrate to incubator conditions before being used in the fluidic circuit.

4.2.6 | Electrical conductivity and ionic species

The electrical conductivity (k) of an electrolyte solution is given by

$$k = \Lambda_m c, \tag{4-2}$$

where Λ_m is the molar conductivity and c is the molar concentration [31]. According to the Kohlrausch's law of independent migration of ions, each ionic species contributes to the conductivity independently of other ions, particularly at infinite dilution ($c \rightarrow 0$). Then, Λ_m can be defined as the sum of all ionic conductivities:

$$\Lambda_m = \sum_i \lambda_i \tag{4-3}$$

in which λ_i is the ionic conductivity of a particular species i. Since ions contribute differently to the overall conductivity, it is interesting to quantify the particular contribution of each ion. The fraction of the conductivity of a given ion i is called its transport number (t_i), and it is calculated as

$$t_i = \frac{c_i \lambda_i}{\sum_i c_i \lambda_i}, \tag{4-4}$$

where c_i is the molar concentration of i-ions. For strong electrolytes where solutes almost completely dissociates in solution, λ_i is equal to the limiting molar conductivity (λ_i^0) at infinite dilution and decreases linearly with the square root of the concentration. Contributions of each compound in the Ringer's solution to the conductivity are shown as supplementary information in Table 3-1 for the approximation of infinite dilution. Although there are several salts in the solution, conductivity is dominated by the NaCl pair due to the high difference in concentrations. This is evidenced by a t_{NaCl} close to 1 and a t_i close to 0 for the rest (t_{NaCl} = 0.94 (140 mM NaCl); t_{NaCl} = 0.89 (70 mM NaCl); t_{NaCl} = 0.66 (70 mM NaCl + 70 mM NMG-gluconate)). In this scenario, it is possible to estimate NaCl concentration from conductivity measurements, especially if the concentrations of the other salts remain constant.

Table 4-1 Contribution of each salt to the conductivity of Ringer's solution. Data is calculated using the limiting molar conductivities at infinite dilution and 25 ºC [32, 33]. Note that each contribution column (t_i) is for a Ringer's solution containing (in mM) 140 NaCl, 70 NaCl, or 70 NaCl plus 70 NMG-gluconate. NMG, N-Methyl-Glucamine.

Compound	λ_i^0 [S cm^2 mol^{-1}]	c_i [mM]	t_i (140 mM NaCl)	t_i (70 mM NaCl)	t_i (70 mM NaCl) + (70 mM NMG-gluc.)
NaCl	$\lambda^0_{Na^+} + \lambda^0_{Cl^-}$ = 50.1 + 76.3 = 126.4	140	0.940	-	-
		70	-	0.887	0.661
KCl	$\lambda^0_{K^+} + \lambda^0_{Cl^-}$ = 73.5 + 76.3 = 149.8	4	0.032	0.060	0.045
$CaCl_2$	$\lambda^0_{Ca^{2+}} + 2\lambda^0_{Cl^-}$ = 118.9 + 152.6 = 271.5	1	0.014	0.027	0.020
$MgCl_2$	$\lambda^0_{Mg^{2+}} + 2\lambda^0_{Cl^-}$ = 106 + 152.6 = 258.6	1	0.014	0.026	0.019
NMG-gluconate	$\lambda^0_{NMG^+} + \lambda^0_{gluc.^-}$ = 24.1 + 24.5 = 48.6	70	-	-	0.254

The electrical conductivity of an electrolyte solution can be measured using a pair of electrodes exposed to the solution according to the following equation:

$$k = K_{cell}\, G, \tag{4-5}$$

where G is the electrical conductance measured between the pair of electrodes and K_{cell} is the cell constant, which depends of the geometry of the electrodes. This methodology is simple and fast, and many commercially available conductivity meters employ this principle to measure the k of electrolytic solutions (e.g., EC-Meter GLP 31, Crison Instruments SA, Barcelona, ES).

Electrical conductances of apical and basal solutions were measured at the perfusion chamber to estimate their NaCl concentrations in real time. Having the cell constant of the electrodes invariable, the conductivity will be proportional to the conductance and their variations in percentage equal. In accordance with this assumption, a small change in the cell constant of the electrodes would account for slight measurement differences. In addition, other ion species and temperature are factors that will affect electrical conductance. The former can be neglected under certain conditions where the conductivity is dominated by only one type of ion, while the latter can be solved performing measurements at same temperature conditions.

4.2.7 | Impedance analysis

Simultaneous measurements of transepithelial electrical parameters and solution conductances were managed by changing the electrical connections between the device and an impedance analyser [34]. This switching was performed automatically with a custom-made relay multiplexer device. Both electrical connections are shown in Figure 4-6.

Impedance measurements across an epithelial monolayer can be interpreted in terms of its electrical properties by the equivalent electric circuit shown in Figure 4-6a. This is a simplified model with lumped elements and consists of the resistance of the medium solution (including the medium resistance through the pores of the semipermeable membrane) (R_s) in series with the parallel of TEER and C_{cl}. These parameters were obtained by impedance analysis using EIS. Impedance spectra were measured at 20 frequencies, ranging from 10 Hz to 1 MHz, and each measurement was fitted to the equivalent electric circuit using the least-squares method in Matlab. For measuring apical or basal conductances, impedances were measured between the two apical (in the upper plate) or the two basal (in the lower plate) IDE, respectively. Then, impedance data was fitted to the equivalent electric circuit consisting of the conductance of the medium solution (G) in series with a CPE representing the electrode polarization impedances (CPE_e) (Figure 4-6b).

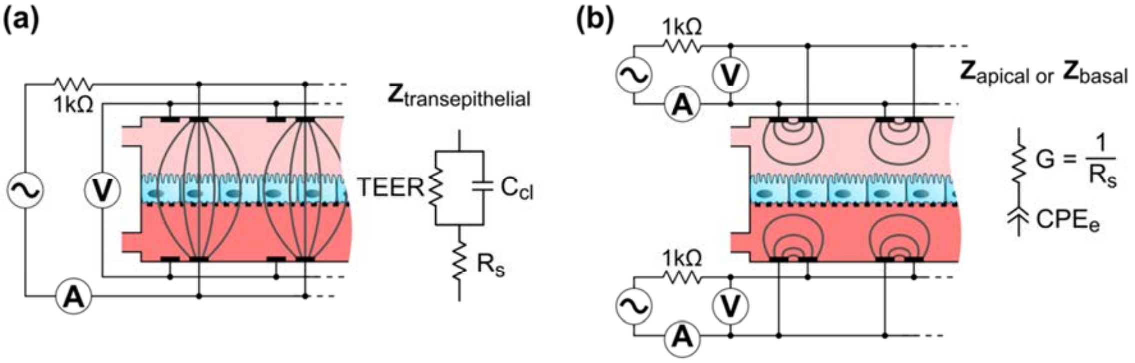

Figure 4-6 Schematic representation of the measurement system. Electrical connections between the device and the impedance analyzer for measuring (a) transepithelial electrical impedance, (b) apical conductance, and basal conductance. There are included the equivalent electric circuits with lumped elements. For transepithelial impedance, this consists in the resistance of the medium solution (R_s) in series with the parallel of TEER and C_{cl}. For apical and basal impedances, this consists of the conductance of the medium solution (G) in series with a constant phase element that represents the electrode polarization impedances (CPE_e). Note that it is not drawn to scale and is a section of the perfusion chamber. The resistance of 1 kΩ in series with the sine wave generator limits the maximum current applied to the cells, so the maximum applied voltage and current are 10 mV and 10 µA, respectively. V, voltmeter; A, ammeter; ~, sine wave voltage perturbations at different frequencies.

4.3 | RESULTS AND DISCUSSION

4.3.1 | Electrophysiological characterization of cells during long-term culture under flow

The fabricated chamber system was experimentally validated to electrophysiologically characterize renal cell monolayers under perfusion. First, the conditions for achieving rapid formation of a confluent cell monolayer were optimized. PET and PC porous membranes were evaluated as a support for forming NRK-52E and raTAL cell monolayer. Phase-contrast images of both cell types on PC or PET membranes are shown in Figure 4-7a. Cells growing on PET membrane reached confluence after 2 days and showed good standing of perfusion in the device. Otherwise, cells on PC membrane were able to attach and spread but not to fully proliferate on the whole membrane. Thus, best conditions were shown to be seeding NRK-52E or raTAL cells at high density on collagen type I-coated PET membranes; the rest of the experiments were done under these conditions. Once the membrane with the cells is assembled inside the bioreactor, monolayer integrity can be readily confirmed by microscopic inspection. Application of 0.2 mL min^{-1} flow rates to either one or both compartments supported long term survival (≥2 weeks) of both cell lines. With this flow rate, cells were subjected to a FSS of 0.07 dyn cm^{-2}. Although this FSS may not be physiologically relevant (the *in vivo* value is approximately 0.2 dyn cm^{-2}), perfusion served to continuously supply the cells with nutrients and gases (i.e., O_2 and CO_2) as well as to take away the waste.

Real-time, continuous TEER recording was used to assess cell monolayer health during long-term culture. This eliminates the need to remove the bioreactor (and the

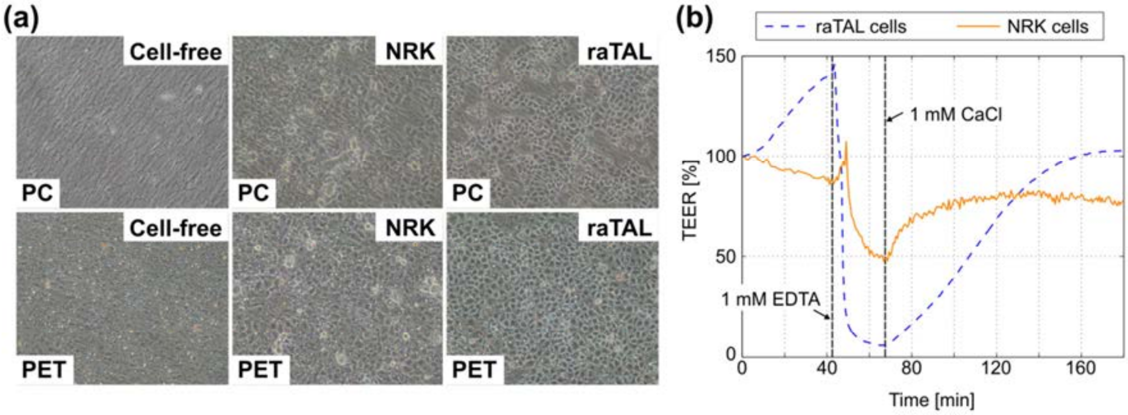

Figure 4-7 (a) Phase-contrast images of NRK-52E and raTAL cells growing on PC or PET membranes for TEER device. Cells were seeded at high density in 300 µL per channel and allowed to attach for 2 h before filling the dish with culture medium. Cells growing on PET reached confluence after 2 days and showed good standing of perfusion in the device. (b) Time course of the TEER during a Ca^{2+} switch protocol for raTAL (blue dashed line) and NRK-52E (orange line) cells. Arrows point the time of Ca^{2+} removal plus the administration of 1 mM of ethylenediaminetetraacetic acid (EDTA) and Ca^{2+} recovery plus EDTA removal.

perfusing circuit) from the incubator, which is a cumbersome manoeuvre, reducing the risk of bubble formation and avoiding abrupt changes in culture conditions that hinder conventional culture techniques. To confirm the formation of both epithelial monolayers and to demonstrate that TEER values were dependent on tight junction paracellular resistance, it was performed a Ca^{2+} switch protocol. This is a well-established method relying in the calcium-dependency of tight junction formation so that monolayers cultured in a low Ca^{2+} medium lack barrier formation [35].

During a Ca^{2+} switch (transition from a Ca^{2+} depleted medium to a normal Ca^{2+} medium), tight junctions reassemble in few hours. The time course of the TEER during a reduction and subsequent recovery of the Ca^{2+} concentration is shown in Figure 4-7b. TEER values of both NRK-52E and raTAL cells fell and rose according to Ca^{2+} reduction and recovery, respectively. Epithelial monolayer formed with NRK-52E cells exhibited a TEER of $9.1\pm0.4\ \Omega\ cm^2$ and a C_{cl} of $0.50\pm0.04\ \mu F\ cm^{-2}$ after being perfused for 1 day, while they were $600\pm80\ \Omega\ cm^2$ and $1.56\pm0.14\ \mu F\ cm^{-2}$ for raTAL cells. The perfusion chamber was found suitable to follow in real-time the assembly and disassembly of intercellular junctions. Representative impedance spectra during the assembly and disassembly of intercellular junctions are shown in Figure 4-8.

Impedance spectra measured through both cell layers (Figure 4-9a and Figure 4-9a) and time course of TEER and C_{cl} in raTAL cells under different flow conditions are shown in Figure 4-10. Flow in the basal compartment not only supplies cells with continuous nutrients at the basolateral side, as occurs *in vivo*, but also helps to remove the waste and to maintain a constant concentration of solutes—an issue that most microfluidic cell cultures fail to reproduce.

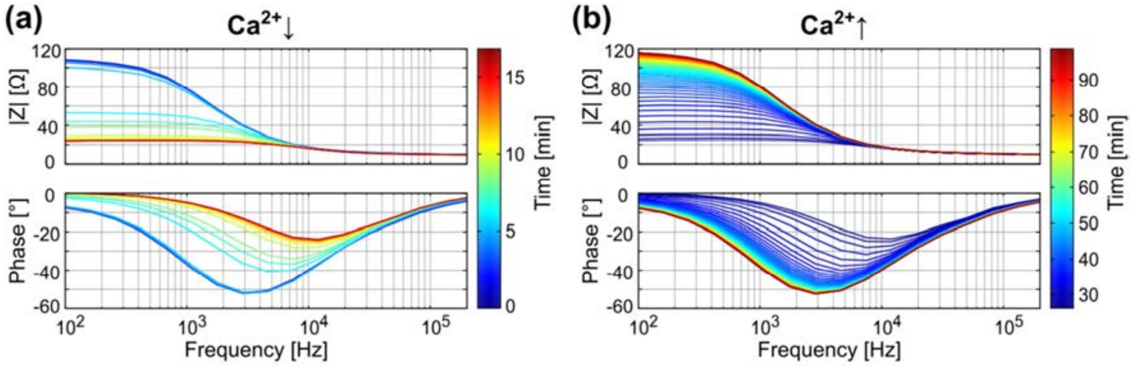

Figure 4-8 Representative impedance spectra during (a) assembly and disassembly of the intercellular junctions in a Ca2+ switch protocol. Data was acquired every minute

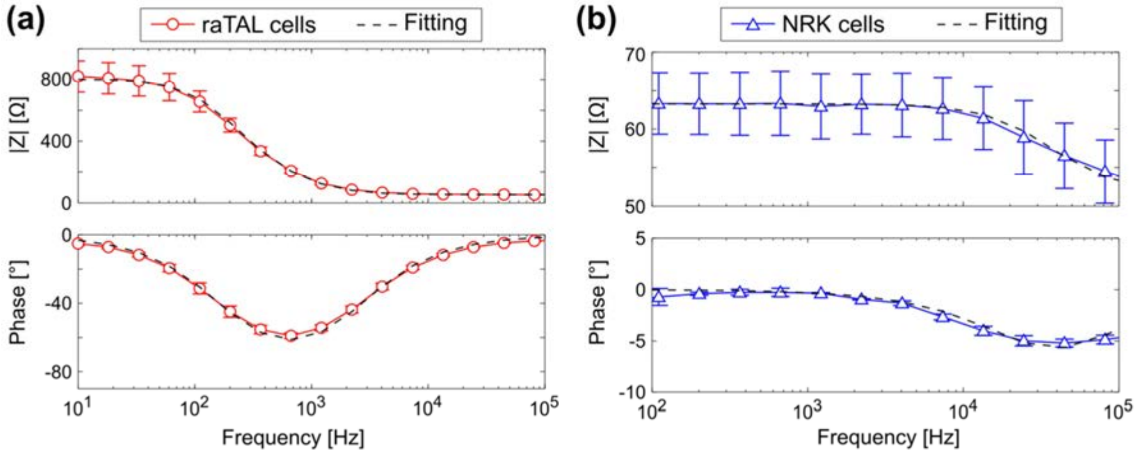

Figure 4-9 Bode representation of the transepithelial impedance measured before gradient experiments. In particular, they were taken after the cells were perfused for 1 day in the system at a flow rate of 0.2 mL min^{-2} (raTAL cells, n = 6; NRK cells, n = 3).

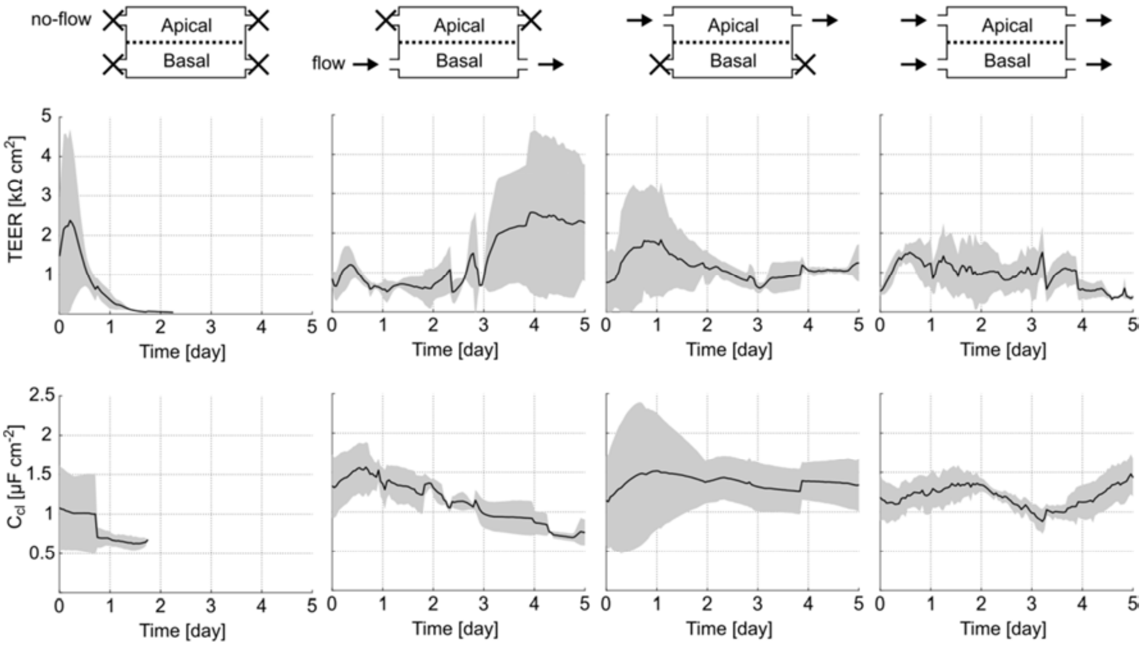

Figure 4-10 Electrophysiological characterization of raTAL cells under different flow conditions. From the left to the right, different conditions include no-flow, basal perfusion, apical perfusion, and apical and basal perfusion (at a constant flow rate of 0.2 mL min^{-1}). Time course of TEER and C_{cl} are shown for 5 days under each condition (n=3 except for apical and basal perfusion, n=9). Measurements started 4–5 days after the cells were plated on the membrane; cells were kept in static conditions during this time. Then, cell monolayers were maintained with apical and basal perfusion, apical perfusion, and even with only basal perfusion for an additional 5 days. In absence of flow, cells died in 1 day. Note that the semipermeable membrane is located between the basal flow and the basolateral cell membrane. Interestingly, time course of TEER and C_{cl} were distinct among conditions (e.g., TEER was lower during apical perfusion than in basal perfusion, and C_{cl} decreased in basal perfusion).

Samples of medium perfusate were analysed to determine several metabolic parameters. The metabolism of raTAL cells is summarized in Table 1.

Table 4-2 Metabolism of raTAL cells cultured in the device. These values were analysed from samples collected at the reservoirs after the cells were perfused in the bioreactor for 4 days (* $p<0.05$ by unpaired student's t-test) ($n=3$).

	Basal	Apical
Glucose flux (μmol h^{-1} cm^{-2})	0.054 ± 0.04	0.092 ± 0.051
Lactate flux (μmol h^{-1} cm^{-2})	0.048 ± 0.031*	0.100 ± 0.055*
$[Na^+]_o$ (mM)	152.3 ± 5.9*	147.5 ± 4.6*
$[K^+]_o$ (mM)	4.08 ± 0.82	4.44 ± 0.56
$[Cl^-]_o$ (mM)	138.2 ± 8.2	138.2 ± 8.2

Surprisingly, data shows that cells have polarized energy metabolism toward the apical site (preferred site to uptake glucose and dump lactate), the opposite to what could be expected *in vivo* in the original tissue. Although the origin of this abnormal polarization cannot be confirmed, this could be because continuous cell lines have been selected to thrive in 2D culture, where all metabolic exchange takes place through the apical membrane. Interestingly, it was detected Na^+ reabsorption in the perfusion chamber. There was a significant difference of Na^+ concentration; the concentration in the apical side was ~5 mM lower than in the basal side (~4 mM for Cl^-). This gradient, measured after 4 days in the perfusion chamber, corresponds to a net transport of NaCl of ~0.15 nmol cm^{-2} s^{-1}. Despite this is much lower than the transport in isolated perfused TAL segments (1–10 nmol cm^{-2} s^{-1}; rat, mouse, and rabbit) [36], it proves the existence of active mechanisms of Na^+ transport. The TAL is known as the diluting segment because it is able to reduce luminal NaCl concentrations up to 30 mM. This is achieved through the combination of active NaCl transepithelial transport and a very tight barrier that is water impermeable. Our findings confirm the high barrier formed by raTAL, but the magnitude of NaCl transport does not appear to be similar to that observed *in vivo*, most likely because we could not demonstrate expression of the major protein responsible for active transport (NKCC2) in these cells. In any case, this example illustrates the validity of the system to readily acquire valuable information about the renal epithelium health and function. Metabolic rates did not change significantly over the course of long-term culture.

4.3.2 | Electrical conductance and NaCl concentration

Renal epithelium *in vitro* should reproduce the *in vivo* function, which basically consists in reabsorbing large quantities of solutes and ions. Differences in ion selectivity and water permeability induce the formation of electrochemical transepithelial gradients, especially in the TAL. That led to propose using a different configuration of the TEER electrodes to determine medium conductance in both compartments (corresponding to apical and basolateral cell poles) and, in turn, to estimate NaCl transport and its potential active transport across the epithelium. Electrical characterization of the measurement system using different NaCl concentrations is shown in Figure 4-11a. To avoid the systematic error due to slightly variations in the cell constant of the electrodes placed at each compartment, conductance was normalized to the value measured at 140 mM of NaCl. The relation between variation in the conductance and the concentration of NaCl were linear at least for values lower than 140 mM (Figure 4-11b). For higher concentrations, it would be expected a lower variation of the conductance as the concentration rises because of an increasing ion interaction that decreases ion mobility. The maximum uncertainty in the percentage of conductance was ±0.93 %, which was equivalent to ±2.4 mM in the estimation of the NaCl. The measured Na$^+$ concentration gradient for raTAL cells cultured in the perfusion chamber was ~5 mM. As mentioned above, other ion species also influences conductance. In the range from 70 to 140 mM, the conductance of the Ringer's solution is dominated by the NaCl due to the high concentration and mobility of Na$^+$ and Cl$^-$ against other ions.

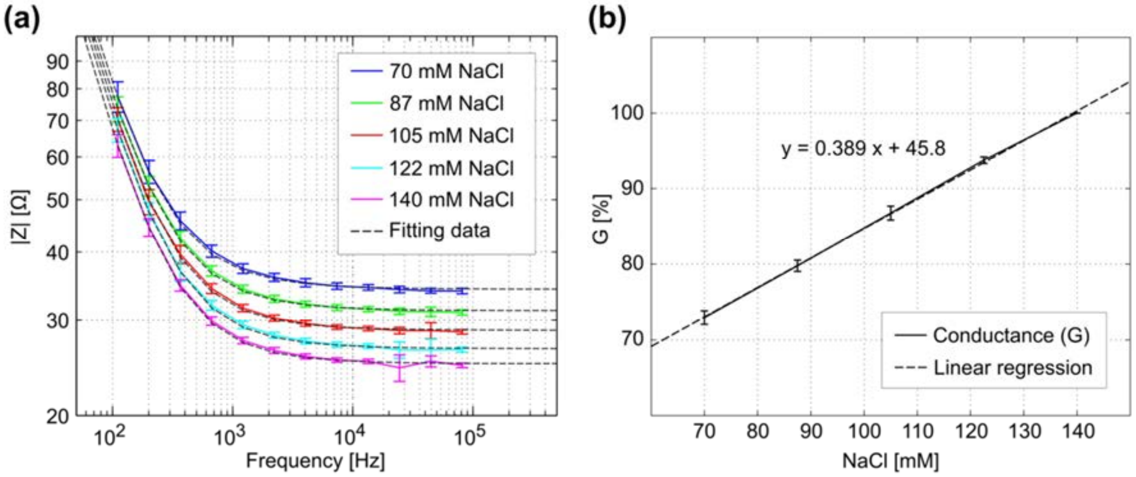

Figure 4-11 Electrical characterization of the estimation of NaCl through EIS. (a) Impedance spectra at different NaCl concentrations using a blank porous membrane. Chambers were filled with Ringer's solutions of 70 (blue line), 87.5 (green line), 105 (red line), 122.5 (cyan line), and 140 mM (magenta line) of NaCl, and impedance spectra were measured at 37 ºC and 12 frequencies, ranging from 100 Hz to 100 kHz. The fitting data according to the equivalent electric circuit is shown in dashed line. (b) Variation in conductance as a function of the NaCl concentration (solid line) and linear regression line (dashed line) (n = 6). Data is normalized to the conductance measured at 140 mM of NaCl (100 %).

An additional application of the in-line determination of ion concentrations is the estimation of water evaporation to maintain osmotic balance in cells. Cell culture incubators prevent water evaporation from cell cultures by direct water fill onto the bottom plate so the humidity is kept above 95 %. However, even a small humidity change may evaporate water causing an osmotic stress in cells. This could be solved by monitoring the ion concentration and then act accordingly refreshing the medium.

4.3.3 | Transepithelial transport of NaCl

Since raTAL epithelium in the chamber system did not exhibit the large active NaCl transport characteristic of native TAL (only a 5 mM NaCl gradient), it was designed an experiment (Figure 4-12a) to validate the conductance measurement system as a method to analyse the role of tight junctions in NaCl transepithelial transport in a renal cell monolayer. Instead of relying on active transport, artificial transepithelial NaCl gradients were imposed by replacing the medium in one of the compartments with an isoosmotic solution containing 70 mM NaCl, while keeping the opposite compartment in a standard Ringer's solution (140 mM NaCl). Thus, the electrochemical gradient lead to the movement of NaCl from the concentrated compartment toward the diluted one, whereas ion diffusion rates should be determined by the tightness of the epithelium.

Measurements of the conductance in both compartments allowed us to follow in real time the transepithelial transport of NaCl while measuring simultaneously transepithelial electrical parameters. Time course measurements of electrical conductance, NaCl concentration, TEER, and C_{cl} are shown in Figure 4-12 for epithelial monolayers obtained with NRK-52E and raTAL cells. Note that the y-axis of Figure 4-12b shows the NaCl concentration calculated through the linear regression line included in Figure 4-11b. Immediately after decreasing the NaCl concentration in basal (+ gradient experiment, apical NaCl > basal NaCl) or apical (- gradient experiment, apical NaCl < basal NaCl) compartments and stopping the flow, the recovery of NaCl concentration in the 70 mM compartment occurred driven by the electrochemical force between both comportments (Figure 4-12b). This rise was much faster for NRK-52E cells than for raTAL cells. NaCl concentrations of the 70mM compartment at 1 and 2.5 h are summarized in Figure 4-12c. In detail, NaCl concentrations after 2.5 h were 138 (+Grad.) and 129±2 mM (-Grad.) for NRK-52E cells, while concentration were 101±7 (+Grad.) and 80±5 mM (-Grad.) for raTAL cells. Otherwise, opposite compartments maintained 140 mM as expected from the continuous flow with the Ringer's solution (140 mM NaCl). Note that the porous membrane, where cells are cultured, partly contributes to maintain the concentration gradient. Therefore, there is a slow recovery of the gradient even with a very leaky epithelium, such as that formed by NRK-52E cells.

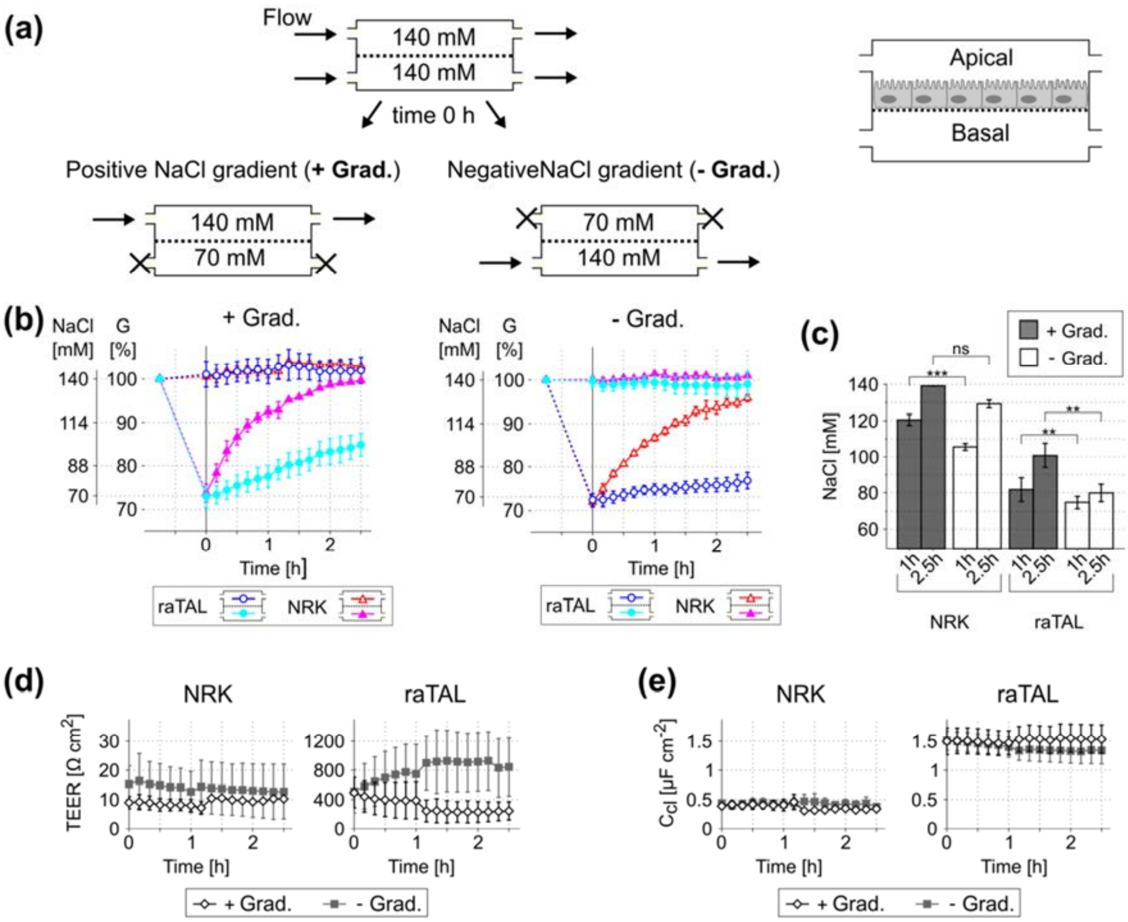

Figure 4-12 Time course of the NaCl concentration during imposed apical to basal positive (apical NaCl > basal NaCl) and negative (apical NaCl < basal NaCl) gradients. (a) Experimental procedure. At time 0, the apical or basal solution containing Ringer's solution of 140 mM of NaCl was replaced by one of 70 mM of NaCl, and the flow was stopped. The opposite compartment was still perfused with Ringer's solution of 140 mM of NaCl. (b) Time course of the electrical conductance at the apical (blue empty circles [raTAL] and red empty triangles [NRK-52E]) and basal (cyan filled circles [raTAL] and magenta filled triangles [NRK-52E]) compartments during positive and negative gradients in raTAL and NRK-52E cells (n=4 except for raTAL cells from 0 to 1h (n=11) and for NRK-52E cells from 1 to 2.5 h (n=1). Data was obtained from two (NRK-52E) and four (raTAL) independent experiments. Conductance was normalized to the data measured at 140 mM of NaCl (100 %), and the NaCl concentration was obtained by means of the linear regression line obtained in the electrical characterization. (c) Estimated NaCl concentration at 1 and 2.5 h after the imposed gradient in both cell types (ns $p>0.05$; ** $p<0.01$; *** $p<0.001$ by unpaired student's t-test). Time course of the (d) TEER and the (e) C_{cl} during positive (black empty diamonds) and negative (gray filled squares) gradients. TEER differences between positive and negative gradients were $p=0.90$ at 0 h; $p=0.39$ at 1 h; $p=0.29$ at 2.5 h.

The metabolic values of the main ionic species in the solution are shown in Table 4-3. For both cell types, cells had again polarized energy metabolism toward the apical site. Furthermore, there was a significant difference for the Na^+ and Cl^- concentration between NRK-52E and raTAL cells, which is in accordance with the results obtained by conductance measurements. However, such values were lower in the case of NRK-52E cells; it may be accounted for the medium contained in the tubes, which can be unbalanced with the medium in the compartment. This highlights the importance of in-line measurements since it is often difficult to collect samples from a specific place within microfluidic channels.

Table 4-3 Metabolic values during imposed NaCl chemical gradients. These values were analysed from samples collected at the compartment that was initially at 70 mM NaCl (1.5 h) (* $p<0.05$, apical vs basal; ‡ $p<0.05$, NRK-52E versus raTAL by unpaired student's t-test) (n=3).

	raTAL		NRK	
	Basal (+ grad.)	Apical (- grad.)	Basal (+ grad.)	Apical (- grad.)
Glucose (mg dL^{-1})	85.2±1.3	82.3±1.2*	94.3±4.0	85.0±2.0*
Lactate (mg dL^{-1})	0.15±0.08	2.65±1.1*	0.23±0.15	1.5±0.3*
$[Na^+]_o$ (mM)	84.7±1.6	82.0±6.6	91.0±3.6‡	90.5±0.5
$[K^+]_o$ (mM)	3.8±0.06	3.8±0.10	4.0±0.21	3.8±0.09
$[Cl^-]_o$ (mM)	88.4±1.6	88.4±3.9	96.8±1.7‡	96.7±0.9‡
$[Ca^{2+}]_o$ (mM)	3.6±0.06	3.7±0.04*	3.8±0.06	3.8±0.05
$[Mg^{2+}]_o$ (mM)	2.5±0.07	2.6±0.10	2.6±0.11	2.5±0.07

In the PT, Na^+ is absorbed through the Na^+/H^+ exchanger (NHE3) and the Na^+/glucose cotransporter in the apical membrane cooperating with the Na^+-K^+-ATPase and the Na^+/HCO_3^- cotransporter in the basolateral membrane. Concurrently, most of the Cl^- is reabsorbed paracellularly due to the generated electrochemical gradient, although Cl^- channels and Cl^--coupled transporters also contribute to Cl- reabsorption [37]. NRK-52E cell line is derived from PT and express Na^+/glucose cotransporter [38]. The epithelium of PT has low transepithelial resistance and is considered a "leaky" epithelium, in which the paracellular resistance is much lower than the transcellular resistance. This means that paracellular pathway is very permeable to ions and a chemical gradient will tend to equalize rapidly, as it happened in our experiments. *In vivo*, the PT achieves to maintain the reabsorbed Na^+ by the drag of water and Cl^- into the peritubular space because of osmosis and electrodiffusion, respectively; otherwise, Na+ would return to the filtrate [39]. On the other hand, raTAL cells were derived from the TAL—the initial segment in the distal nephron. In the TAL, the NaCl is transported into cells via the apical Na^+-K^+-$2Cl^-$ cotransporter (NKCC2), and Na^+ and Cl^- are secreted into the basolateral side through the Na^+-K^+-ATPase pump and the chloride channel Kb (ClC-Kb)/barttin channel, respectively. Both transport proteins, required for

Na^+ reabsorption (i.e., NKCC2 and Na^+-K^+-ATPase), have been detected in raTAL cells [29]. TAL is a tight epithelium and impermeable to water, being among the tighter epithelia in the human body. In such epithelia, the value of the paracellular resistance may be similar to transcellular one. This is an important requirement to efficient transepithelial transport since a leaky paracellular pathway that would allow for ion backflow would dissipate the chemical energy accumulated as NaCl transepithelial gradient, which is achieved through a secondary active transport through ATP consumption. Differences between time courses for passive transepithelial NaCl transport in NRK-52E and raTAL cells are in good agreement with what is expected from PT and TAL epithelia. Moreover, the NaCl transport was faster during positive gradients than during negative gradients for both cells.

In addition to the conductance, TEER (Figure 4-12d) and C_{cl} (Figure 4-12e) parameters were also measured during both gradient experiments by transepithelial impedance analysis. TEER values for NRK-52E cells at 2.5 h were 10.3 (+Grad.) and 12.7±9.3 $\Omega\,cm^2$ (-Grad.), which are in accordance with low values expected from the PT and with the literature for NRK-52E cells (12–13 $\Omega\,cm^2$) [40, 41]. For raTAL cells, TEER values were 245±123 (+Grad.) and 844±397 $\Omega\,cm^2$ (-Grad.). There are no reported values for this cell line, but TEER for freshly isolated rat medullary TAL tubules is one order of magnitude lower (7,722 Ω cm, corresponding to 48 $\Omega\,cm^2$ for lumen diameter of 20 μm) [42]. Interestingly, TEER of raTAL cells increased during the negative gradient and decreased during the positive gradient although not significantly. This means that ion permeabilities changed to be leakier during the positive gradient and vice versa, which may account for the faster NaCl transport along the positive gradient. The rate of NaCl reabsorption in the TAL segment is dynamic and depends on the luminal NaCl load, that is, cells ceases to reabsorb NaCl when the luminal NaCl concentrations is diluted and if the flow rate is very low, otherwise NaCl reabsorption increases [43]. Based on our results, we speculate that raTAL cells might sense ion concentrations on either side and adjust tight junction permeability accordingly. A leaky epithelia would contribute to reabsorb a positive gradient (avoiding salt waste from the body), whereas a tight epithelia would help to maintain the gradient achieved through active transport (which is the normal function *in vivo* for TAL cells). Unlike TEER, C_{cl} remained unchanged during gradient experiments suggesting that membrane surface areas were maintained. C_{cl} is a lumped element resulting from luminal and basolateral membrane capacitances in series. Its value is approximately 0.5 $\mu F\,cm^{-2}$ for cells with unfolded membranes and increases with the formation of complex surface morphologies. For tubular epithelial cells, which have very particular microvilli and cilium formations, C_{cl} is a useful parameter to electrically differentiate between cell types and to evidence tissue formation and persistence *in vitro*.

4.4 | CONCLUSIONS

Monitoring of transepithelial electrical parameters and simultaneous assessment of the ion concentration in real time has been achieved in the presented perfusion chamber using an innovative measurement approach. In particular, both methodologies can be easily combined with an appropriated electrode configuration in microfluidic cell cultures, as it is demonstrated in this work.

Here, the feasibility of this methodology for quantifying the concentration of NaCl has been presented. Therefore, it is possible the in-line and real-time monitoring of transcellular chemical gradient of NaCl produced by active transporters, which is a primary function of the renal tubule (NaCl reabsorption). In addition, it is essential to integrate sensing capabilities—similar to those of the Ussing chamber—in microphysiological systems that can apply FSS to study renal epithelial cells in a more physiological microenvironment.

4.5 | REFERENCES

[1] Lorenz JN. Micropuncture of the Kidney: A Primer on Techniques. In: Terjung R (ed) *Comprehensive Physiology*. Hoboken, NJ, USA: John Wiley & Sons, Inc., 2012, pp. 621–637.

[2] Burg MB, Green N. Function of the thick ascending limb of Henle's loop. *Am J Physiol* 1973; 224: 659–668.

[3] Muto S, Hata M, Taniguchi J, et al. Claudin-2–deficient mice are defective in the leaky and cation-selective paracellular permeability properties of renal proximal tubules. *Proc Natl Acad Sci* 2010; 107: 8011–8016.

[4] Stockand JD, Vallon V, Ortiz P. *In Vivo* and *Ex Vivo* Analysis of Tubule Function. In: Terjung R (ed) *Comprehensive Physiology*. Hoboken, NJ, USA: John Wiley & Sons, Inc., pp. 2495–2525.

[5] Furuse M, Furuse K, Sasaki H, et al. Conversion of *Zonulae Occludentes* from Tight to Leaky Strand Type by Introducing Claudin-2 into Madin-Darby Canine Kidney I Cells. *J Cell Biol* 2001; 153: 263–272.

[6] Li H, Sheppard DN, Hug MJ. Transepithelial electrical measurements with the Ussing chamber. *J Cyst Fibros* 2004; 3: 123–126.

[7] Ussing HH, Zerahn K. Active Transport of Sodium as the Source of Electric Current in the Short-circuited Isolated Frog Skin. *Acta Physiol Scand* 1951; 23: 110–127.

[8] Terryn S, Jouret F, Vandenabeele F, et al. A primary culture of mouse proximal tubular cells, established on collagen-coated membranes. *AJP Ren Physiol* 2007; 293: F476–F485.

[9] Yu ASL, Enck AH, Lencer WI, et al. Claudin-8 Expression in Madin-Darby Canine Kidney Cells Augments the Paracellular Barrier to Cation Permeation. *J Biol Chem* 2003; 278: 17350–17359.

[10] Ferrell N, Ricci KB, Groszek J, et al. Albumin handling by renal tubular epithelial cells in a microfluidic bioreactor. *Biotechnol Bioeng* 2012; 109: 797–803.

[11] Ha L, Jang K-J, Suh K-Y. Chapter 2. Kidney on a Chip. In: Berg A, Segerink L (eds) *RSC Nanoscience & Nanotechnology*. Cambridge: Royal Society of Chemistry, 2014, pp. 19–39.

[12] Jang K-J, Mehr AP, Hamilton GA, et al. Human kidney proximal tubule-on-a-chip for drug transport and nephrotoxicity assessment. *Integr Biol* 2013; 5: 1119–1129.

[13] Weinbaum S, Duan Y, Satlin LM, et al. Mechanotransduction in the renal tubule. *AJP Ren Physiol* 2010; 299: F1220–F1236.

[14] Benson K, Cramer S, Galla H-J. Impedance-based cell monitoring: barrier properties and beyond. *Fluids Barriers CNS* 2013; 10: 5.

[15] Clausen C, Lewis SA, Diamond JM. Impedance analysis of a tight epithelium using a distributed resistance model. *Biophys J* 1979; 26: 291–317.

[16] Cole KS. *Membranes, Ions and Impulses: A Chapter of Classical Biophysics*. Berkeley: University of California Press, 1972.

[17] Wang X-B, Huang Y, Gascoyne PRC, et al. Changes in Friend murine erythroleukaemia cell membranes during induced differentiation determined by electrorotation. *Biochim Biophys Acta BBA - Biomembr* 1994; 1193: 330–344.

[18] Wegener J, Abrams D, Willenbrink W, et al. Automated multi-well device to measure transepithelial electrical resistances under physiological conditions. *BioTechniques* 2004; 37: 590, 592–594, 596–597.

[19] Brakeman P, Miao S, Cheng J, et al. A modular microfluidic bioreactor with improved throughput for evaluation of polarized renal epithelial cells. *Biomicrofluidics* 2016; 10: 064106.

[20] Ferrell N, Desai RR, Fleischman AJ, et al. A microfluidic bioreactor with integrated transepithelial electrical resistance (TEER) measurement electrodes for evaluation of renal epithelial cells. *Biotechnol Bioeng* 2010; 107: 707–716.

[21] Curto VF, Marchiori B, Hama A, et al. Organic transistor platform with integrated microfluidics for in-line multi-parametric in vitro cell monitoring. *Microsyst Nanoeng* 2017; 3: 17028.

[22] Greger R. Physiology of Renal Sodium Transport. *Am J Med Sci* 2000; 319: 51–62.

[23] Duan Y, Weinstein AM, Weinbaum S, et al. Shear stress-induced changes of membrane transporter localization and expression in mouse proximal tubule cells. *Proc Natl Acad Sci* 2010; 107: 21860–21865.

[24] Mohammed SG, Arjona FJ, Latta F, et al. Fluid shear stress increases transepithelial transport of Ca^{2+} in ciliated distal convoluted and connecting tubule cells. *FASEB J* 2017; 31: 1796–1806.

[25] Raghavan V, Rbaibi Y, Pastor-Soler NM, et al. Shear stress-dependent regulation of apical endocytosis in renal proximal tubule cells mediated by primary cilia. *Proc Natl Acad Sci* 2014; 111: 8506–8511.

[26] Grabias BM, Konstantopoulos K. The physical basis of renal fibrosis: effects of altered hydrodynamic forces on kidney homeostasis. *AJP Ren Physiol* 2014; 306: F473–F485.

[27] Maggiorani D, Dissard R, Belloy M, et al. Shear Stress-Induced Alteration of Epithelial Organization in Human Renal Tubular Cells. *PLOS ONE* 2015; 10: e0131416.

[28] Gabriel G, Erill I, Caro J, et al. Manufacturing and full characterization of silicon carbide-based multi-sensor micro-probes for biomedical applications. *Microelectron J* 2007; 38: 406–415.

[29] Eng B, Mukhopadhyay S, Vio CP, et al. Characterization of a long-term rat mTAL cell line. *AJP Ren Physiol* 2007; 293: F1413–F1422.

[30] Taub M, Sato G. Growth of functional primary cultures of kidney epithelial cells in defined medium. *J Cell Physiol* 1980; 105: 369–378.

[31] Robbins J. *Ions in Solution 2: An Introduction to Electrochemistry*. Oxford: Oxford University Press, 1972.

[32] Haynes WM. *CRC Handbook of Chemistry and Physics, 95th Edition*. CRC Press, 2014.

[33] Ng B, Barry PH. The measurement of ionic conductivities and mobilities of certain less common organic ions needed for junction potential corrections in electrophysiology. *J Neurosci Methods* 1995; 56: 37–41.

[34] Guimerà A, Gabriel G, Parramon D, et al. Portable 4 Wire Bioimpedance Meter with Bluetooth Link. In: Dössel O, Schlegel WC, Magjarevic R (eds) *World Congress on Medical Physics and Biomedical Engineering*. Berlin: Springer, pp. 868–871.

[35] Gonzalez-Mariscal L, Contreras RG, Bolivar JJ, et al. Role of calcium in tight junction formation between epithelial cells. *Am J Physiol - Cell Physiol* 1990; 259: C978–C986.

[36] Burg MB. Thick ascending limb of Henle's loop. *Kidney Int* 1982; 22: 454–464.

[37] Planelles G. Chloride transport in the renal proximal tubule. *Pflüg Arch - Eur J Physiol* 2004; 448: 561–570.

[38] Dong X, Chen J, He Q, et al. Construction of bioartificial renal tubule assist device In Vitro and its function of transporting sodium and glucose. *J Huazhong Univ Sci Technolog Med Sci* 2009; 29: 517–521.

[39] Palmer LG, Schnermann J. Integrated Control of Na Transport along the Nephron. *Clin J Am Soc Nephrol* 2015; 10: 676–687.

[40] Limonciel A, Wilmes A, Aschauer L, et al. Oxidative stress induced by potassium bromate exposure results in altered tight junction protein expression in renal proximal tubule cells. *Arch Toxicol* 2012; 86: 1741–1751.

[41] Prozialeck WC, Edwards JR, Lamar PC, et al. Epithelial barrier characteristics and expression of cell adhesion molecules in proximal tubule-derived cell lines commonly used for in vitro toxicity studies. *Toxicol In Vitro* 2006; 20: 942–953.

[42] Monzon CM, Occhipinti R, Pignataro OP, et al. Nitric oxide reduces paracellular resistance in rat thick ascending limbs by increasing Na^+ and Cl^- permeabilities. *Am J Physiol-Ren Physiol* 2017; 312: F1035–F1043.

[43] Greger R. Ion transport mechanisms in thick ascending limb of Henle’s loop of mammalian nephron. *Physiol Rev* 1985; 65: 760–797.

5

A compartmentalized microfluidic chip for modelling the blood-retinal barrier

The interconnection of different tissue-tissue interfaces may extend organ-on-chips to a new generation of sophisticated models capable of recapitulating more complex organ-level functions. Single interfaces are largely recreated in organ-on-chips by culturing the cells on opposite sides of a porous membrane or by connecting the cells of two adjacent compartments through microchannels. However, it is difficult to interconnect more than one interface using these approaches. To address this challenge, it is presented a novel microfluidic device where cells are arranged in parallel compartments and are highly interconnected through a grid of microgrooves, which facilitates paracrine signalling and heterotypic cell-cell contact between multiple tissues. In addition, the device includes electrodes on the substrate for the measurement of TEER. Unlike conventional methods for measuring the TEER where electrodes are on each side of the cell barrier, a method with only electrodes on the substrate has been validated. As a proof-of-concept, the device was used to mimic the structure of the BRB by co-culturing primary human retinal endothelial cells (HREC), a human neuroblastoma cell line (SH-SY5Y), and a human retinal pigment epithelial cell line (ARPE-19). Cell barrier formations were assessed by a permeability assay, TEER measurements, and ZO-1 expression. These results validate the proposed microfluidic device with microgrooves as a promising in vitro tool for the compartmentalization and monitoring of barrier tissues.

Most of the contents of this chapter have been published in:

[1] **Yeste J**, García-Ramírez M, Illa X, Guimerà A, Hernández C, Simó R, Villa R. A compartmentalized microfluidic chip with crisscross microgrooves and electrophysiological electrodes for modeling the blood–retinal barrier. *Lab Chip* 2018; 18: 95–105

5.1 | INTRODUCTION

Organ-on-a-chip is an emerging technology addressed to reduce animal testing and accelerate clinical trials. Devices based on this technology enable an *in vitro* microenvironment and microarchitecture that closely mimics *in vivo* conditions [1, 2]. These factors stimulate a physiological response of the cells allowing the recapitulation of tissue- and organ-level functions. Organ-on-chips offer the advantage of accurately controlling the microenvironment of different cells by placing them in different compartments [3]. Therefore, each cell type can be exposed to particular mechanical and biochemical conditions. However, this separation is detrimental to heterotypic cell-cell interactions, especially when dealing with many different cells and compartments. In fact, to reproduce more than one tissue-tissue interface while maintaining a particular microenvironment for each cell type is a microengineering challenge.

Tissue-tissue interfaces in organ-on-chips have mimicked the interface between microvascular endothelium and brain parenchyma in the central nervous system [4] or the interface between the alveolar epithelium and the pulmonary microvascular endothelium in the lung [5], among others. A common strategy to simulate a tissue-tissue interface is by using membrane-based devices [5–8]. However, there are few works based on multi-layered membranes to deal with several interfaces [9]. Indeed, the stacking of porous membranes hampers the application of live cell imaging techniques. An alternative strategy is to use microchannels that link two adjacent compartments to permit side-by-side interconnections. Since compartments are arranged in parallel over a flat surface, these devices are suitable for real-time imaging of the whole cell culture. In addition, they are easy to fabricate and only requires the bonding of the PDMS slab once the mould is built. A disadvantage of this strategy is the small interface area, i.e., a barrier function model will be associated with the few cells occupying the entrance of the microchannels.

To reproduce more than one tissue-tissue interface in a single device, it was developed a novel microfluidic device where cells are arranged in parallel compartments but are highly interconnected through a grid of microgrooves under the cells (Figure 5-1), which facilitates paracrine signalling and heterotypic cell-cell contact between multiple tissues. Therefore, it is possible to build multiple interconnected interfaces maintaining a particular microenvironment for each tissue. The device comprises a PDMS slab that defines the compartments and a glass chip including a grid of microgrooves and metal electrodes. Its planar disposition facilitates real-time imaging and the integration of electrodes. In addition, permeability studies can be performed on epithelium and endothelium tissues covering the grid. Since the whole extent of the compartments is located on the grid, the measured permeability is representative of a large culture area unlike microchannel approaches.

Microfluidic cell culture devices are commonly built using microfabrication processes such as photolithography, deposition, and etching. With this technology it is also possible to integrate metal electrodes in such devices [10]. In fact, the presented microfluidic device includes metal electrodes on the glass substrate that permit the measurement of TEER. Several authors have developed different electrode configurations and strategies to measure TEER in microfluidic systems [11–14] and have integrated electrodes in microfluidic barrier models for its online monitoring [6, 7, 11–16]. Unlike methods aimed at measuring the TEER based on electrodes located on each side of the cell barrier, it is demonstrated in this chapter a method—also compatible with transport studies—that only requires electrodes to be on the basal side similar to the work of Sun *et al* [17]. Thus, TEER can be measured in multiple compartments avoiding the laborious task of integrating electrodes in the PDMS block. With the ECIS technology [18, 19], it is also possible to assess cell proliferation and barrier function using only electrodes in a substrate. However, ECIS systems lack a basal compartment since cells are attached to a surface that contains the electrodes. Thus, permeability and transport studies cannot be performed in such systems, which is a significant limitation in a barrier organ-on-a-chip system. In addition to the TEER measurement electrodes, the device includes an array of electrodes to be used in future applications for the recording of extracellular field potential. Recording electrodes allow evaluation of the electrical activity of neuronal tissues through local field potentials (LFPs) and extracellular action potentials (EAPs); additionally they could also be used to electrically stimulate neuronal activity [20].

To show the potential applicability of the structure of multi-compartments and microgrooves in organ-on–a-chip technology as well as its monitoring capabilities, the device was used to mimic the structure of the BRB, including both inner and outer barriers (Figure 5-1a). *In vitro* models that faithfully recapitulate the BRB are of great interest since its failure leads to the accumulation of fluid in the area of the retina of the

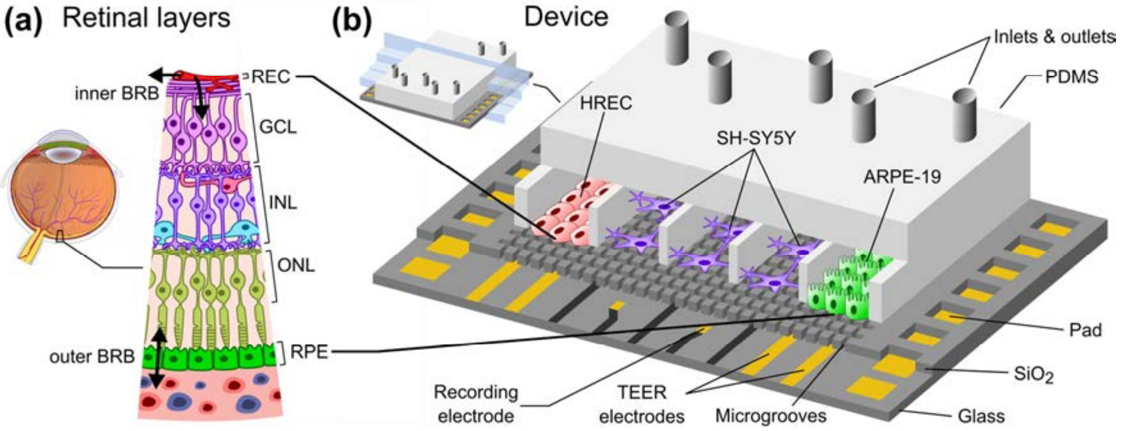

Figure 5-1 Recapitulating the cell structure of the retina. (a) Cell layers of the retina. From the anterior part of the retina to the posterior part of the retina: retinal endothelial cells (REC), ganglion cell layer (GCL), inner nuclear layer (INL), outer nuclear layer (ONL), and retinal pigment epithelium (RPE). Double arrows indicate the transport crossing the inner and outer BRB. (b) Schematic representation of the presented microfluidic cell culture device, including cells arrangement used in the experimental setup. Endothelial (HREC) and epithelial (ARPE-19) cells are located at the end compartments where there are TEER measurements electrodes, and SH-SY5Y cells are located in the middle compartments where there are extracellular potential recording electrodes

highest visual acuity (macula oedema) [21]. This occurs in early stages of diabetic retinopathy (DR) and in particular diabetic macular oedema (DME), which are common complications of diabetes that remain the leading causes of blindness in working-age populations in developed countries [22].

To validate the herein proposed microfluidic device, it was developed a co-culture of primary human retinal endothelial cells (HREC), the human neuroblastoma cell line (SH-SY5Y), and the human retinal pigment epithelial cell line (ARPE-19). The formation of endothelial and epithelial barriers was assessed by a permeability assay, TEER measurements, and ZO-1 expression. With this compartmentalization approach, it is possible to expose the endothelium to flow-induced shear stress, and the neuronal tissue can be subjected to a particular damage in order to evaluate the neurovascular coupling. In addition, it is possible to examine not only the particular response of one isolate type of cell in front to several stimuli but also its repercussion on the other retinal cell types, thus reproducing what really happens in the human retina.

5.2 | MATERIALS AND METHODS

5.2.1 | Microfluidic device design

The microfluidic device is structured in side-to-side compartments that are interconnected through a grid of microgrooves. It comprises a PDMS slab containing 7 compartments and a glass chip with microgrooves and electrodes for TEER measurements and recording of extracellular field potential. The compartments are 500 µm in width, 230 µm in height, and spaced by 50 µm. Two arrays of perpendicular microgrooves are etched in the glass and arranged in an area of 4 x 4 mm in the middle of the chip. Microgrooves are 2 µm in width, 4 µm in depth, and spaced by 10 µm. The total dimensions of the device are 22 x 22 x 4 mm.

Platinum electrodes are located at the bottom of the microgrooves. The three compartments in the middle have an array of 24 recording electrodes regularly distributed. The area of each electrode is 50 x 50 µm, although the effective area that is exposed to the surface is 30 x 30 µm due to the microgrooves. Each of the other two compartments at both ends has a pair of straight electrodes of 40 µm in width and 4 mm in length (effective area of 0.58×10^{-3} cm^2) to measure the TEER. All electrodes have accessible pads at the edges of the chip. A custom-made holder with spring contacts enables the electrical connection between the chip and an impedance analyser, thereby facilitating the assembly. Figure 5-2 shows a microscopy image with the layout of the electrodes on the glass chip.

5.2.2 | Microfluidic device fabrication

The building of the device was divided into three steps: 1) fabrication of the glass chip with microgrooves and electrodes, 2) replica moulding to make the PDMS slab with compartments, and 3) the final alignment and bonding of these two parts.

5.2.2.1 | Glass chip fabrication

The fabrication process of the glass chip containing the microgrooves and the electrodes is shown in Figure 5-3a (steps 1-14). A 4-inch borosilicate glass wafer (Borofloat, Praezisions Glas & Optik GmbH, DE) of 0.5 mm thickness was cleaned in a standard RCA bath. To define metal electrodes, a Ti/Pt/Ti (10, 150, and 10 nm) multilayer was e-beam evaporated (Oerlikon Univex 450B) and patterned by a standard lift-off process using 1.5-µm-thick image reversal photoresist (AZ5214E, Clariant GmbH, DE) (steps 2-5). These Ti layers were respectively used to improve the adhesion of the Pt to the glass substrate and the SiO2 deposited thereon. Layers of SiO2 (3.5 µm) and amorphous silicon (a-Si) (300 nm) were subsequently deposited on the wafer by plasma-enhanced chemical vapour deposition (PECVD) in an Oxford IPT Plasmalab 800 Plus (Oxford Instruments, UK). The SiO2 layer was used to create the microgrooves in a further step and was the surface where the cells were cultured, while a-Si was used to passivate the tracks of the recording electrodes by retarding the etching of the microgrooves over these tracks.

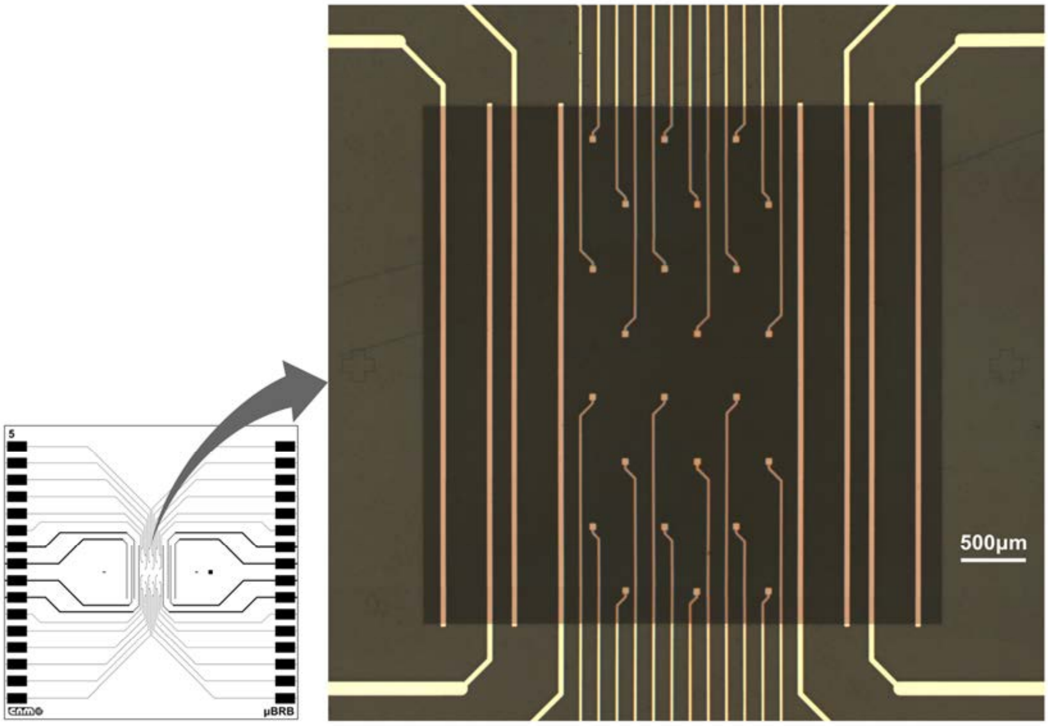

Figure 5-2 Microscopy image of the glass chip. The image shows the central area of the chip including the grid of microgrooves, straight electrodes for TEER measurement, and microelectrode array for the recording of extracellular field potential.

A standard photolithography process using 1.2-µm-thick positive photoresist (HIPR 6512 Fujifilm Electronic Materials, US) was performed to define the passivation layer (steps 8, 9). The a-Si layer was etched using a deep reactive ion etching (DRIE) process (Alcatel AMS-110DE), and the remaining photoresist was stripped using O_2 plasma (TEPLA 300-E, Technics Plasma, US) (step 10). Microgrooves were defined using the µgrooves & pad level photomask in a second standard photolithography procedure (steps 11, 12) and etched using a DRIE process (steps 13, 14). The etch profile resulted in two levels because of the patterned a-Si layer: the one that reached the surface of the platinum layer (4 µm in depth), and a second one (2.5 µm in depth) that insulated the metal tracks of the recording electrodes. Finally, the wafer was then cut into chips of 22 x 22 mm, obtaining 9 chips per wafer.

To decrease the electrode polarization impedance of the TEER and recording electrodes, these were electrochemically coated with a layer of platinum black [23]. Details about platinization are provided in Figure 5-4. In addition, apart from their use in future applications, the recording electrodes were electrically characterized by measuring a simulated signal of 10 Hz ranging from 10 to 1000 µVp (Figure 5-5). The impedance of the recording electrodes was 10 kΩ at 1 kHz, and the obtained average noise was lower than 5 µVrms.

5.2.2.2 | PDMS slab fabrication

The PDMS slab with the compartments was fabricated by a standard replica moulding process using a SU-8 mould (Figure 5-3b). This mould was fabricated on a clean silicon wafer where SiO2 was previously grown by a thermal process. There, SU-8 2005 photoresist (MicroChem Corp., US) was spin-coated, baked, and UV-exposed to form a seed layer of 5 µm thickness. This SU-8 surface was then activated using O2 plasma before spin-coating and baking a thicker layer of SU-8 2050. The different compartments were defined using an emulsion film mask (JD Photo Tools, UK) during UV-exposure. A second baking step was performed before developing the wafer and baking again at 120 °C for 30 min, resulting in a 230 µm thick layer.

The PDMS prepolymer (Sylgard 184, Dow corning Europe SA, BE) was prepared in a ratio of 10:1 (base: curing agent, w/w) and degassed in a vacuum desiccator. The prepolymer was cast on a Petri dish containing the SU-8 mould and left on a flat surface for 15 min. The PDMS was cured at 75 °C for 2 h and left overnight at room temperature (step 16). The PDMS was then peeled off from the mould, and pieces of 17 x 22 mm were cut and punched for fluid access (step 17). The resulting height of the compartments was 230 µm, and the thickness of the PDMS slab was 4 mm.

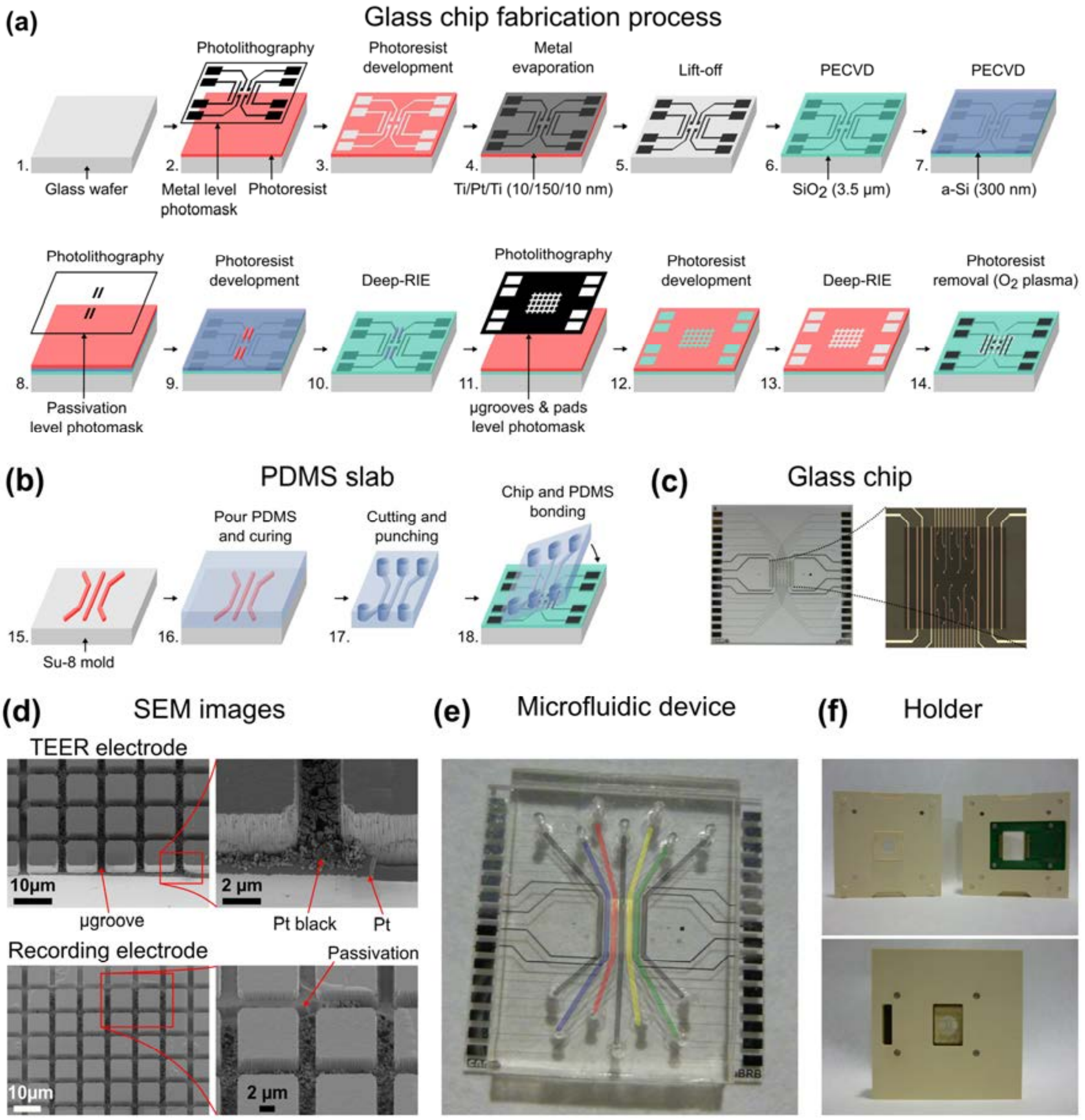

Figure 5-3 Microfluidic device fabrication process. (a) Fabrication steps of the glass chip. Proceeding from the beginning to the end are the photolithography process with the metal level photomask, Ti/Pt/Ti (10/150/10 nm) evaporation, lift-off process, plasma enhanced chemical vapor deposition (PECVD) of silicon dioxide (SiO2) (3.5 µm), PECVD of amorphous silicon (a-Si) (300 nm), photolithography process with the passivation level photomask, deep reactive-ion etching (deep-RIE) to etch the a-Si, photolithography process with the microgrooves and pad level photomask, and deep-RIE to etch the SiO2. (b) Fabrication steps of the PDMS stamp consisted of pouring a prepolymer PDMS on the SU-8 mold, curing of the PDMS, cutting of pieces, punching fluidic holes, and bonding of the PDMS slab with the glass chip. (c) Microscopy images of the glass chip, including an image of the central zone where the grid of microgrooves is located. (d) Scanning electron microscopy (SEM) images of the glass chip detailing the microgrooves and metal electrodes. (e) Full assembling of the device. Light color lines are superimposed on the image for clarity of the fluidic channels. (f) Custom-made holder to handle the device and to bring the electric pads into contact.

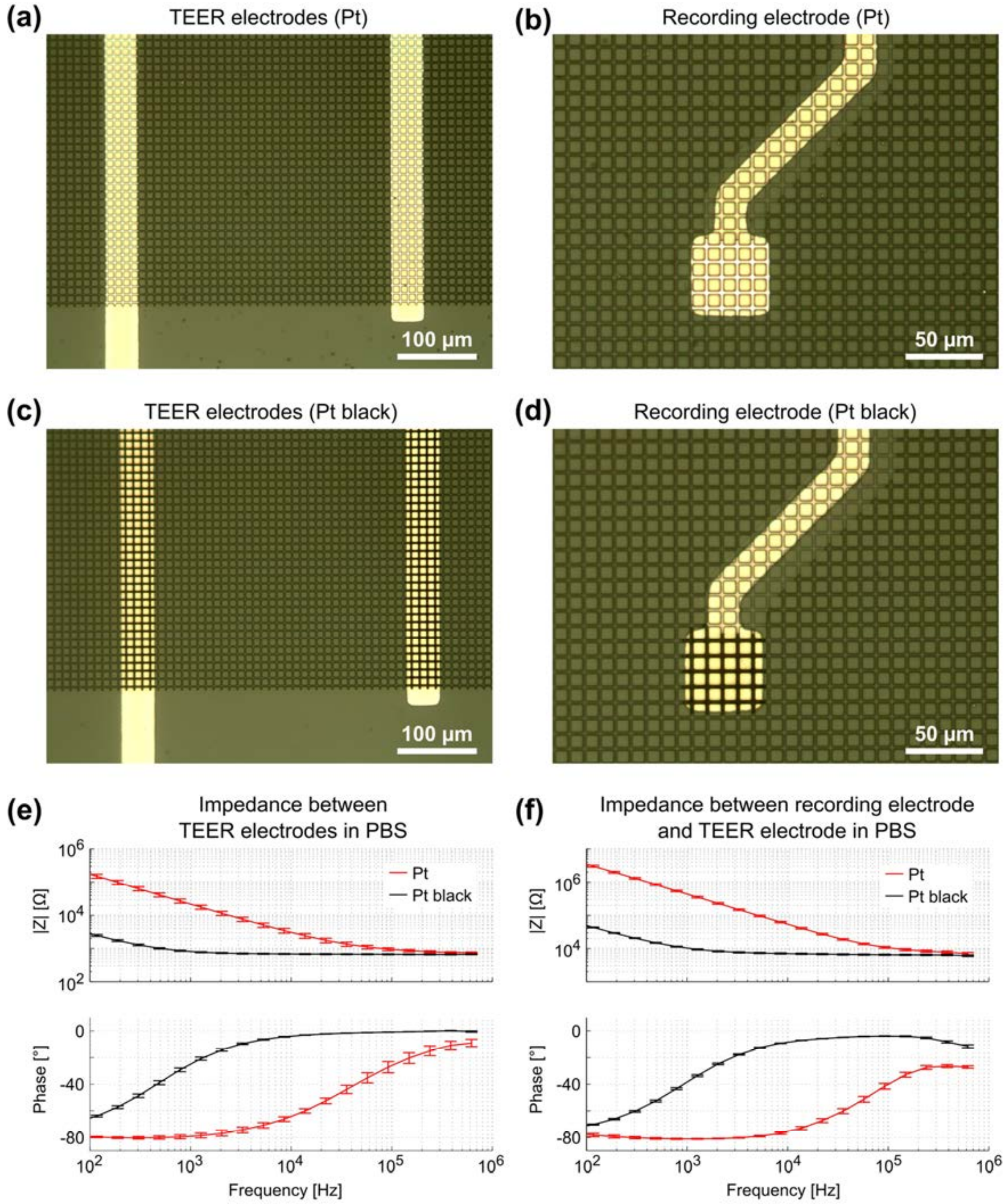

Figure 5-4 Electrochemical coating of platinum (Pt) black. (a–b) Microscope images of TEER and recording electrodes before platinization. (c–d) TEER and recording electrodes after being electrochemically coated with a layer of Pt black. Pt black was deposited by constant potential amperometry applying -0.2 V for 12.5 s on the electrodes against an Ag/AgCl reference electrode. (e–f) Impedance spectra measured between (e) TEER electrodes and between (f) a recording electrode and a TEER electrode in phosphate-buffered saline (PBS) (0.9 % NaCl, w/v) (n = 8).

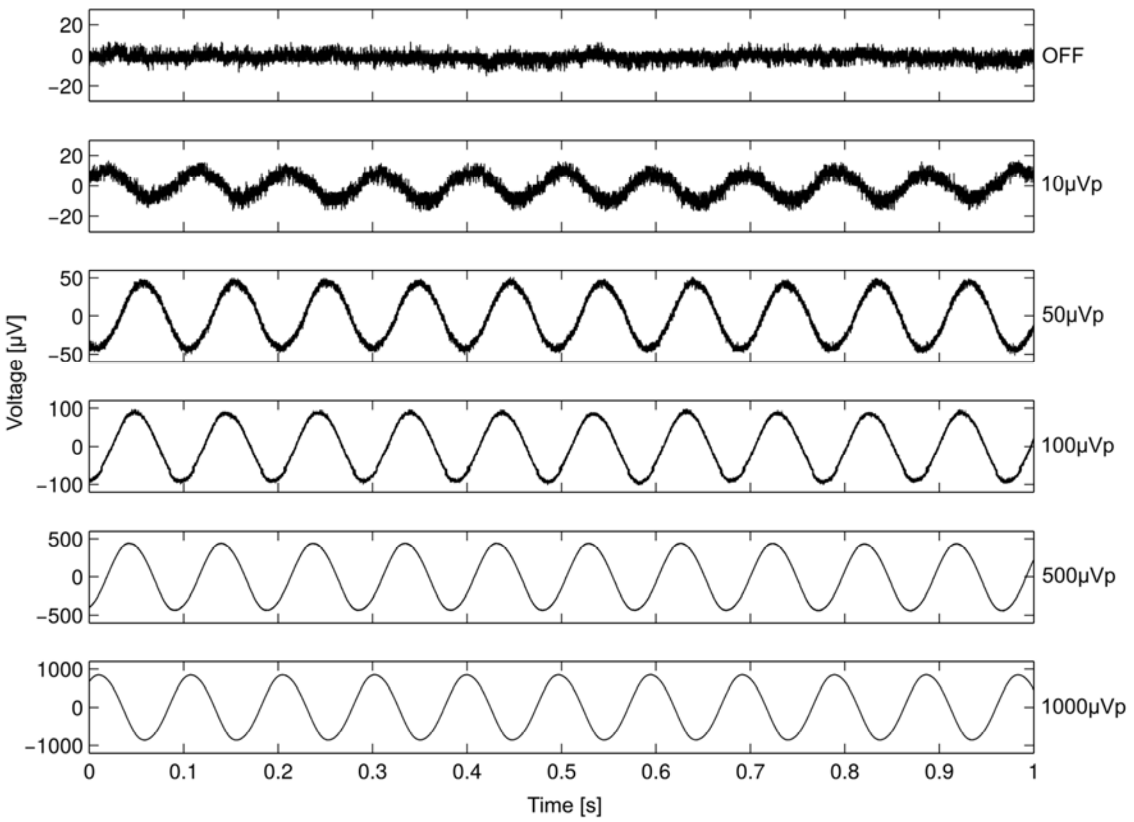

Figure 5-5 Validation of the electrodes for recording of extracellular field potential. Recording electrodes were validated by measuring a simulated signal of 10 Hz and 0, 10, 50, 100, 500, and 1000 µVp. This signal was generated with a sine wave generator (g.SIGgen, Guger Technologies OG, AT) and applied to the PBS solution through an external Pt wire electrode. Recording was made using an open-sourced tool for electrophysiology (Open Ephys, www.open-ephys.org). The average noise value for 24 electrodes of a a device was lower than 5 μV_{rms}.

5.2.2.3 | Assembly of the device

The PDMS slab and the glass chip were autoclaved at 121 °C for 15 min prior to bonding. The remaining steps were carried out under sterile conditions with the help of a custom-made support. Surfaces to be bonded were activated using O2 plasma at 200 W for 24 s. Both parts were immediately aligned under a stereomicroscope and brought into conformal contact. The device was then baked at 100 °C for 15 min for complete sealing (step 18). To maintain hydrophilicity, the device was immersed in distilled water until utilization.

5.2.3 | Permeability assay

The endothelial and epithelial permeabilities were quantified by the passage of labelled tracers. This assay was carried out after the cells were perfused for 3 days in the device. Afterwards, pipette tips were connected at the inlets and outlets to fill the compartments with the tracers. The compartment with epithelial cells was carefully filled with medium containing fluorescein isothiocyanate-dextran (FITC-dextran)

(70kDa, Sigma Aldrich) at a concentration of 50 µg mL^{-1}. The compartment with endothelial cells was filled with medium containing Rhodamine B isothiocyanate-dextran (RITC-dextran) (70kDa, Sigma Aldrich) at a concentration of 5 mg mL^{-1}. The device was then placed in an incubator at 37 °C and 5 % CO_2. At 30 min, fluorescence microscopy images were taken from the device using an Olympus 1X71 inverted microscope at an exposure time of 0.33 (RITC) and 0.67 ms (FITC). In the same way, a compartment of a device without cells was filled with both labelled dextrans, and fluorescence microscopy images were taken every 5 min for 30 min. Fluorescence images were analysed with ImageJ software to quantify the intensity in the compartments. Normalization was performed by dividing the intensity in the receiving compartment by the intensity in the donor compartment. According to Fick's First Law and provided that there is a lineal relation between intensity and dextran amount, the initial slope of the normalized intensity will be related to the permeability as [24, 25]

$$P = \frac{1}{I_d}\frac{dI_r}{dt}\frac{V}{S} \tag{5-1}$$

where P is the permeability coefficient, I_d and I_r, respectively, are the fluorescence intensities in the donor and receiving compartments, V is the donor volume, and S is the permeable area (grid of microgrooves).

5.2.4 | Transepithelial electrical resistance

TEER is conventionally obtained using electrodes in apical and basal sides, so that the electrical current flows across the cell barrier. In this approach, there are two electrodes placed at the bottom of the microgrooves, and the current flows from one electrode to another crossing the cell barrier twice. A schematic representation of this measurement system and the equivalent electric circuits with lumped elements are shown in Figure 5-6. Unlike the conventional measurement system, this approach includes the parasitic resistance of the solution in the basal side (the medium in the microgrooves, $R_{\mu g}$). At relatively middle frequencies (~1-10 kHz), the measured impedance is purely resistive (phase = 0 °) and associated with the equivalent electric circuit shown in Figure 5-6c. This is because the electrode polarization impedances (CPE_e) and the C_{cl} do not contribute significantly to the measured impedance in this range of frequencies. To convert TEER values in units of Ω cm^2, a numerical study as in chapter 2 [13] is provided in the Figure 5-7. Normalizing the TEER to the area of the electrodes does not take into account that the effective area through which the current passes the cell layer depends on the TEER value.

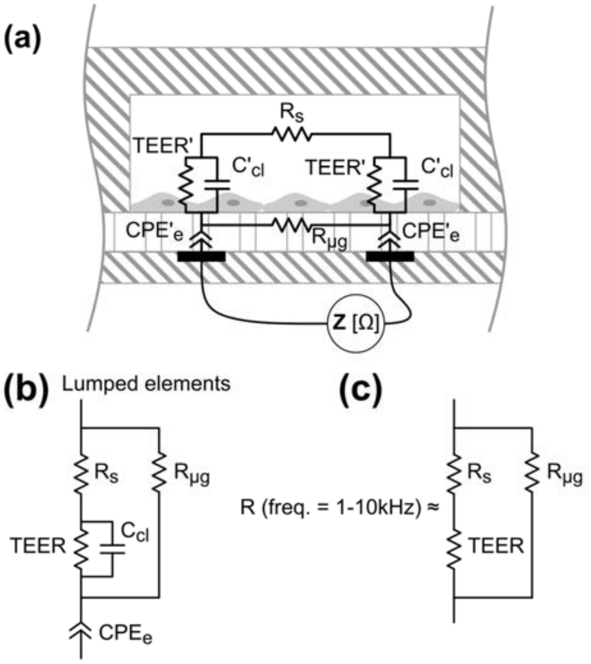

Figure 5-6 (a) Schematic representation of the measurement system consisting of two electrodes under the microgrooves. The equivalent electric circuit includes constant phase element (CPE_e) that represents the electrode polarization impedance, C_{cl}, luminal medium resistance (R_s), basolateral medium resistance ($R_{\mu g}$), and transepithelial electrical resistance (TEER). (b) Lumped elements model of the equivalent electric circuit. (c) Equivalent electric circuit of the resistance measured at relatively middle frequencies (from 1 to 10 kHz).

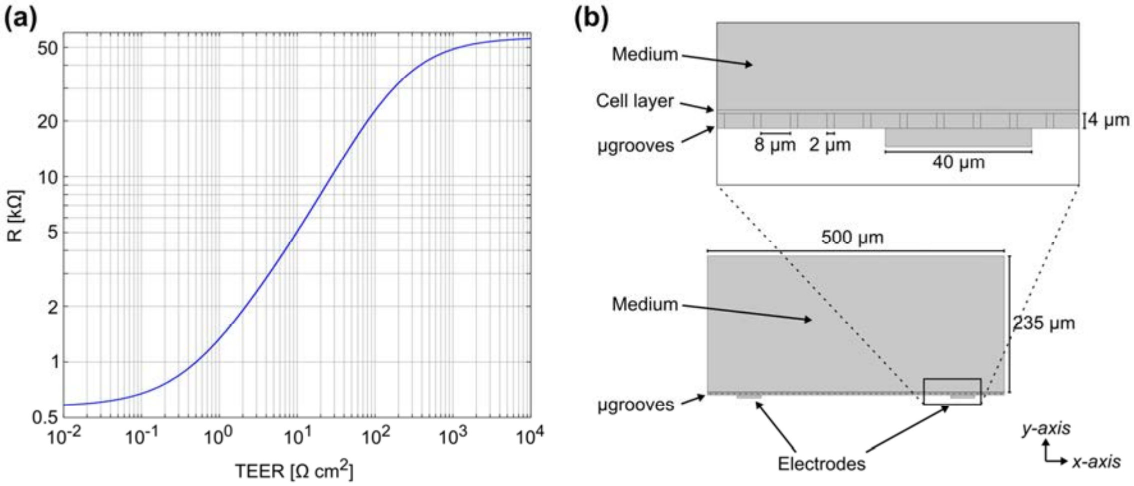

Figure 5-7 TEER normalization to area obtained by numerical study. (a) Resistance measured (R) with the system as a function of the TEER in units of Ω cm^2. The numerical study was performed according to the previous study using COMSOL Multiphysics version 5.1 and its AC/DC module. (b) Schematic representation of the simulated model with dimensions. The model is a 2D vertical cross-section of the microfluidic system including a cell layer, a medium compartment, microgrooves and electrodes. Cell barriers with different TEER values were simulated by changing the conductivity of the area of the cell layer. Electrical conductivity of the medium and the microgrooves was 1.5 S m^{-1}. The conductivity in the space of 8 µm between microgrooves was 0.3 S m^{-1} (microgroove separation was divided by the width of microgrooves (10 µm / 2 µm)) to account for the microgrooves in the *x-axis* direction.

Electrical impedance between the two electrodes was acquired with the impedance analyser [26] and measured at 20 frequencies ranging from 100 Hz to 1 MHz. As in the previous chapter, the analyser was adapted to apply a maximum voltage and current of 10 mVp and 10 µAp, respectively. The resistance at middle frequencies (Figure 5-6c) was obtained from fitting the impedance spectra using the least-squares method in Matlab.

5.2.5 | Cell culture

Epithelial monolayers were obtained with ARPE-19 cells (ATCC, US), an immortalized human retinal pigment epithelial cell line. These epithelial cells form stable monolayers, which exhibit morphological and functional polarity under specific culture conditions. ARPE-19 cells were cultured in Dulbecco's modified Eagle's medium (DMEM) and Ham's F-12 nutrient mixture (1:1), 10 % foetal bovine serum (FBS), and 2 mmol L^{-1} penicillin/streptomycin. Experiments were performed at passage 23. Endothelial monolayers were obtained with primary HREC (Innoprot, ES). Endothelial cells were cultured in Endothelial Medium (EM, Innoprot, ES), (5%) FBS, 2 mmol L^{-1} penicillin/streptomycin, and experiments were performed at passage 3. Human neural cells (SH-SY5Y cell line) were obtained from ECACC (Sigma-Aldrich, ES) and cultured in DMEM, 5 % FBS, 2 mmol L^{-1} penicillin/streptomycin.

Compartments of the device were coated with fibronectin (Millipore, ES) at a concentration of 100 µg mL^{-1} (2.3 µg cm^{-2}) and incubated at 37 °C for 1 h. The device with fibronectin was rinsed with culture medium and incubated for 30 min. SH-SY5Y, HREC, and ARPE-19 cells were then seeded at a concentration of 2×10^6 cells cm^{-2} and incubated at 37 °C and 5 % of CO_2 until the end of the experiment.

5.2.6 | Experimental setup

Neuronal cells were cultured in the three middle compartments of the device containing the recording electrodes. Otherwise, endothelial and epithelial cells were cultured in the compartments adjacent to those with the neurons as shown in Figure 5-1b.

After seeding, cells were incubated under static conditions for 1.5-3 h to ensure cell attachment. Then, the cells were perfused with their respective culture media at a rate of 0.1 mL min^{-1} for 3 days. For the case of the neuronal cells, the medium was only flowed through the central compartment to simplify the fluidic connections. Culture medium was injected using a syringe pump (NE-4000, New Era Pump Systems, Inc., US) in infusion mode. PTFE tubes (0.5 mm internal diameter [ID] and 1 mm outer diameter [OD]) were cut and inserted into the inlets and outlets of the device. Inlet tubes were connected to syringes containing culture media, and the outlet tubes were connected to reservoirs (silicone tube of 0.8 mm ID and 2.4 mm OD). To ensure proper equilibration of the medium with the incubator, reservoirs were vented and placed near the outlets.

5.2.7 | Immunocytofluorescence

Cells were cultured under the conditions previously described. At the end of each experiment, cells were washed with Dulbecco's phosphate-buffered saline (DPBS) and blocked with DPBS containing 2 % bovine serum albumin (BSA) and 0.05 % Tween for 1 h at room temperature. Then, the cells were incubated with mouse anti-human ZO-1 antibody (Zymed, Invitrogen, ES) diluted 1/200 in the same buffer overnight at 4 °C. After washing two times with DPBS, cells were further incubated with a fluorescent secondary antibody (Alexa 594, Invitrogen, ES) for 1 h at room temperature. Nuclei were stained in blue with 4′-6-diamidino-2-phenylindole (DAPI) (Vector Laboratory, US). Images were acquired with a confocal laser scanning microscope (FV1000, Olympus, DE) (ARPE-19 cells) and an Olympus 1X71 inverted microscope (SH-SY5Y cells).

5.3 | RESULTS AND DISCUSSION

The developed microfluidic device was validated with a co-culture of primary HREC, the SH-SY5Y human neuroblastoma cell line, and the ARPE-19 human retinal pigment epithelial cell line. Cells were cultured at confluence, and maintained with a continuous supply of culture medium for 3 days (Figure 5-8). The formation of endothelial and epithelial barriers was assessed by their permeability to dextran 70kDa, TEER measurements, and ZO-1 expression. In addition, SH-SY5Y cells exhibited a more neuronal morphology at the 3rd day.

5.3.1 | Permeability assay and immunocytofluorescence

Reduced permeability to large dextran molecules was found in both endothelial and epithelial cell monolayers (Figure 5-9). Fluorescence images taken from the blank control (without cells) show that the devices were properly sealed. The PDMS successfully bonded on top of the microgroove grid, letting the tracer pass only through the grooves. In Figure 5-9d, a zoomed view of the PDMS wall between two adjacent compartments is shown. In addition, cells did not cross between compartments, and those compartments without cells still remained empty at the end of the experiment. The size of the microgrooves are small enough (2 μm width and 4 μm depth) to prevent cell migration between compartments, but they are large enough to allow neuritic processes to extend between compartments through the microgrooves under the wall.

RITC and FITC dextrans were used to simultaneously quantify the permeability of both endothelial and epithelial barriers. Fluorescence intensities in the receiving compartments, adjacent to the donor compartments, and calculated permeabilities are shown in Figure 5-9c. In the blank control, both labelled dextrans were rapidly distributed throughout the device when they were injected into one compartment as

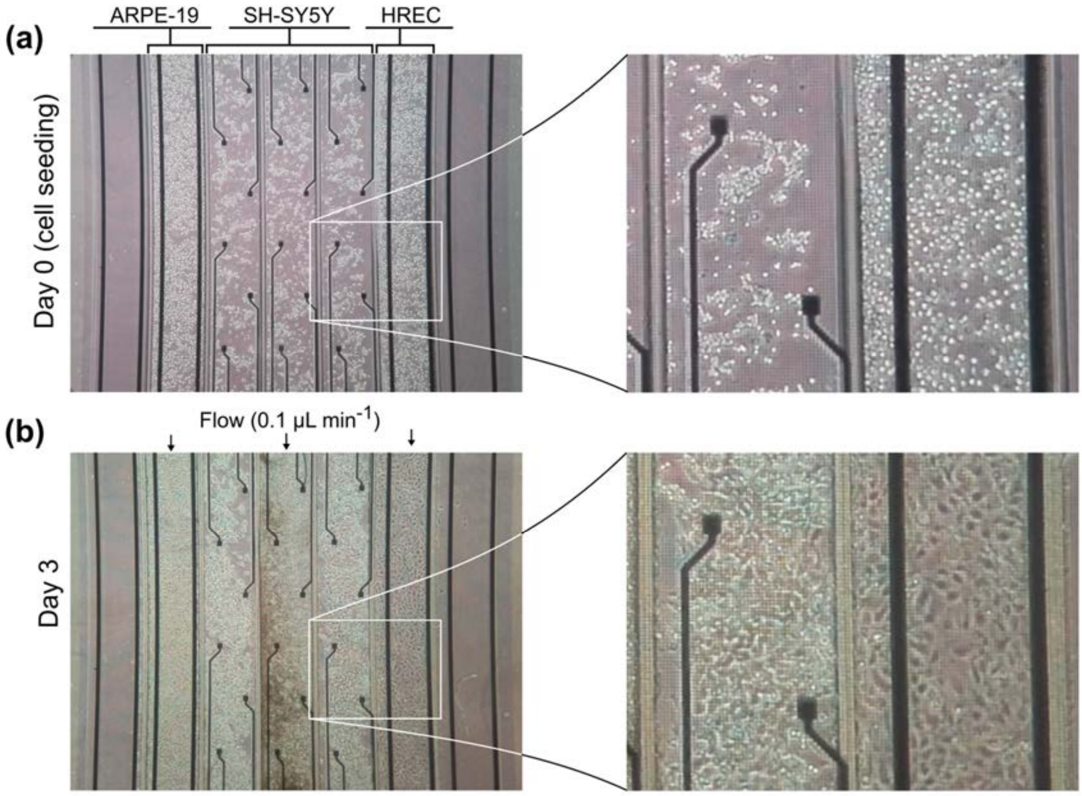

Figure 5-8 Phase contrast images of the cells in the zone of the grid of microgrooves of the device. Images were taken (a) at the cell seeding and (b) at the third day. Cells in the compartments pointed with arrows were perfused with their respective culture media at a rate of 0.1 mL min-1 for 3 days.

evidenced by the fluorescence images taken at 1 and 30 min. Otherwise, the endothelial and epithelial compartments exhibited little permeation to dextran, at least for 30 min. Only a little fluorescence was observed in the adjacent compartments as shown in the zoomed view in Figure 5-9e. Permeability was shown to decrease by more than 1 order of magnitude. However, further studies using longer assay times are needed. The planar disposition of the device allows real-time imaging of the whole cell culture. Furthermore, transport studies can be conducted with high spatiotemporal resolution which is not possible with conventional methods based on collecting samples. Indeed, some authors have utilized similar planar approaches to perform time course monitoring of labelled tracers [25].

In addition to permeability analysis and TEER, immunocytofluorescence staining for ZO-1 was performed after 3 days for ARPE-19 cells. It demonstrated barrier formation on the grid of microgrooves. The ZO-1 protein was localized at the peripheral membrane and continuous distributed alongside the epithelial monolayer (Figure 5-10d). SH-SY5Y cells also proliferated on the grid. At the end of the experiment, there were some cells forming clusters with more neuronal phenotypes and extended neuritic processes (Figure 5-10e).

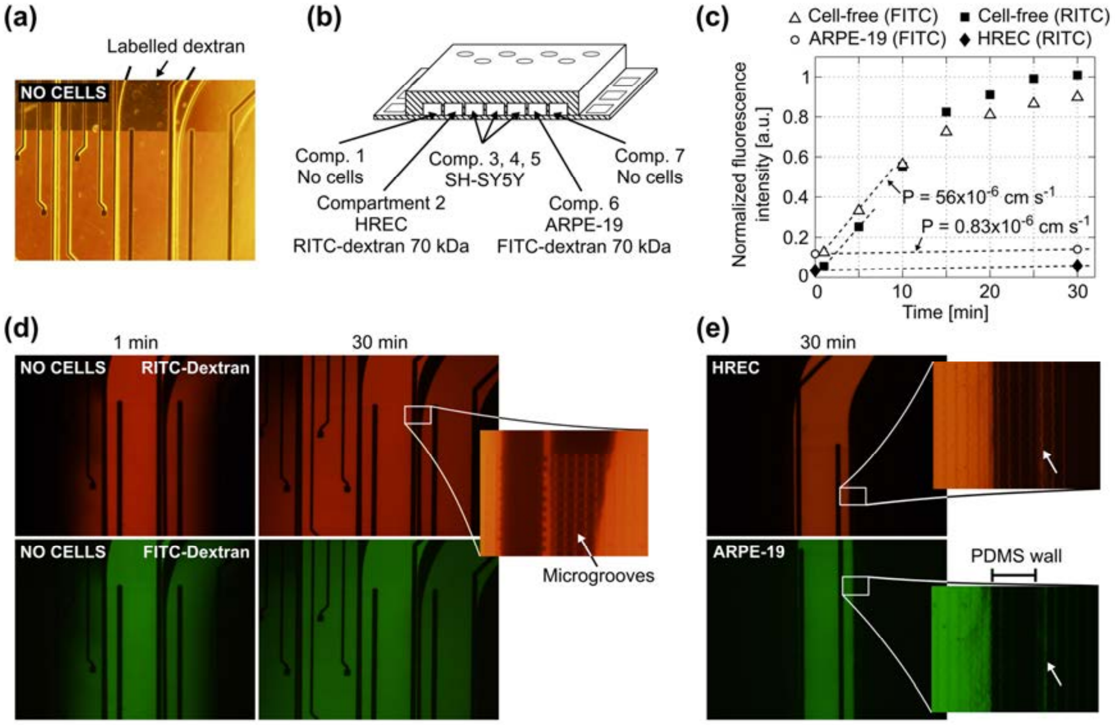

Figure 5-9 Permeability to labelled dextran 70 kDa. (a) Contrast phase image of the compartments without cells. Note that metal electrodes and electric tracks are opaque. (b) Schematic drawing (not to scale) of the arrangement of the cells and labelled dextrans. (c) Normalized fluorescence intensity in the receiving compartment that is adjacent to the donor compartment. Intensity was quantified from the mean of an area in the middle of the compartment with ImageJ software and normalized by dividing by the intensity at the donor compartment. Permeability was calculated according to equation (5-1) using the initial slope of the normalized fluorescence ((in cm s^{-1}) $P_{cell\text{-}free(FITC)} = 56x10^{-6}$, $P_{cell\text{-}free(RITC)} = 53x10^{-6}$, $P_{ARPE\text{-}19(FITC)} = 0.83x10^{-6}$, and $P_{HREC(RITC)} = 0.88x10^{-6}$). (d) Fluorescence microscopy images without cells at 1 and 30 min after the administration of RITC and FITC dextrans in one of the compartments. In the zoomed view, a PDMS wall that separates two compartments and a TEER measurement electrode (left side) is shown. Indicated with an arrow is the location of the microgrooves under the PDMS wall. (e) Fluorescence microscopy image at 30 min after the administration of RITC or FITC dextran in a compartment with a monolayer of HREC or ARPE-19. Images were taken once the cells have stayed in the device for 3 days. The arrow in the zoomed view points to a little fluorescence in the adjacent compartment after the PDMS wall.

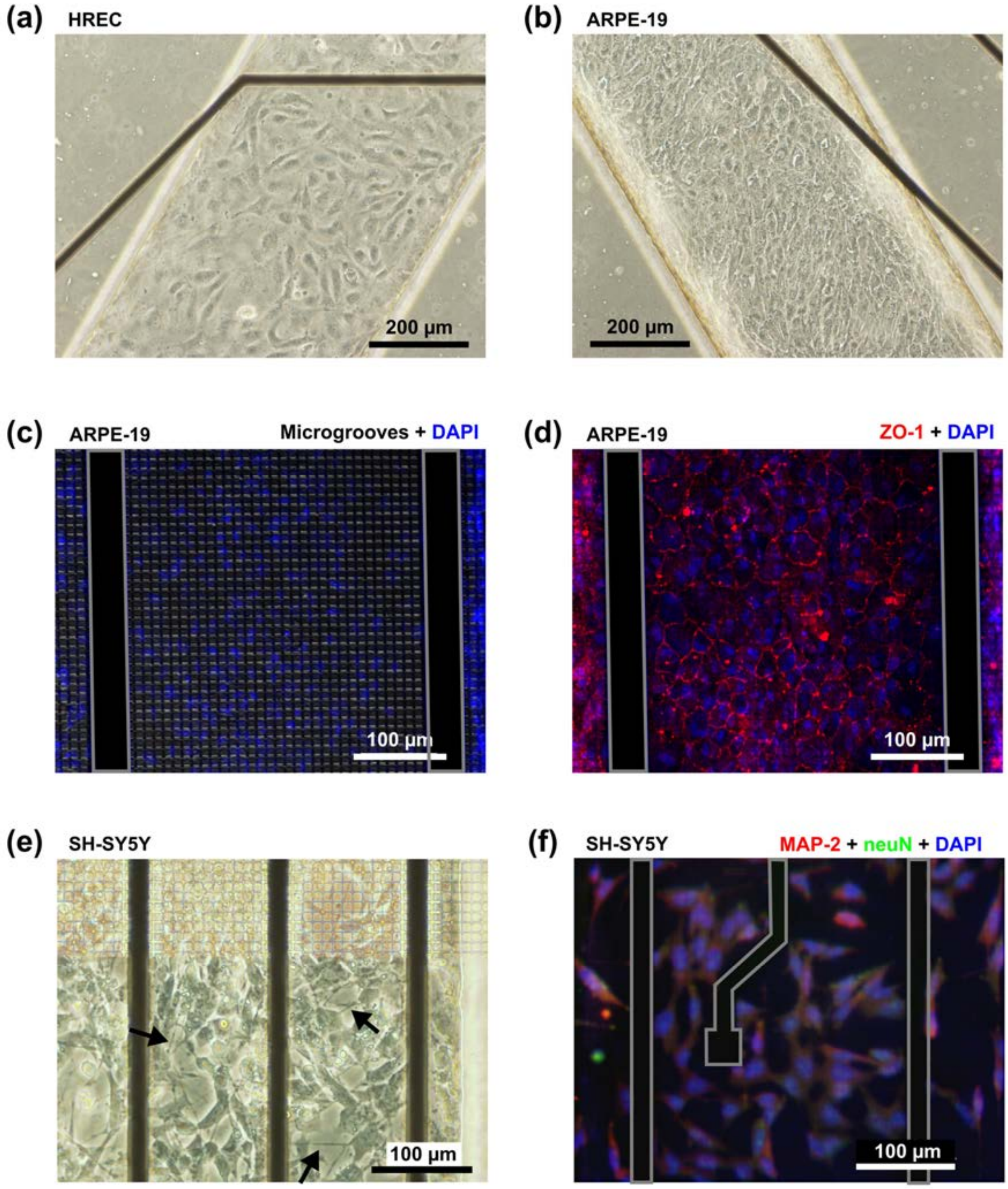

Figure 5-10 Light microscopy of (a) HREC and (b) ARPE-19 cells after 3 days in the device. Images were taken in the microfluidic inlets outside the grid of microgrooves. Note that black lines are the electrical tracks that connect the electrodes with the pads. (c–d) Confocal microscopy image (X10) of human retinal epithelial monolayer lining the grid of microgrooves in the device. (c) The image is an overlap of the grid of microgrooves and cell nuclei stained with DAPI (blue). (d) Overlap of ZO-1 protein (red) and DAPI. (e) Light microscopy of the SH-SY5Y taken at the edge of the grid of microgrooves. Arrows point to occasional extensions of neuritic processes. (f) Fluorescence image of SH-SY5Y cells following staining with DAPI (Blue), anti-NeuN antibody [EPR12763] - neuronal marker with Alexa 488 (green), and anti-Map2 (ab32454) - neuronal marker with Alexa 568 (red).

5.3.2 | Transepithelial electrical resistance

To validate the TEER measurement system that uses two straight parallel electrodes at the bottom of the microgrooves, it was compared the resistance measured using this two basal electrodes to the conventional TEER measurement using electrodes in apical and basal sides. For that, the PDMS slab of the device was perforated as in Figure 5-11a to introduce an additional Pt wire electrode in the apical side. In Figure 5-11b, the time course of the resistances is shown during the administration and removal of ethylenediaminetetraacetic acid (EDTA) in ARPE-19 cells cultured for 1 day for both configurations. The application of the calcium chelating agent EDTA induced in a few minutes rapid barrier breakdown, whereas its removal caused the recovery of the barrier to its initial values. EDTA removes extracellular Ca^{2+} of the medium, which in turn opens the paracellular pathway presumably through stimulation of protein kinase C [27, 28] and upregulation of intracellular Ca^{2+}. As a result, Ca^{2+} depletion induces disruption of intercellular junctions, disruption of actin filaments, and event delocalization of tight junctions when depletion is prolonged [29]. During transient Ca^{2+} removal (approximately less than 1 h), tight junctions remain localized in the region of cell-cell contacts, and TEER alternatively drops and is recovered in a process that usually takes several hours; this transient disruption has been exploited to enhance drug permeability [30].

It can be observed that the time courses of the resistance measured between the apical electrode and each one of the basal electrodes ($R_{E1\leftrightarrow E3}$ and $R_{E2\leftrightarrow E3}$) were equal as expected. In addition, the sum of these two resistances ($R_{E1\leftrightarrow E3} + R_{E2\leftrightarrow E3}$) fitted the same time course of the resistance measured between basal electrodes in our method ($R_{E1\leftrightarrow E2}$). This demonstrates that the proposed measurement system is feasible to

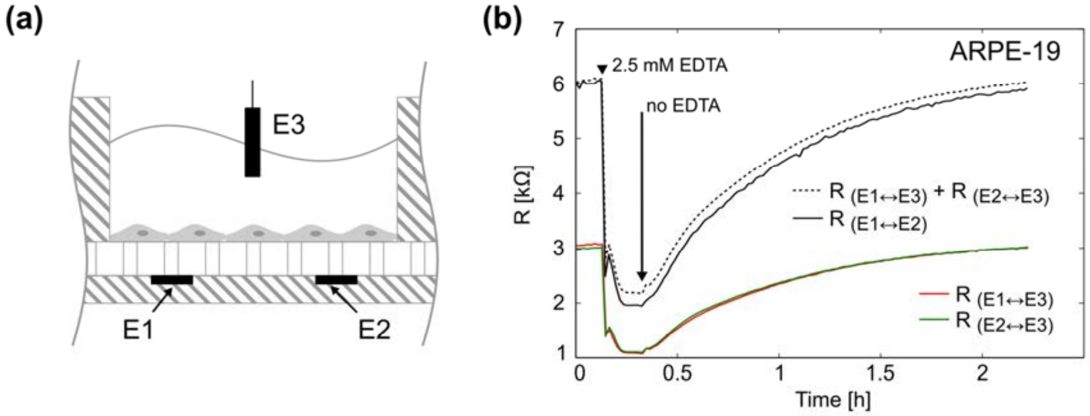

Figure 5-11 TEER measurement system validation. (a) Schematic representation of the electrode configuration used to validate the measurement system based on two electrodes under the microgrooves (E1 and E2). For this purpose, the device was perforated and an additional Pt wire electrode (E3) was introduced in the apical side. This electrode configuration allow us to measure three resistances; 1) the resistance between the electrodes under the microgrooves ($R_{E1\leftrightarrow E2}$), 2) the resistance between E1 and E3 ($R_{E1\leftrightarrow E3}$), and 3) the resistance between E2 and E3 ($R_{E2\leftrightarrow E3}$). (b) ARPE-19 cells were cultured for 1 day, and the three resistances were measured during a calcium switch procedure. The sum of $R_{E1\leftrightarrow E3}$ and $R_{E2\leftrightarrow E3}$ is shown in dashed lines and fits the same time course variations of $R_{E1\leftrightarrow E2}$.

determine the TEER. It offers the advantage of measuring the TEER in many compartments without integrating electrodes in the PDMS slab, which is time-consuming and has poor reproducibility. However, some considerations have to be addressed with this methodology.

Depending on the microgroove dimensions, there may be a limitation when measuring high TEER values because the resistance of the solution in the basal side ($R_{\mu g}$) is in parallel with the TEER. Therefore, there will be an underestimation of the TEER as its value approaches $R_{\mu g}$. For example, if TEER plus the resistance of the solution in the apical side (R_s) is smaller than $R_{\mu g}$ ($TEER + R_s < R_{\mu g}$) most of the current will flow across the cell barrier, and the measured resistance will be the TEER plus the R_s. Otherwise ($TEER + R_s > R_{\mu g}$), most of the current will flow through the solution contained in the microgrooves without crossing the cell barrier. For the determined electrodes and microgroove dimensions, this $R_{\mu g}$ (40 kΩ, details are provided in Figure 5-12) is much higher than the maximum measured resistance in this study (R < 6 kΩ). Thus, the measured resistance (R) was mainly contributed by the TEER in series with R_s. Although the measurement system is suitable to measure a large range of TEER values neglecting $R_{\mu g}$, it would be possible to incorporate the calculated $R_{\mu g}$ value when measuring high TEER values.

In Figure 5-13a, the impedance spectra measured with and without a monolayer (ARPE-19 or HREC) covering the grid are shown. In the Bode representation, the change that causes the cell barrier in the impedance spectra is clearly observed. Herein, the rise in resistance in the middle frequencies is associated with the increase of the TEER value. The time course of R is shown in Figure 5-13b. After 1 h, cells were successfully attached to the microgroove grid, and during the first day, the R increased supposedly due to cell spreading until it reached a plateau. This coincided with the monolayer formation observed under the microscope.

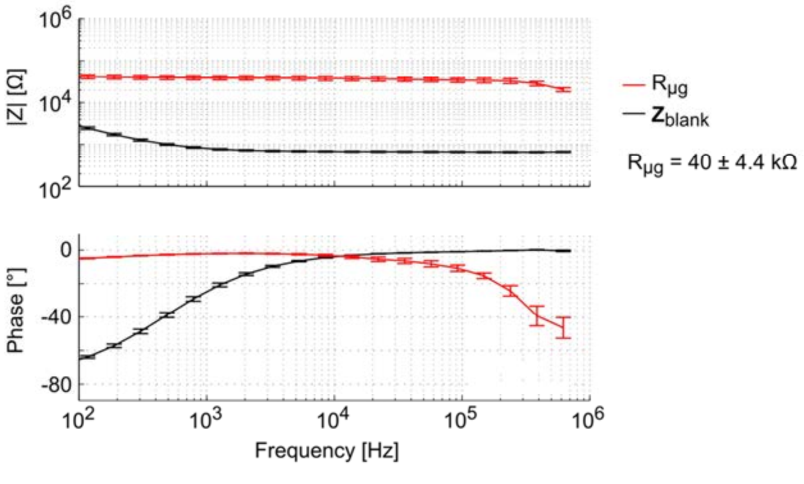

Figure 5-12 Bode representation of the Impedance of the solution contained in the microgrooves ($R_{\mu g}$). This measurement was performed pouring a drop of PBS over the chip and pressing the drop with a piece of flat PDMS. $R_{\mu g}$ was 40 ± 4.4 kΩ (n = 8). There is also included in the figure the impedance spectra measured without the PDMS.

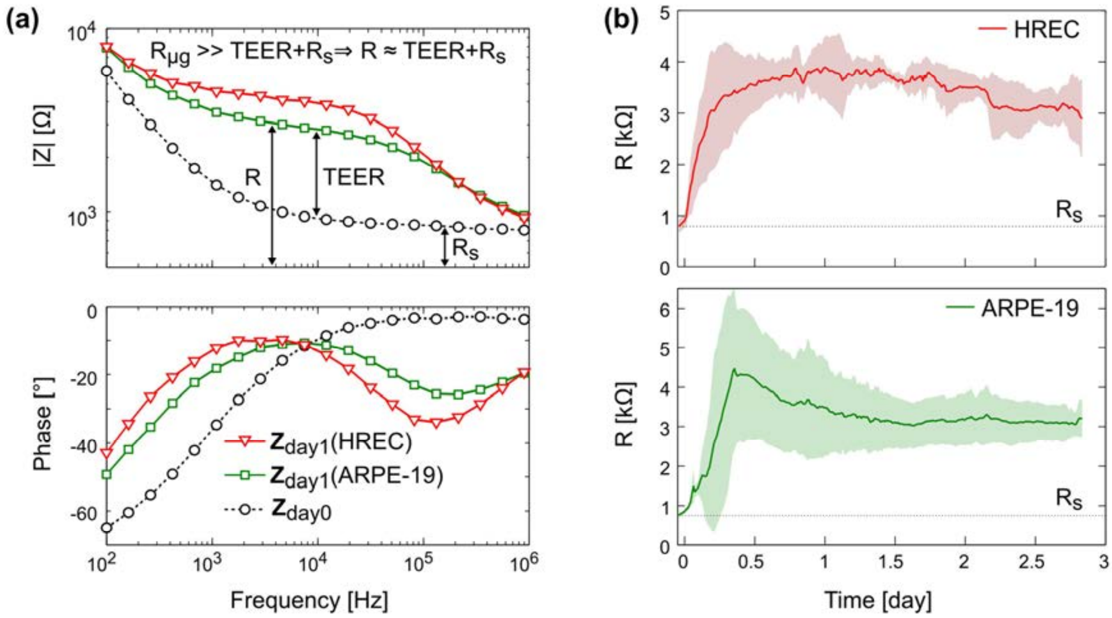

Figure 5-13 Transepithelial electrical resistance measurement. (a) Bode representation of the impedance spectra measured before cell seeding (dashed line and circle symbol) and after 1 day for HREC (green square symbol) and ARPE-19 (red inverted triangle symbol) cultures. (b) Time course of the resistance measured for HREC (red line) (n = 4) and ARPE-19 (green line) (n = 3) cultures. Data was acquired each 15 min for 3 days. Note that there are data before cell seeding (time 0) that correspond to the measure without cells.

Although there was no significant difference in R between ARPE-19 and HREC at the 3rd day (3.2 ± 0.46 kΩ [4.9 Ω cm^2] and 2.9 ± 0.73 kΩ [4.2 Ω cm^2], respectively), the real-time functionality allowed us to observe some different behaviours in cell attachment and spreading. For instance, the R of HREC cells experienced an exponential increase after cell seeding. Otherwise, the R of ARPE-19 cells increased with a constant slope, and made a noticeable overpeak. Herein, it has to be noted that the variability between experiments was observed when the flow was connected.

The formation of the tight junctions depends on the experimental conditions and in particular on the number of cells plated to reach confluence. In cultures in which a high amount of cells has been seeded, the tight junction ZO-1 appears by western blot as soon as 4-8 h but the protein forming an efficient barrier between cells is not visible by immunohistochemistry until 2-3 days. This has also been reported in both ARPE-19 [31, 32] and HREC [33–36]. Immunofluorescence images of the cells at the 3rd day of culture in Petri dishes are shown in Figure 5-14.

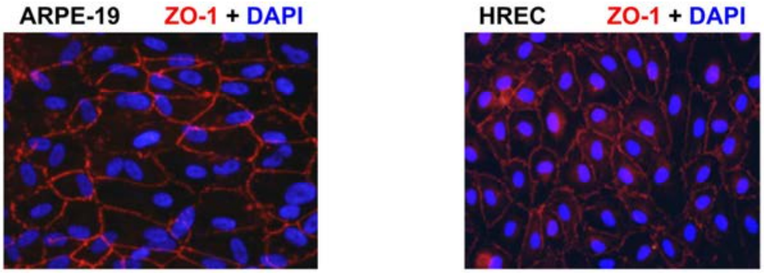

Figure 5-14 Overlap of ZO-1 (red) and DAPI (blue) immunofluorescence in ARPE-19 cells and HREC in cell monolayers (X20) at the 3rd day of culture in Petri dishes.

5.3.3 | Limiting factors

Herein, there are summarized several limiting factors of the device as well as some issues of the microfluidic cell culture that is important to discuss:

Heterotypic cell-cell interaction. Heterotypic cell-cell interactions in the human retina can occur largely through direct contact and paracrine signalling. In the former, cells are very close and share some binding molecules. In the latter, signal molecules are released from one type of cell and they diffuse through the extracellular medium to other cell types. Therefore, in our device we could only mimic paracrine signalling since direct contact is not possible *a priori*.

Device reusability. Since detergent solutions and solvents could be absorbed into the PDMS and then released during the cell culture, the cleaning of the device for its reuse can compromise the integrity of the cell culture. To overcome this limitation, a reversible bonding between the glass chip and the PDMS slab would be suitable to, at least, reuse the glass chip.

Neuronal recording. The coupling between cells and electrodes is a critical issue for the ability to record neuronal activity. In the device, electrodes are buried 3.5 μm from the surface where cell somas are expected to be. A possible strategy to improve this coupling could be to electrochemically coat the electrodes with sufficient platinum black to allow direct contact between electrodes and neurons.

5.4 | CONCLUSIONS

The interconnection of different tissue-tissue interfaces together with cell exposure to constant flow may expand organ-on-chips to a new generation of sophisticated models capable of recapitulating more complex organ-level functions. Here, it was developed a microfluidic cell culture device where more than one tissue barrier function can be emulated. It is based on a grid of microgrooves that allows heterotypic cell-cell interactions and the formation of several tissues. Microfabrication techniques were used to construct the device, allowing the integration of TEER electrodes for continuous monitoring. Moreover, its planar disposition enables real-time imaging with high spatiotemporal resolution.

As a proof-of-concept, the fabricated device was used to mimic the structure of the BRB by co-culturing HREC (inner BRB), SH-SY5Y cells (neuroretina), and ARPE-19 cells (outer BRB). Tissues on the microgrooves were assessed by a permeability assay, TEER measurements, and ZO-1 expression. To measure the TEER in real-time, it has been presented a method based on electrodes placed at the basal side (situated under the microgrooves) of both cell monolayers.

In conclusion, the presented multi-compartment microfluidic device with integrated electrophysiological monitoring electrodes will permit to make more accurate measurements of cell behaviour than can be obtained in the currently static models. Thus, it can be envisaged as a promising new approach for recapitulating multi-barrier models. In particular, it will facilitate the study of retinal diseases affecting BRB integrity and neurovascular coupling such as DR, which remains the leading cause of blindness in working-age individuals in the western world.

5.5 | REFERENCES

[1] Yum K, Hong SG, Healy KE, et al. Physiologically relevant organs on chips. *Biotechnol J* 2014; 9: 16–27.

[2] Bhatia SN, Ingber DE. Microfluidic organs-on-chips. *Nat Biotechnol* 2014; 32: 760–772.

[3] Moraes C, Mehta G, Lesher-Perez SC, et al. Organs-on-a-Chip: A Focus on Compartmentalized Microdevices. *Ann Biomed Eng* 2012; 40: 1211–1227.

[4] Achyuta AKH, Conway AJ, Crouse RB, et al. A modular approach to create a neurovascular unit-on-a-chip. *Lab Chip* 2013; 13: 542–553.

[5] Huh D, Matthews BD, Mammoto A, et al. Reconstituting Organ-Level Lung Functions on a Chip. *Science* 2010; 328: 1662–1668.

[6] Griep LM, Wolbers F, Wagenaar B de, et al. BBB ON CHIP: microfluidic platform to mechanically and biochemically modulate blood-brain barrier function. *Biomed Microdevices* 2013; 15: 145–150.

[7] Booth R, Kim H. Characterization of a microfluidic in vitro model of the blood-brain barrier (μBBB). *Lab Chip* 2012; 12: 1784–1792.

[8] Achyuta AKH, Conway AJ, Crouse RB, et al. A modular approach to create a neurovascular unit-on-a-chip. *Lab Chip* 2013; 13: 542–553.

[9] Sticker D, Rothbauer M, Lechner S, et al. Multi-layered, membrane-integrated microfluidics based on replica molding of a thiol–ene epoxy thermoset for organ-on-a-chip applications. *Lab Chip* 2015; 15: 4542–4554.

[10] Booth R, Noh S, Kim H. A multiple-channel, multiple-assay platform for characterization of full-range shear stress effects on vascular endothelial cells. *Lab Chip* 2014; 14: 1880–1890.

[11] Henry OYF, Villenave R, Cronce MJ, et al. Organs-on-chips with integrated electrodes for trans-epithelial electrical resistance (TEER) measurements of human epithelial barrier function. *Lab Chip* 2017; 17: 2264–2271.

[12] van der Helm MW, Odijk M, Frimat J-P, et al. Direct quantification of transendothelial electrical resistance in organs-on-chips. *Biosens Bioelectron* 2016; 85: 924–929.

[13] Yeste J, Illa X, Gutiérrez C, et al. Geometric correction factor for transepithelial electrical resistance measurements in transwell and microfluidic cell cultures. *J Phys Appl Phys* 2016; 49: 375401.

[14] Odijk M, Meer AD van der, Levner D, et al. Measuring direct current trans-epithelial electrical resistance in organ-on-a-chip microsystems. *Lab Chip* 2015; 15: 745–752.

[15] Wang YI, Abaci HE, Shuler ML. Microfluidic blood-brain barrier model provides in vivo-like barrier properties for drug permeability screening: Microfluidic BBB Model Mimics In Vivo Properties. *Biotechnol Bioeng* 2017; 114: 184–194.

[16] Maoz BM, Herland A, Henry OYF, et al. Organs-on-Chips with combined multi-electrode array and transepithelial electrical resistance measurement capabilities. *Lab Chip* 2017; 17: 2294–2302.

[17] Sun T, Swindle EJ, Collins JE, et al. On-chip epithelial barrier function assays using electrical impedance spectroscopy. *Lab Chip* 2010; 10: 1611–1617.

[18] Wegener J, Keese CR, Giaever I. Electric Cell–Substrate Impedance Sensing (ECIS) as a Noninvasive Means to Monitor the Kinetics of Cell Spreading to Artificial Surfaces. *Exp Cell Res* 2000; 259: 158–166.

[19] Giaever I, Keese CR. Use of Electric Fields to Monitor the Dynamical Aspect of Cell Behavior in Tissue Culture. *IEEE Trans Biomed Eng* 1986; BME-33: 242–247.

[20] Obien MEJ, Deligkaris K, Bullmann T, et al. Revealing neuronal function through microelectrode array recordings. *Front Neurosci* 2015; 8: 423.

[21] Klaassen I, Van Noorden CJF, Schlingemann RO. Molecular basis of the inner blood-retinal barrier and its breakdown in diabetic macular edema and other pathological conditions. *Prog Retin Eye Res* 2013; 34: 19–48.

[22] Wong TY, Cheung CMG, Larsen M, et al. Diabetic retinopathy. *Nat Rev Dis Primer* 2016; 2: 16012.

[23] Gabriel G, Erill I, Caro J, et al. Manufacturing and full characterization of silicon carbide-based multi-sensor micro-probes for biomedical applications. *Microelectron J* 2007; 38: 406–415.

[24] Huxley VH, Curry FE, Adamson RH. Quantitative fluorescence microscopy on single capillaries: alpha-lactalbumin transport. *Am J Physiol - Heart Circ Physiol* 1987; 252: H188.

[25] Deosarkar SP, Prabhakarpandian B, Wang B, et al. A Novel Dynamic Neonatal Blood-Brain Barrier on a Chip. *PLOS ONE* 2015; 10: e0142725.

[26] Guimerà A, Gabriel G, Parramon D, et al. Portable 4 Wire Bioimpedance Meter with Bluetooth Link. In: Dössel O, Schlegel WC, Magjarevic R (eds) *World Congress on Medical Physics and Biomedical Engineering*. Berlin: Springer, pp. 868–871.

[27] Citi S. Protein kinase inhibitors prevent junction dissociation induced by low extracellular calcium in MDCK epithelial cells. *J Cell Biol* 1992; 117: 169–178.

[28] Tomita M, Hayashi M, Awazu S. Absorption-Enhancing Mechanism of EDTA, Caprate, and Decanoylcarnitine in Caco-2 Cells. *J Pharm Sci* 1996; 85: 608–611.

[29] Siliciano JD. Localization of the tight junction protein, ZO-1, is modulated by extracellular calcium and cell-cell contact in Madin-Darby canine kidney epithelial cells. *J Cell Biol* 1988; 107: 2389–2399.

[30] Deli MA. Potential use of tight junction modulators to reversibly open membranous barriers and improve drug delivery. *Biochim Biophys Acta BBA - Biomembr* 2009; 1788: 892–910.

[31] Yoshikawa T, Ogata N, Izuta H, et al. Increased Expression of Tight Junctions in ARPE-19 Cells Under Endoplasmic Reticulum Stress. *Curr Eye Res* 2011; 36: 1153–1163.

[32] Hirata J, Ko J-A, Mochizuki H, et al. Oxidative stress regulates expression of claudin-1 in human RPE cells. *Open Life Sci* 2014; 9: 461–468.

[33] Gardner TW, Lesher T, Khin S, et al. Histamine reduces ZO-1 tight-junction protein expression in cultured retinal microvascular endothelial cells. *Biochem J* 1996; 320: 717–721.

[34] Kim J-H, Kim JH, Jun H-O, et al. Inhibition of Protein Kinase C δ Attenuates Blood-Retinal Barrier Breakdown in Diabetic Retinopathy. *Am J Pathol* 2010; 176: 1517–1524.

[35] Jiang Y, Liu L, Steinle JJ. Compound 49b Regulates ZO-1 and Occludin Levels in Human Retinal Endothelial Cells and in Mouse Retinal Vasculature. *Investig Opthalmology Vis Sci* 2017; 58: 185.

[36] Ye E-A, Liu L, Steinle JJ. miR-15a/16 inhibits TGF-beta3/VEGF signaling and increases retinal endothelial cell barrier proteins. *Vision Res*. Epub ahead of print 7 August 2017. DOI: 10.1016/j.visres.2017.07.007.

6

Conclusions and future work

6.1 | OVERVIEW

Epithelial and endothelial barriers are crucial to maintain organ homeostasis and their deregulation play an important role in the pathogenesis and progression of many prevalent human diseases. Most *in vitro* models of biological barriers, typically based on Petri dishes or Transwell inserts, have been restricted to one or two different cell types and have been inadequate to apply controlled physical or biochemical stimuli that emulate the *in vivo* microenvironment. Taking advantage of the available microfabrication techniques and biomaterials, it has been possible to refine conventional *in vitro* models towards more sophisticated MPS able to better predict human response. Current MPS are heterotypic cell cultures with physiologically relevant organizations, where cells, for example, can be embedded in an ECM with a particular stiffness, seeded on a surface with certain topography, subjected to mechanical forces such as FSS and cyclic stretching, or exposed to concentration gradients of cytokines and growth factors. Although it is debatable whether an *in vitro* model predicts human response or emulates the complexity of human organ-level physiology, human cell cultures can be more reliable than animal testing due to species differences as well as being inexpensive and less time-consuming. Furthermore, they are a viable way to satisfy in part the 3Rs (i.e., Replacement, Reduction, and Refinement) guiding principles for a more ethical use of animal testing [1]. On the one hand, cultures replace animals; on the other hand, a single animal may provide many cultures and in turn give more information.

In addition to facilitate real-time imaging, an advantage of many MPS modelling tissue barriers is the integration of electrodes for continuous monitoring of transepithelial electrical parameters. Nevertheless, obtaining accurate transepithelial measurements with these systems is not easy. Two of the leading research groups working on organ-on-a-chip technology (i.e., Donald E. Ingber team at Wyss Institute and Albert Van der Berg's lab at Twente University) have been dealing with this issue and have recently published on the topic [2–4]. This thesis also presents pioneering work on measuring multiple barriers, as the goal of monitoring more than one tissue barrier in real time has been accomplished by integrating TEER measurement electrodes in multiple compartments of a microfluidic device.

MPS technology is a multidisciplinary field where the cooperation between biologists—to elucidate physiology and pathophysiology—and engineers—to address the technical challenges—has been crucial in developing functional models for translational research.

6.2 | SPECIFIC CONCLUSIONS

Two functional MPS for modelling and monitoring biological barriers have been presented in this PhD dissertation. To expand the sensing capabilities of the Ussing chamber to microfluidic culture systems, the one designed in chapter 3 and developed in chapter 4 has addressed the technical challenge of performing transepithelial electrical measurements in miniaturized chambers. The other one, described in chapter 5, has dealt with the interconnection of multiple tissue barriers and their continuous *in situ* monitoring, an innovative technology with great potential towards organ-on-a-chip applications.

Particular conclusions of the thesis are listed in the following:

1. Common electrode configurations reported in the literature for performing TEER measurements in Transwell and microfluidic culture systems have been studied numerically. It has been evidenced that TEER can be erroneously determined if the entire cell culture area does not contributes equally to the measurement as assumed in the widely used formula to calculate the TEER, especially when measuring low TEER values and when using microfluidic systems that have small chamber heights. This error may partially explain the large disparity of TEER values reported for same cell types. A correction factor that can be determined by FEM simulations has been proposed to correct this issue and also to be used in measurement systems with nonobvious current distributions.
2. A tetrapolar electrode configuration based on IDE has been proposed as an accurate measurement system to perform EIS in microfluidic cell cultures. Besides being accurate in the low range of TEER values, it implements minimal

electrode coverage so that the cells can be visualised alongside impedance analysis. Importantly, it has been described a numerical simulation method to adapt and optimise the electrode configuration to particular chamber dimensions.

3. A modular perfusion chamber with integrated EIS measurement electrodes has been developed combining microelectronic and rapid prototyping fabrication techniques. The device made of COP allocates a disposable membrane where the barrier tissue is formed. Therefore, the tissue can be assembled into the system to be exposed to a dynamic flow—not only to apply a FSS stimulus but also to continuously supply nutrients and to take away the waste—while being monitored through EIS. Additionally, the tissue can be removed from the system to facilitate analyses of the cells and the plates containing the electrodes can be autoclave-sterilized and reused.
4. The perfusion chamber has been used to build an *in vitro* model of the renal tubule including cells from the PT and TAL segments in the nephron. Both cell monolayers thrived for long term on the perfusion chamber where they were monitored by EIS in real time. Electrical conductance measurements of apical and basal solutions were achieved using the same electrodes that allowed transepithelial impedance measurements. Thus, the concentration of NaCl was estimated from the conductance enabling in-line measurement of the transepithelial chemical gradient of NaCl. Under imposed chemical gradients, the time course of the NaCl concentrations in apical and basal solutions were in good agreement with the simultaneous measurement of the TEER.
5. A novel cell compartmentalization strategy based on a grid of microgrooves has been presented as an alternative to membrane-based devices for interconnecting multiple tissue-tissue interfaces in organ-on-a-chip technology. By means of microelectronic techniques, it was fabricated a microfluidic device comprising a PDMS slab that defined the compartments and a glass chip that included the microgrooves and metal electrodes. Using this device, it was developed a microfluidic BRB model by co-culturing HREC, SH-SY5Y cells, and ARPE-19 cells, thus mimicking the inner and the outer BRB. Cells were cultured within the device for 3 days and the formation of endothelial and epithelial barriers were confirmed by permeability assays, TEER measurements, and TJ protein expression.
6. Real-time monitoring of inner and outer BRB was managed by means of TEER measurements using only a pair of straight electrodes buried on the substrate. The feasibility of this method was demonstrated with a calcium switch protocol where the time course of the measured resistance was equal to the TEER conventionally determined with electrodes in apical and basal sides. This approach avoids the laborious task of integrating electrodes in multiple compartments, which facilitates the future mass production.

6.3 | FUTURE WORK

The use of the here presented MPS will now be focused on the development of relevant *in vitro* disease models. In particular, the aim is to accelerate pathophysiology research in two severe human diseases: chronic kidney disease (CKD) and diabetic retinopathy (DR).

In collaboration with the Renal Physiology and Cardiovascular research group at Aragon Health Sciences Institute (IACS, Zaragoza), the perfusion chamber here developed may be used to elucidate which co-culture conditions (e.g., renal epithelial cells and fibroblasts) and mediators (e.g., cytokines) are determinants in the early stage and progression of fibrosis that can lead to CKD. This pathology is a gradual loss of kidney function that affects more than 10 % of general population. The progression of CKD appears to be associated to prevalent diseases such as hypertensions, diabetes, or obesity, and sometimes appears as a consequence of an acute kidney injury. When the patient reaches end-stage disease, renal replacement therapy becomes necessary. Mechanisms underlying the progressive loss of renal function are characterized by inflammation and tubulo-interstitial fibrosis development, which results in nephron loss and subsequent hyperfiltration (i.e., an increase in FSS); this process in turn contributes to further fibrosis. For this application and to expand the versatility of the chamber, an improvement would be the ability to measure the V_{te}. This would require the modification of the pick-up electrodes since platinum is not stable enough to allow long term recordings of the V_{te}. A more stable electrode material would be Ag/AgCl, however, the possible liberation of free Ag^+ ions into the solution may cause cytotoxicity. In this sense, the incorporation of a polymer coating acting as a salt bridge between the metal electrode and the solution would prevent the release of the Ag^+ ions. Another improvement would be the co-culture of different cell types on both sides of the membrane instead of fluidically connecting two double compartments (the perfusion chamber comprises three replicas of these double compartments). Although this has not being addressed in this dissertation, culturing cells on opposite sides of the membrane does not seem, a priori, to be an issue since the cells can be seeded before assembling the device.

In collaboration with the Diabetes and Metabolism research group at Vall d'Hebron Research Institute (VHIR, Barcelona), the microfluidic BRB model may be used to study the BRB neurovascular impairment and the underlying mechanisms of the diabetic retinopathy (DR) pathogenesis. This is a common complication of diabetes that remains a leading cause of vision loss in working age population. In general, there are two basic hypotheses to explain pathogenesis of DR; the loss of BRB integrity with an increase of vascular permeability, and the direct effect of diabetes on metabolism within the neural retina, which in turn causes breakdown of the BRB. DR has been considered a microcirculatory disease of the retina. However, there is emerging evidence to suggest that retinal neurodegeneration is an early event in the pathogenesis of DR that participates in the development of microvascular abnormalities. To achieve this goal, some technical and biological improvements should be done. For instance, the design of the PDMS stamp that currently defines seven compartments may be optimized for these particular requirements, that is, a PDMS stamp with three channels. Therefore, the neural tissue may cover the entire surface containing the multielectrode array, and each barrier tissue may be measured in two zones of the cell culture area. Another enhancement would be the parallelization of the microfluidic cell culture. In addition to miniaturization that reduces reagent consumption, parallelization enables implementation of high throughput screening assays. Moreover, a reversible bonding of the PDMS slab would allow to reuse the glass chip thus reducing the cost of the device. As a biological improvement, the neural tissue requires to display a more neuronal phenotype. The culture conditions of the neuroblastoma cell lines SH-SY5Y, which has been used here, will need to be revised in order to induce cell differentiation into mature neurons; a common agent for such purpose is retinoic acid. Altogether, the microfluidic BRB model would enable the study of the underlying mechanisms leading to neurodegeneration and the identification of the mediators in the cross-talk between neurodegeneration and microangiopathy that will be essential for the development of new therapeutic strategies for DR. In addition, if neurodegeneration and its neurovascular coupling are confirmed as the trigger of the BRB breakdown in the DR, new therapeutic targets could be identified to act in early stages of DR.

To date, electrophysiology of the paracellular pathway where TJ reside has been addressed by measuring large cell culture areas with countless cells. It is likely that new tools will emerge to record the ionic conductances of individual channels in tight junctions. This unprecedented spatial resolution measurement would give new insights into the underlying mechanisms of barrier regulation in molecular terms. Moreover, there are no straightforward solutions to determine the electrophysiological properties of 3D architectures (e.g., microvessels with circular cross-sectional geometries) contained within microchannels unlike isolated tubules that can be cannulated or micropunctured.

In vitro barrier models are suitable for studying the ability of pharmaceutical compounds to cross biological barriers, since these are the major impediment for agents to reach targeted tissues during drug delivery. In addition, barrier models are useful to quantify the transepithelial transport of drugs and thus provide information about times and doses at which organs are exposed to the drug for toxicity testing. Engineered MPS using human cells (e.g., primary cells or stem cells) have a high potential in many applications including drug screening, disease modelling, and regenerative medicine. In particular, the combination of these systems and stem cell technologies is a promising tool for the development of the so-called ‘precision medicine’, in which patient-derived cells are used for a personalized treatment.

Despite the progress made to develop representative MPS, many challenges remain to be addressed. For example, when dealing with heterotypic cell cultures, every tissue thrives in a specific cell culture medium that can differ from the others. Moreover, the heterogeneity of cells is detrimental for controlling the cell microenvironment of each cell type, which is a major advantage of MPS. On the other hand, microfabrication using soft lithography is appropriated to reproduce the cell organization of native tissues since it enables features in the sub-micron range; however, it requires the stacking of several patterned layers to build complex 3D structures, which results in a cumbersome fabrication process. Meanwhile, bioprinting technology is still in its infancy but is expected to grow rapidly if some issues related to print speed, bioink viscosity, and printer cost can be improved. Another challenge is to find biomaterials compatible with the microengineering techniques and also inert to the bind of drugs and compounds. In addition, using artificial materials as a cell support can partially restrict the diffusion of solutes or a direct contact communication between heterotypic cells. Finally, and independently of all the technical advances, it is desirable to develop user-friendly MPS that could be handled for non-skilled personnel and adapted to common equipment that is being used in cell culture laboratories.

6.4 | REFERENCES

[1] Russell WMS, Burch RL. *The principles of humane experimental technique*. London: Methuen, 1959.

[2] van der Helm MW, Odijk M, Frimat J-P, et al. Direct quantification of transendothelial electrical resistance in organs-on-chips. *Biosens Bioelectron* 2016; 85: 924–929.

[3] Henry OYF, Villenave R, Cronce MJ, et al. Organs-on-chips with integrated electrodes for trans-epithelial electrical resistance (TEER) measurements of human epithelial barrier function. *Lab Chip* 2017; 17: 2264–2271.

[4] Khire TS, Nehilla BJ, Getpreecharsawas J, et al. Finite element modeling to analyze TEER values across silicon nanomembranes. *Biomed Microdevices* 2018; 20: 10.

List of Publications

[1] Illa X, Vila S, **Yeste J**, Peralta C, Gracia-Sancho J, Villa R. A Novel Modular Bioreactor to In Vitro Study the Hepatic Sinusoid. *PLOS ONE* 2014; 9: e111864.

[2] **Yeste J**, Illa X, Guimerà A, Villa R. A novel strategy to monitor microfluidic in-vitro blood-brain barrier models using impedance spectroscopy. In: van den Driesche S (ed). Bellingham, WA: SPIE, p. 95180N.

[3] **Yeste J**, Illa X, Gutiérrez C, Solé M, Guimerà A, Villa R. Geometric correction factor for transepithelial electrical resistance measurements in transwell and microfluidic cell cultures. *J Phys Appl Phys* 2016; 49: 375401.

[4] **Yeste J**, Martínez-Gimeno L, Illa X, Guimerà A, Giménez I, Villa R. A modular bioreactor with integrated impedance spectroscopy electrodes for monitoring of epithelial and endothelial barriers. In: *20th International Conference on Miniaturized Systems for Chemistry and Life Sciences, MicroTAS 2016*. Chemical and Biological Microsystems Society, 2016, pp. 435–436.

[5] Acarregui A, Ciriza J, Saenz del Burgo L, Gurruchaga Iribar H, **Yeste J**, Illa X, Orive G, Hernández RM, Villa R, Pedraz JL. Characterization of an encapsulated insulin secreting human pancreatic beta cell line in a modular microfluidic device. *J Drug Target* 2018; 26: 36–44.

[6] **Yeste J**, Martínez-Gimeno L, Illa X, Laborda P, Guimerà A, Sánchez-Marín JP, Villa R, Giménez I. A perfusion chamber for monitoring transepithelial NaCl transport in an in vitro model of the renal tubule. *Biotechnol Bioeng* 2018; 115: 1604–1613.

[7] **Yeste J**, García-Ramírez M, Illa X, Guimerà A, Hernández C, Simó R, Villa R. A compartmentalized microfluidic chip with crisscross microgrooves and electrophysiological electrodes for modeling the blood–retinal barrier. *Lab Chip* 2018; 18: 95–105. Work featured on the front cover (Figure 6–1).

[8] Ortega-Ribera M, **Yeste J**, Villa R, Gracia-Sancho J. Chapter 18 - Biomaterials for the treatment of liver diseases. In: Mozafari M, Rajadas J, Kaplan D (eds) *Nanoengineered Biomaterials for Regenerative Medicine*. Elsevier, 2018, p. 464.

[9] **Yeste J**, Illa X, Álvarez M and Villa R. Engineering and monitoring epithelial and endothelial barrier models. *J Biol Eng.* **Submitted**.

Volume 18 | Number 1 | 7 January 2018 | Pages 1–208

Lab on a Chip

Devices and applications at the micro- and nanoscale

rsc.li/loc

ISSN 1473-0197

ROYAL SOCIETY OF CHEMISTRY

PAPER

Jose Yeste *et al.*

A compartmentalized microfluidic chip with crisscross microgrooves and electrophysiological electrodes for modeling the blood–retinal barrier

Figure 6–1 Artwork featured on the front cover of Lab on Chip journal.

List of Abbreviations

3Rs	Replacement, reduction, and refinement
Au	Gold
BBB	Blood-brain barrier
BRB	Blood-retinal barrier
BSA	bovine serum albumin
Caco-2	Colorectal adenocarcinoma cell line
Ccl	Cell layer capacitance
CNM	Centro Nacional de Microelectrónica
CNS	Central nervous system
CPE	Constant phase element
CSIC	Consejo Superior de Investigaciones Científicas
CVD	Chemical vapour deposition
DAPI	4′-6-diamidino-2-phenylindole
DMEM	Dulbecco's modified Eagle's medium
DPBS	Dulbecco’s phosphate-buffered saline
ECIS	Electric cell-substrate impedance sensing
ECM	Extracellular matrix
EDTA	Ethylenediaminetetraacetic acid
EIS	Electrical impedance spectroscopy
EMT	Epithelial-mesenchymal transition
FBS	Foetal bovine serum
FEM	Finite element method
FITC	Fluorescein isothiocyanate
FSS	Fluid shear stress
GAB	Grupo de aplicaciones biomédicas
GCF	Geometric correction factor
hUVECs	Human umbilical vein endothelial cells
hMSCs	Human mesenchymal stem cells

IDE	Interdigitated electrodes
IMB	Instituto de Microelectrónica de Barcelona
LSEC	Liver sinusoidal endothelial cell
MEA	Microelectrode array
MPS	Microphysiological systems
PC	Polycarbonate
PDMS	Polydimethylsiloxane
PET	Polyester
Pt	Platinum
PTFE	Polytetrafluoroethylene
PSA	Pressure-sensitive adhesive
PVD	Physical vapour deposition
R_i	Intercellular resistance
RIE	Reactive-ion etching
RITC	Rhodamine B isothiocyanate
TEER	Transepithelial electrical resistance
TJ	Tight junctions
TNF-α	Tumour necrosis factor alpha
VEGF	Vascular endothelial growth factor
V_{te}	Transepithelial voltage